Title of Grant / Cooperative Agreement:	APPLE: Atomic Planar Power for Lightweight Exploration
Type of Report:	Summary of Research
Name of Principal Investigator:	E. Joseph Nemanick
Period Covered by Report:	April 1, 2022 to March 31, 2024
Name and Address of recipient's institution:	The Aerospace Corporation, 2310 E. El Segundo Blvd., El Segundo, CA 90245
NASA Grant / Cooperative Agreement Number:	80NSSC22K0768

Reference 2 CFR § 1800.908 or 14 CFR § 1260.28 Patent Rights *as applicable (abbreviated below)*
The recipient may use whatever format is convenient to disclose subject invention required in subparagraph (c)(1). NASA prefers that the recipient use either the electronic or paper version of NASA Form 1679, Disclosure of Invention and New Technology (Including Software), to disclose subject inventions. Both the electronic and paper version of the NASA Form 1679 may be accessed at the electronic New Technology Reporting Web site https://invention.nasa.gov.
A final new technology summary report listing all subject inventions (or a statement certifying there were none) for the entire award period; which report shall be submitted within 90 days after the end date for the period of performance within the designated system noted within the award document."

Have any Subject Inventions / New Technology Items resulted from work performed under this Grant / Cooperative Agreement?	No ◉	Yes ○
If yes a complete listing should be provided here: Details can be provided in the body of the Summary of Research report.		

Reference 2 CFR § 1800.907 or 14 CFR § 1260.27 Equipment and Other Property *as applicable* (abbreviated below)
A Final Inventory Report of Federally Owned Property, including equipment where title was taken by the Government, will be submitted by the Recipient no later than 60 days after the expiration date of the grant. Negative responses for Final Inventory Reports are required.

Is there any Federally Owned Property, either Government Furnished or Grantee Acquired, in the custody of the Recipient?	No ◉	Yes ○
If yes please attach a complete listing including information as set forth at § 1260.134(f)(1).		

Attach the Summary of Research text behind this cover sheet.

Reference 2 CFR § 1800.902 or 14 CFR § 1260.22 Technical publications and reports *as applicable* (abbreviated below)
Reports shall be in the English language, informal in nature, and ordinarily not exceed three pages (not counting bibliographies, abstracts, and lists of other media).

A Summary of Research (or Educational Activity Report in the case of Education Grants) is due within 90 days after the expiration date of the grant, regardless of whether or not support is continued under another grant. This report shall be a comprehensive summary of significant accomplishments during the duration of the grant.

APPLE, ATOMIC PLANAR POWER FOR LIGHTWEIGHT EXPLORATION

NIAC PHASE II FINAL REPORT

June 30, 2024

E. Joseph Nemanick, The Aerospace Corporation, Energy Technology Department
Sabah Bux, Jet Propulsion Laboratory, Power and Sensors Department
Henry Helvajian, The Aerospace Corporation, Surface Science & Engineering Department
Gabriel Veith, Oak Ridge National Laboratories, Chemical Sciences Division
Adon Delgado, The Aerospace Corporation, Thermal Control Department
David Hinkley, The Aerospace Corporation, Missions System Engineering Department
Billy Chun-yip Le, Jet Propulsion Laboratory, Power and Sensors Department
Martin Schmeidler, The Aerospace Corporation, Thermal Control Department
Donald Chaney, The Aerospace Corporation, Vehicle Systems Division

Prepared for:

NASA Innovative Advanced Concepts
NASA Space Technology Mission Directorate
300 E. St. SW
Washington, DC 20546

Solicitation No. 80HQTR22NOA01-22NIAC_A2

Award No. 80NSSC22K0768

Executive Summary

The ***Atomic Planar Power for Lightweight Exploration*** **(APPLE)** is a small scale, modular, isotope agnostic spacecraft power architecture that merges the extensive heritage of radioisotope power generation with a radiation-hard battery in a robust modular system which can enable a wide range of spacecraft and rover design. The Phase II APPLE design consists of a small core of radioisotope of either ^{238}Pu or ^{241}Am oxide mounted on skutterudite thermoelectric legs, insulated in an aerogel insulation, mounted on the vehicle chassis for thermal dissipation. The primary Phase II findings are:

- The APPLE architecture is not only feasible but also opens the design space for spacecraft and mission designs through distributed power that scales across vehicle sizes, from 10's of Watts to kilowatt systems, integral placement in the vehicle and chassis thermal dissipation without a dedicated radiator.
- Thermal simulations showed that locating the battery at the thermoelectric cold shoe/radiator junction maintains a temperature range between 0˚C and 30˚C for the battery while the hot shoe thermoelectric junction remains at 500˚C. Vehicle chassis can sufficiently dissipate waste heat and keep vehicle warm.
- Skutterudite (SKD) thermoelectrics can operate at greater than 10% efficiency and meet the 17+ year wearout mission requirements.
- Mission designs for a distributed Lunar seismic mission can use multiple APPLE cores to survive the lunar night.

In Phase II, APPLE underwent several design changes as a result of the simulations of the thermal design interface, the thermal profile, and radiation exposure. It was demonstrated that limiting the isotope hot shoe temperature to a skutterudite compatible temperature (500˚C) enabled a room temperature cold shoe temperature. This enables mounting APPLE on the vehicle chassis, removing a dedicated radiator and its associated mass. This enables complete utilization of the thermal inventory for power as well as vehicle heating without extensive thermal distribution systems. Utilization of the chassis as the radiator allows for large radiative surface without adding radiator mass while increasing the efficacy of heat-to-electricity conversion (10-11%). APPLE is intended to utilize waste heat from the isotope to reduce the need for component heaters and power. With the integral location of the APPLE device within a deployable payload, vehicle, or system, APPLE can both efficiently convert heat to electricity and warm the vehicle. In Phase II, we fabricated four leg, 2 junction SKD thermoelectric units and mated them with an isotope simulator for power generation. We demonstrated voltage and current generation for APPLE.

The Phase II studies of thermoelectric conversion and radiation generation included both $^{238}PuO_2$ as well as $^{241}Am_2O_3$ to take advantage of the ramped up production of ^{241}Am, derisking the technology from ^{238}Pu supply. Radiation simulations of alpha and gamma penetration from ^{241}Am indicated that minimal amounts of refractory metal cladding was needed to prevent significant dose of radiation during integration. In addition, this radiation cladding protects the isotope in a launch failure through ductile deformation to contain the material.

Mission designs utilizing APPLE as the power source demonstrate that small landers can survive the lunar night, as well as power small (<1 kg) vehicles for independent navigation around an asteroid or in orbit.

Contents

The Atomic Planar Power for Lightweight Exploration, (APPLE), is an enabling architecture for solar system exploration with low mass vehicles. Its goal is to develop an advanced vehicle power architecture that integrates lightweight radioisotope power in a modular, scalable power system.

1. Concept Overview

APPLE is a radioisotope-based modular power and energy storage spacecraft architecture that enables long duration missions destined for the outer reaches of the solar system or and around worlds. In these regions solar photon flux is low, or blocked by planetary rotation, requiring radioisotope power sources. APPLE can enable fast-transit spacecraft missions by providing a substantially lower mass power system architecture than existing monolithic, massive RTGs, while still providing long mission life (30+ years). It can also power small planetary rovers or payloads where the existing large RTGs are too large, and solar energy is too low or blocked by planetary rotation. The architecture will drive rapid exploration of the deepest parts of the Solar System via a low mass power system architecture. This will enable scientific exploration on smaller (e.g. nanosatellite class) spacecraft, unlocks the use of solar sail propulsion for increased vehicle velocity to send nanosatellite class vehicles distant locations, and opens up RTG power for small rovers, and accelerates vehicle and mission design through a modular power system.

The ***Atomic Planar Power for Lightweight Exploration*** **(APPLE)** is a low mass, high reliability spacecraft power architecture that converts the extensive heritage of radioisotope power generation into a small (50-200g) modular power system which can enable a wide range of vehicle and mission designs. A modular power architecture will open up the design space for spacecraft bus by enabling power designs to fit the mission for any vehicle shape or size, from 10's of Watts to kilowatts. As shown in

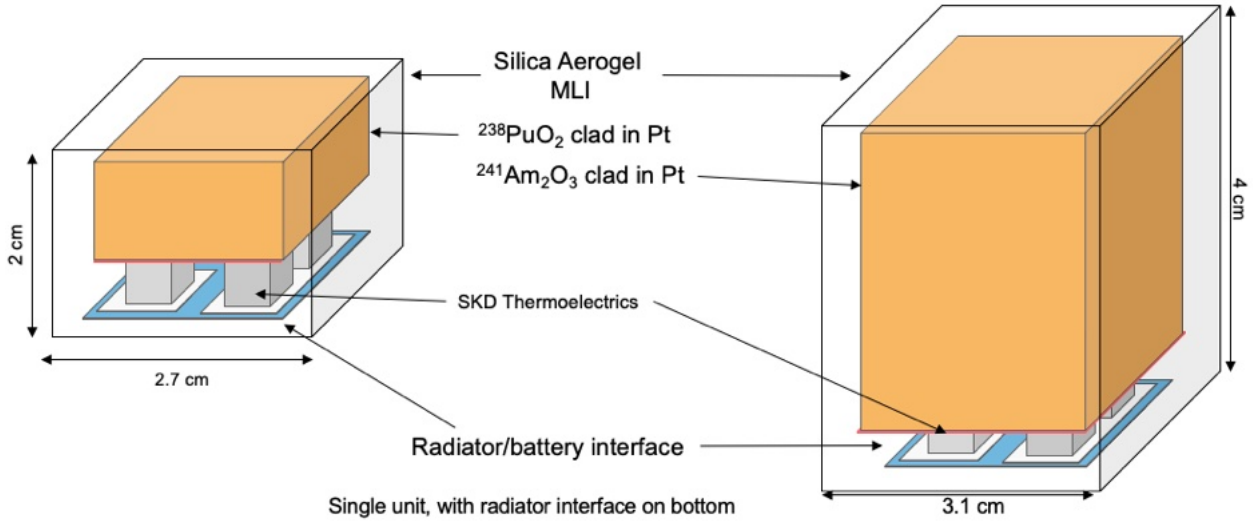

Figure 1. Two APPLE designs from the Phase II work. On the left is the PuO_2 design, using 31g of PuO_2 and on the right is the Am2O3 design, using 154g of Am_2O_3. Each unit produces 16.7W_{th} of thermal energy and is converted to 1.7 W_e of electric energy through the skutterudite thermoelectric legs. The thermal energy is dissipated through the radiator interface at the bottom of the unit to the vehicle chassis.

Figure 1 APPLE uses small $^{238}PuO_2$ or $^{241}Am_2O_3$ cores with skutterudite (SKD) thermoelectrics to generate power. The two designs deliver the 17 W of thermal energy from the radioisotopes into the thermoelectric junctions and then into the radiative interface, which is mounted to the vehicle chassis, enabling use of the full thermal load to heat the vehicle while generating power. The SKD thermoelectrics deliver 1.7 W of electrical power for a small mass (39g for Pu and 187g for Am).

This Phase II work demonstrated the efficient (>10%) conversion of isotope heat to electricity and on vehicle thermal radiation, as well as the safety of using small isotope cores with minimal cladding to protect workers from radiation exposure during integration and testing, as well as in the event of suborbital launch failures. Missions to the moon for deployable seismic landers as well as free flying asteroid explorers demonstrate the benefit and need for smaller, more capable RTG systems for the future of space exploration.

1.1 Motivation

We are at a technological precipice of being able to widely visit and study our Solar System and beyond by robotic rovers (e.g. moons, Mars), aerial drones (e.g. Mars Ingenuity), orbiting/flyby probes (e.g. Enceladus Life Finder, JPL Marco) and missions into deep space (e.g. Solar Gravity Lens). The NIAC program under STMD is one of the propelling forces for applying technological ingenuity in support of these sought-after missions. All of these missions require power, and many destinations cannot efficiently use photovoltaic technology.[1] A non-photovoltaic power and energy architecture that is modular, scalable, compact, low mass, long lived and robust to the space environment would enable a host of new missions and vehicle designs. In addition, more efficient, non-plutonium RTG designs are needed to mitigate impacts from the low rate of transmutation for Pu generation. NASA and DOE have committed 24 RHUs for the Dragonfly mission to Titan, and 40 RHUs to ESA's Rosalind Franklin rover. This leaves only two MMRTGS and 20 additional RHS for New Frontiers missions to launch in the 2030s. Additional missions such as the Uranus Orbiter and Probe, a highly prioritized mission in the Planetary Decadal Survey are not able to be met under current Pu-238 production planning.[2] Currently there are no Pu-238 GPHS units dedicated for other missions such as lunar exploration, arguably the most critical destination for radioisotope power, with the long nights and low temperatures.

With the fixed decision to only produce enough Pu-238 for future MMRTG missions, expansion of RTG operations beyond the handful of planned MMRTG missions requires a new hardware built to accommodate other isotopes, particularly the new supply of Am-241 being produced in Europe. The reduced amount of isotopes needed by increasing the efficiency and the overall smaller form factor of APPLE, multiple smaller missions can be planned, in small form factors on non-flagship missions to prove out this new power architecture. In addition, the low supply of Am-241 planned also means that very few, if any, Am-241 clads will be made available for NASA missions, and would require a power architecture than can operate on single clads, which only APPLE can do.

NASA is investing in several nanosatellite technologies which could be the basis for a modularized, self-assembled in-space architectures and small ground based rovers. NASA is also investing in solar sail propulsion technology (e.g. Solar Cruiser) to explore the possibility of very fast transits through our solar system and beyond (0201 NIAC Phase II). Finally, they are also exploring the next generation in space telescopes (e.g. LUVOIR). Among these and many other missions, an APPLE power system could enable nanosatellites to produce more data (e.g. MarCO), stay on mission longer, to permit high velocity transit space probes that would provide a wider area of space exploration, and better facilitate the flagship missions and to enable very large in space structures to operate in a distributed power mode and thereby reducing harness mass.

Current chemical propulsion technologies reach 3-5 AU/yr velocities for spacecraft. For spacecraft with higher transit velocities (>15 AU/yr) which can be achieved via solar sails[3] propulsion and a close solar perihelion transit, it is essential that the total vehicle mass be low while retaining high power capability and reliability of the avionics and payloads. For a practical solar sail area, this forces the total spacecraft mass to be within 10-20 kg for transit velocities of 10-20 AU/yr. Even for nanosatellites (<10 kg) with electric propulsion,[4] a power system mass less than 1-2 kg would be a mission enabler. Whatever the propulsion source, existing qualified RTG systems are massive, constant power systems, and designed only for large vehicles. In addition, conventional battery technology requires shielding from radiation and particulates from the space environment limiting their placement to deep interior of vehicles. Many current and next generation deep space mission designs like Solar Gravity Lens, SIMPLEx, and MarCO use low mass vehicles that cannot accommodate large RTGs or spare excess mass for power system shielding. Without onboard, small size, robust power sources their power would have to be supplied through energy beaming or short lived primary batteries further limiting capability and increasing vehicle mass. Consequently, the APPLE power system architecture fills a key technology gap. A modular and scalable RTG technology would allow for design flexibility and enable deep space small vehicle missions. This technology gap is addressed by the modular nature of the APPLE architecture providing power and heating.

Current power systems for small planetary rovers are limited to either photovoltaic systems or primary batteries. While MSL and Curiosity are RTG powered, these are large (900 kg) vehicles. Smaller vehicles like those needed for more distant destinations (Enceladus, Europa, Titan), or for novel propulsion systems (helicopters, swimmers, climbers) need a small, capable power system. The existing RTG systems are simply too massive for deployment on small (10-20 kg) vehicles. To open up planetary rover exploration, a lightweight power system is needed that does not depend on sunlight. A small power system that utilizes its own heat can reduce rover mass while extending exploration and science.

1.2 RTG Requirements

Radioisotope thermoelectric generator (RTG) technology has been NASA's reliable long-life, non-photovoltaic power system, but these systems have been massive (10's of

kg), monolithic, and cannot be accommodated on the small, lightweight space platforms needed for next generation missions to distant destinations. The masses and BOL powers for commonly used RTGs: a) SNAP-9A (12.3 kg, 26.8 W_e), b) SNAP-19A (13.6 kg, 40.3 W_e), c) eMMRTG (40.3 kg, 125 W_e), and GPHS-RTG (57 kg, 300W_e).[5] In addition, RTGs provide continuous, but declining, power and must either be scaled to accommodate the peak power requirements of a mission (e.g. long distance COMM, imaging, radiometry, etc.) or have onboard energy storage capabilities.
RTG design efficiency is dependent not only on the ZT of the thermoelectric materials, but also the ΔT between the hot and cold shoes. This equilibrium temperature is primarily dependent on the amount of heat generated and the radiator size and efficiency. Existing RTG designs have had to compromise on radiator size, as the relatively compact form factor (cylindrical) meant that the radiator fins had impaired view of space, and extending them would result in additional mass penalties. Using the flat APPLE on vehicle mounting there are no radiator surfaces to carry, or block instrument's views of space, and the amount of chassis surface allows for more radiative surface area than was accommodated on previous MMRTG powered designs. This increased radiative surface improves thermoelectric efficiency, lowers vehicle mass, and directly delivers thermal energy to the spacecraft. This thermal energy at the vehicle chassis can result in room temperature vehicles, removing the need to power resistive heaters (less power needed), reduces or eliminates thermal range for components (less design/complexity of components), and brings power generation into the vehicle (more compact). This can result in a greater ΔT for a given isotope mass, and a higher conversion efficiency and lower isotope mass, a critical need given the restricted isotope supply and the safety issues associated with isotope carrying launches. By increasing efficiency as well as reducing the minimum size of individual units current isotope inventory can be stretched farther, and new isotopes (^{241}Am) can be used, revitalizing RTG powered space exploration.

1.3 Current Battery Capability

The state of the art high energy density battery technology for spacecraft are lithium ion cells (Li-ion). With energy densities up to 300 Wh/kg,[6] these cells store the most energy for the lowest mass and volume, displacing older rechargeable chemistries such as NiCd and nickel hydrogen (NiH_2) cells used in older NASA missions.[7] The challenges of using lithium ion battery technology for spacecraft energy storage in large spacecraft revolves around the thermal control and maintenance of the battery as well the battery wear and ageing. Li-ion cells were designed for terrestrial applications, and as such have an optimal temperature operating range of 20 ± 10˚C. Battery performance outside these ranges degrades the battery performance and life, and can lead to catastrophic failures.[8] Because of this, the batteries in deep space missions must be kept within this range over mission life through the use of electric heaters which drawn upon the vehicle bus. For large vehicle power systems, the battery is typically placed inside the vehicle, close to the center of mass, as the battery is often one of the heaviest components of the vehicle. This placement interior to the spacecraft does benefit thermal regulation, keeping it with other components such as payloads that need thermal regulation. This interior position also benefits the battery by isolating it from external hazards, namely ionizing radiation and (small) impacts.

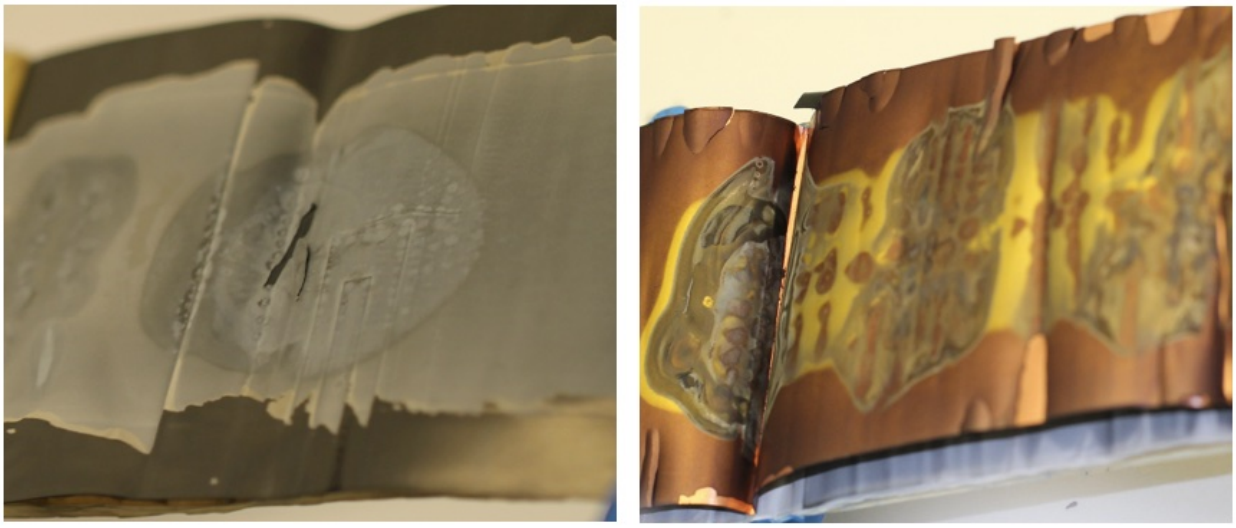

Figure 2. Li-ion battery electrode materials after 18Mrad gamma radiation exposure and 600 operational cycles. A) shows the embrittled polymer separator adhered to the cathode, and B) shows the discoloration of the anode material, with gold regions that could not discharge.

For a design that is compatible with small spacecraft, in the 1-20 kg range, there is less 'deep interior' in the vehicle. In addition, for small, or modular spacecraft, the Li-ion battery can no longer be bulky rolls of material in heavy metal cases. In a small, thin, lightweight modular design, the battery must be much thinner, without the benefit of thick steel cell cases and battery boxes. This means the battery is no longer shielded from the radiation and particulate environment of space. Studies conducted at the Jet Propulsion Laboratory and at the Aerospace Corporation showed the effects of radiation on conventional Li-ion batteries. Panasonic B 18650 cells were exposed to 18 Mrad of ^{60}Co gamma radiation to simulate the effects of radiation sterilization of the battery for planetary protection needs and Jupiter radiation belt ionizing radiation effects. These conventional Li-ion cells showed only minimal initial effects to battery capacity from this irradiation. However, upon cycling the cells showed significant reduction in cycle life, and inspection of the batteries at Aerospace post cycling failure showed extensive damage to the battery materials, as shown in Figure 2. The cells on cycling showed catastrophic failures around 600 cycles, with various hard and soft short circuits causing cell failures. The degradation of the cell materials upon inspection correlated with these failures, as the polymer separator was found to be embrittled and prone to failure, and the anode showing signs of lithium plating. Both of these failure modes are consistent with degradation of the organic components of the battery, with the polymer separator becoming fragile, and the organic electrolyte polymerizing, resulting in a higher cell impedance linked to dangerous lithium plating. In this test, the cells had a 1mm thick steel case, as well as, for most of the electrode materials, layers of additional shielding battery material due to the jelly roll structure. For planar cell designs to fit in the modular APPLE design, there will be no effective shielding of the battery from external radiation sources, and the battery materials must be robust to ionizing radiation over long mission life.

To remove organic components in an APPLE battery, the existing electrolyte and polymer separators must be replaced with more robust materials. The electric vehicle

and personal electronics industries are developing solid-state ceramic combination separator/electrolyte systems that should be more resistant to ionizing radiation. There are several systems being developed, including the oxynitiride ($Li_xPO_yN_z$, LiPON) system, garnets ($Li_7La_3Zr_2O_{12}$, LLZO), phosphates ($Li_{1+x}Al_xTi_{2-x}(PO_4)_3$, LATP and $Li_{1+x}Al_xGe_{2-x}(PO_4)_3$ LAGP), perovskites, ($Li_{3x}La_{2/3-x}TiO_3$, LLTO), germania ($Li_{14}Zn(GeO_4)_4$), nitride (Li_3N), and sulfide (γ-Li_3PS_4) systems. The radiation hardness of each of these materials has not been determined, but it is likely that the structural and ionic conductivity parameters are more robust to ionizing radiation than organics and polymers due to higher bond strengths and extended crystal structures of these materials. *A radiation hard battery based on the LiPON system is part of the ongoing collaboration between the Aerospace Corporation's Intelligent Battery Group and Oak Ridge National Labs and can be used as the energy storage for APPLE.*

However, these solid-state materials typically have a significant drawback in application in comparison to organic electrolytes, as ceramic ionic conductivities are significantly worse. This limits the maximum discharge and charge rates for the batteries, a key limitation for mission application where peak power will be needed for applications like comm, and payloads, and rover motors. The room temperature conductivities for the solid-state electrolytes are ~ 1 x 10^{-6} S cm^{-1} for LiPON,[9] 1× 10^{-4} S cm^{-1} for LAGP,[10] 1.0 × 10^{-5} S cm^{-1} for garnets,[11] 1 x 10^{-5} S cm^{-1} for perovskites,[12] 1 x 10^{-5} S cm^{-1} for germania,[13] and 1 x 10^{-3} S cm^{-1} for sulfides.[14] The conductivity for typical commercial Li-ion organic electrolyte systems is ~1 x 10^{-2} S cm^{-1}.[15] These solid-state ceramic systems, however, show much better conductivities above ~60˚C,[16,17] meeting or exceeding typical organic systems, at a temperature which rapidly degrade organic electrolytes. Since spacecraft operations rarely use very high power operations (kW or greater) such as used in electric vehicles, they instead need batteries to operate for long durations, and so carry extra capacity to address battery fade over life rather than supply high power bursts. Operating the battery in this design at low rates (C/5 or less) will avoid the key issue to using solid-state batteries for terrestrial applications which typically cannot operate at these temperatures.

In addition, these solid-state battery systems are more puncture resistant than the organic systems with polymer separators, as solid materials typically prevent the microshorts that occur during puncture in conventional systems.[18] This puncture resistance is critical for a battery that can face repeated small particle impacts during a mission on a small vehicle that would not be a significant risk in large vehicles. Whereas conventional liquid electrolyte cells could go into thermal runaway upon puncture, a solid-state design would not, and perhaps even still be able to function, but even if not, would not damage more of the battery in its distributed, modular shape.

1.4. Technology Needs

In summary, the key needs for a new RTG system that APPLE seeks to meet are a lightweight, modular system to enable a range of vehicle sizes, from microsats and small rovers up to large flagship missions. In addition, to accommodate a wide range of vehicle morphologies and to enhance the RTG efficiency, APPLE has a small and modular design. This size allows for no radiators but rather chassis mounting for

efficient radiation and a higher heat-to-electricity conversion. As seen in the mission technology and design section below, APPLE will enable a new class of deep space missions built around a robust, flexible, multifunction power architecture.

Electrical power for missions to Jupiter and beyond require RTGs, making them an enabling technology for a wide range of destinations and missions outlined in the Decadal Survey. European RTG technology development is targeting electrical power output of 50 W per unit, with the RTG program at TRL 4.[19] The European RPS is being designed around Americium-241;[20,21] with its longer half-life (433 years) when compared to Plutonium-238 (88 years), but lower thermal power output of 0.12 W_e per gram of ^{241}Am metal, versus 0.57 W_e per gram of ^{238}Pu metal. The unit life requirement for this European design is 20 years, meaning isotope thermal output decay will be a negligible factor. Even with existing ^{238}Pu designs the RTGs have continued to function well past the planned end of mission, such as Pioneer 10 operating well past its planned two year mission by several decades,[22] and Voyagers 1 and 2 are still operational after 47 years. Current NASA RTG development projects have a design requirement of 17 years. These long durations are required for the extended transit times of deep space missions where RTG power is the only solution.

However, a growing need is being recognized for missions that can effectively use RTG power on much shorter missions. The Curiosity (2011) and Perseverance (2020) rovers have recently demonstrated the capability RTG power brings to missions much closer to home, delivering power electrical power and heat to the rovers for their missions. These missions are typically planned for far shorter missions, due to both the shorter transit times (7-8 months) as well as the effects of the rugged conditions on Mars leading to wear out of key systems such as transportation and payloads. The short day-night cycle on Mars (24.6 Earth days) means that the thermal survivability of the Martian nights is important, but have been successfully managed with solar power plus battery storage. The other nearby RTG destination has a far more punishing day/night cycle: the moon's 28 Earth days. Nighttime survivability for Lunar missions without radioisotopes has been so far an unsolved problem, with examples of the solar plus batteries Chandrayaan-3 mission failing to wake up after its first night. China's Yutu-2 rover has so far survived since December 2018 using radioisotope heater units (RHUs) to keep warm overnight, shattering the RHU heated Lunokhod-1's record of eleven lunar days. The longest lasting lunar mission was the Apollo era seismic sensors, which were RTG powered. Apollo Lunar Surface Experiment Packages (ALSEPs) deployed on Apollos 11, 12, 14, 15, and 16. The missions were designed to determine the structure of the moon's interior, the number of meteorite impacts, and tidal stresses in the lunar surface. The ASLEP experiment was powered by a Radioisotope Thermoelectric Generator (RTG).[23] The mission lasted from November 1969 to September 1977, with the units lasting up to 8 years until turned off by Mission Control. The units were powered by SNAP-27 Pu-238 RTGs[24]

While solar powered missions that have RHUs for overnight heating are a demonstrated technology, these missions have operated during the lunar day with full power and hunkered down during the lunar night trying to survive the low temperatures. This limits the total amount of science that can be done by half for science that can be done while

the sun shines, but more importantly limits operations to locations with regular and sustained solar power. Many rover mission locations do not have regular solar insolation, including permanently shadowed craters on Mars and the moon, subsurface caves, and polar regions with a low solar incidence and extended night periods. To both extend the amount of science a mission can deliver, as well as enabling missions to these poor solar regions, the survival heaters of RHU's must be extended to include electrical power generation from RTGs.

1.5 Design Changes Over Phase I Design

In Phase I, a flat, multi-core design was developed, mounted with a large, flat radiator surface, and TAGS/PbSnTe thermoelectrics as seen in Figure 3. This design was meant to be integral, with no addition components needed, such as additional radiators, and could be mounted on the vehicle (without thermal contact) with the radiator surface facing out. The isotope cores were $^{238}PuO_2$ in a Pt clad. This design would deliver 1 W_e power from 15 W_{th} of thermal energy, and store up to 5 Wh of energy in an integral battery mounted at the integral radiator. This design was 8.6% efficient for electrical energy, but required additional components such as heat pipes to deliver heat to other components to the vehicle as the radiator and insulation was designed to only radiate heat to the space environment. The insulation was a silica aerogel. In addition, this design had four cores per radiative segment, with independent power cores that each had two p-n junctions, and the four junctions had the capability to be connected either in series or parallel.

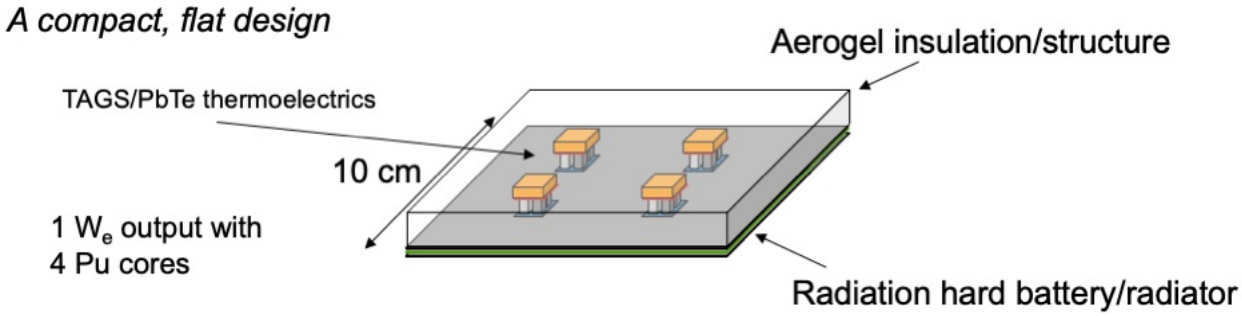

Figure 3. Phase I design was flat, complete design, with thermoelectric components and an integral radiator, the structure of which would also be flat form factor battery.

In Phase II, the design simplified the concept by eliminating the integral radiator, and reduced the minimum device size to a single isotope and thermoelectric core, though expanded the isotope clad. This new concept was built and tested in Phase II with two p-n thermoelectric junctions per isotope unit, with the design capable of incorporating up to eight p-n junctions per isotope core for series/parallel connection. Depending on the number of APPLE units per vehicle, the series parallel connections could be altered to meet the desired bus voltage for the application. In addition, the Phase II design was expanded to incorporate ^{241}Am as an isotope material, in the Am_2O_3 form. The smaller size of the total device per individual unit still had a higher thermal and electrical output, of 16 W_{th} and 1.7 W_e due to an increased electrical conversion of efficiency of 10.9% for the Pu and 10.0% for the Am model. The increase in efficiency stems from the use of a skutterudite thermoelectric materials with a p-SKD: $Ce_{0.9}Fe_{3.5}Co_{0.5}Sb_{12}$ and n-SKD:

$Yb_{0.15}Ba_{0.05}Co_4Sb_{12}$ as well as a larger effective radiator surface. Despite not having an integral radiator, the Phase II design dissipates the isotope heat more efficiently through connection to the vehicle chassis, allowing for direct utilization of the isotope heat post electrical conversion.

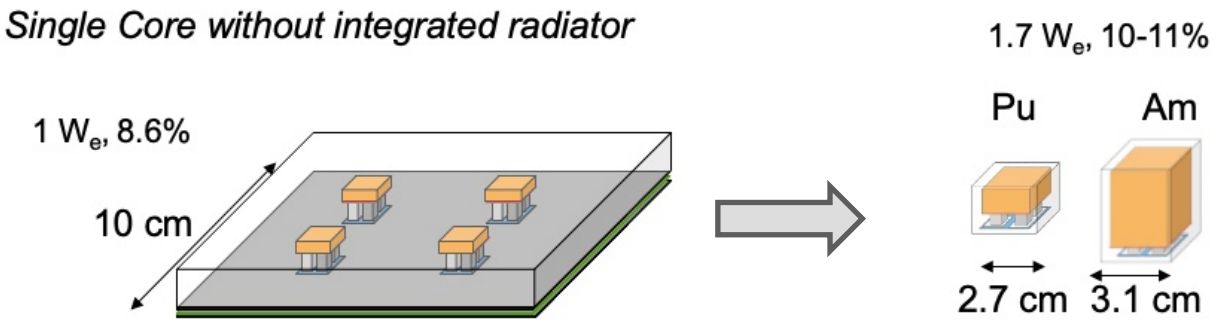

Figure 4. The new design eschews the large integrated radiator. Vehicle design efforts showed that thermal effects would need to be considered, and that the vehicle surface provided substantial 'free' surface area for heat radiation.

2. Radiation Simulations

Radiation simulations are necessary in APPLE design for several reasons, including determination of required isotope cladding thickness to shield workers and sensitive electronics from isotope radiation, to evaluate the radiation exposure of the thermoelectric materials, both from the isotope as well as the space environment, and, as performed in Phase I, the deposited dose in the battery materials. The APPLE design uses a compact unit for spacecraft design flexibility leveraging the chassis for thermal regulation, however, this design does not keep the radioisotope segregated from the spacecraft components as in heritage RTG designs, but rather keeps the radioisotopes close in to the chassis to leverage thermal dissipation and waste heat utilization to keep components warm. For the isotope selection, this prioritized alpha particle emitters over that of more penetrating beta or gamma emitters. For the radiation simulations, the geometry of the device and local shielding was taken into account for simulations. There are several sources of ionizing radiation to and from the APPLE RPS unit, with several components of concern. The thermoelectric materials may also absorb radiation which may impact performance and life, as well as the battery component of the device.

Results indicate that dose due to the space environment drives battery exposure over radiation from the isotope source. The selected radioisotopes, ^{238}Pu and ^{241}Am are primarily alpha emitters, which does not penetrate outside of the isotope material and its refractory metal clad. External dose in interplanetary space due to solar particle events (SPEs) is dynamic and can be unpredictable, depending on the mission location, duration, and space weather. For this reason, we simulated worst-case scenarios to maximize the probability of designing for mission success when using APPLE. These scenarios covered high flux solar events in the inner solar system (Earth and inwards) portion of the mission, where solar flares in transit can result in high doses of ionizing radiation. Dose in interplanetary space (Mars and outward) due to galactic cosmic rays (GCRs) was found to be concerning due to the high energy of these particles and their associated penetration depth. GCRs can also initiate a shower of secondary particles upon incidence with a material, causing downstream effects. Strategic decisions on launch dates (during solar minimum activity) and mission duration (shortest possible) are thus at least partially driven by space radiation dose concerns.

2.1 Radioisotope Selection

The radioisotope sources considered for this design were Plutonium (^{238}Pu), Americium (^{241}Am), and Strontium (^{90}Sr). ^{238}Pu has a long history of space use with NASA.[25] Despite serious concerns with supply,[26] the existing use of this isotope should be streamlined compared to a new isotope source selection. ^{238}Pu has historically been the isotope of choice for RTGs used by NASA missions, used in their previous RTG designs such as Voyagers 1 and 2, Vikings 1 and 2, Cassini, New Horizons, and the MSL. The isotope has an 87.7 year half-life, and generates 0.57 W/g for pure ^{238}Pu and

0.502 W/g in its PuO_2 form, the stable oxide of choice for use. Additional isotopes with high thermal output and sufficiently long half-life for deep space missions considered in this project were ^{90}Sr and ^{241}Am. ^{90}Sr is typically used in its titanate form for chemical stability, while ^{241}Am is generated as the Am(II) oxide, but this oxide decomposes to form the Am(III) form in Am_2O_3. ^{90}Sr is an attractive isotope due to its relative abundance from domestic nuclear reactor waste,[27] and ^{241}Am is the isotope being purified for ESA's RTG designs.[28]

Table 1. Figures of merit for the three RTG isotopes under consideration.

Isotope	Material	Thermal output (metal, W/g)	Thermal output (material, BOL, W/g)	Thermal output (material, EOL-15y, W/g)	Mass (material, g/cm^3)	Thermal output (material, W/cm^3)
^{238}Pu	PuO_2	0.57	0.50	0.45	11.5	5.77
^{90}Sr	$SrTiO_3$	0.95	0.46	0.32	5.11	1.31
^{241}Am	Am_2O_3	0.11	0.10	0.10	11.77	1.21

However, these isotopes decay through widely different mechanisms, and release their energy via different particle emissions. These particles must be captured through interaction with the RTG mass to generate heat. The decay products of each of these three sources vary in both species and energy, with ^{238}Pu emitting 5.593 MeV alpha particles, ^{241}Am emitting 5.478 MeV alpha particles and 59 keV gamma rays, and ^{90}Sr emitting 0.546 MeV beta particles (electrons). Figure 5 shows the average penetration depths of the isotope decay particles in common RTG and spacecraft materials.[29,30,31] These values were calculated using National Institute of Standards and Technology (NIST) lookup tables of stopping power, range, and/or mass attenuation coefficients for specific decay products and target materials. The ^{238}Pu alpha particles have very large interaction cross sections, meaning that they have very short penetration depths for energy capture. Typically, the majority of this energy is captured within the ^{238}Pu oxide material itself, with the small remaining portion captured in the isotope cladding. ^{90}Sr,

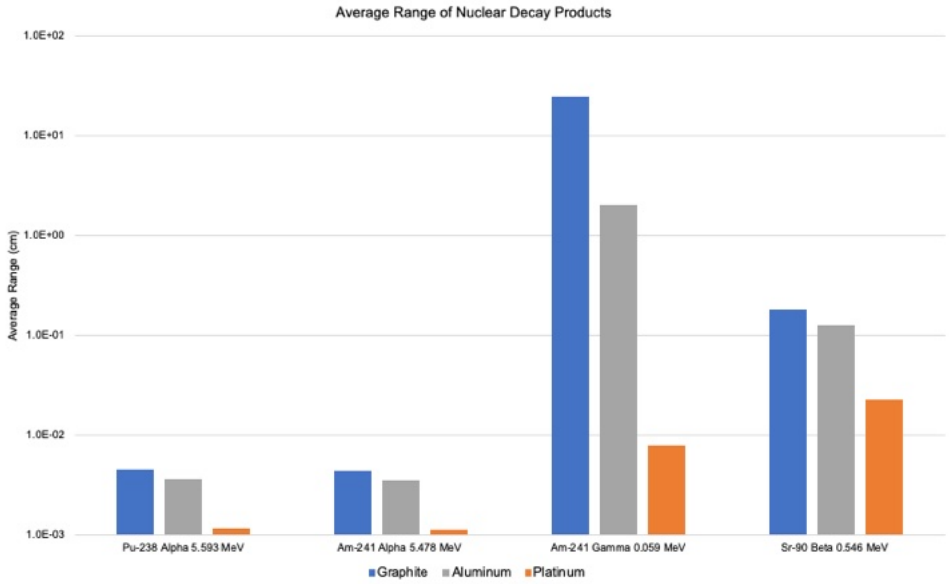

Figure 5. Average penetration depths of decay particles from ^{238}Pu, ^{90}Sr, and ^{241}Am in common materials. The long capture length for ^{90}Sr betas impacts its use in lightweight RTGs.

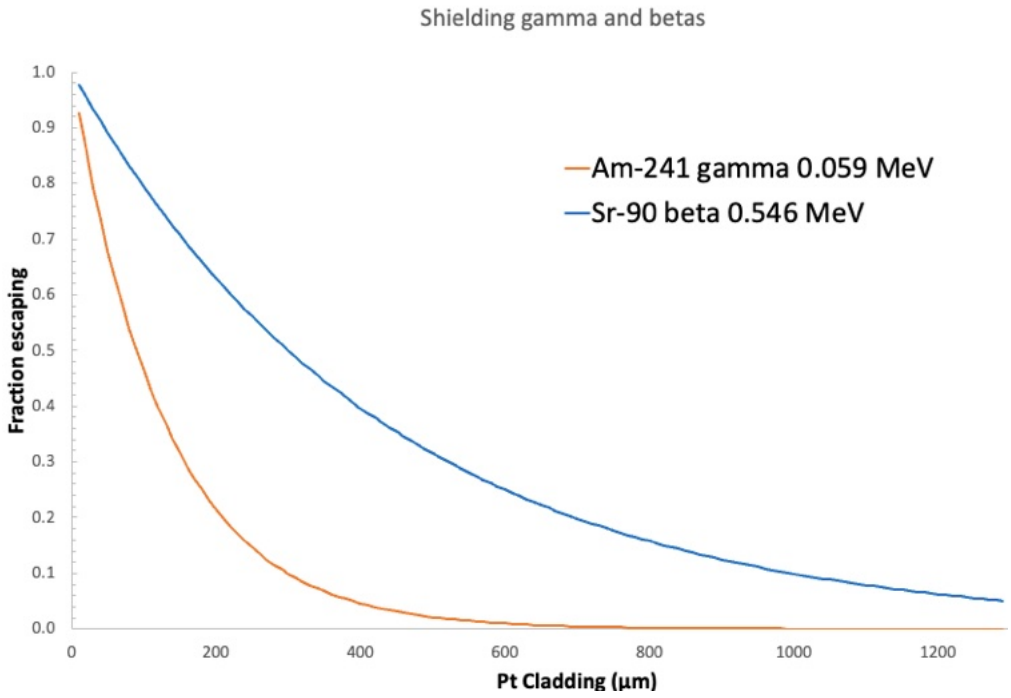

Figure 6. Fraction of beta (Sr-90) and gamma (Am-241) escaping of varying cladding thicknesses.

on the other hand, releases its energy in highly penetrating beta particles, requiring substantial amounts of material to capture the released energy. RTGs based on ^{90}Sr typically use large amounts of dense material to fully convert the radiation to heat as well as shield outside components and people from ionizing radiation, increasing their mass, and would have a negative impact on APPLE energy density. ^{241}Am is similar in some ways to ^{238}Pu, as it releases its energy primarily in alpha particles, but also releases 59 keV gamma rays, which penetrate farther than alpha particles, if not so far as the ^{90}Sr beta particles. While ^{238}Pu can capture essentially all of the energy (>99.9% of energy) within the Pt clad isotope core, ^{90}Sr would need 2-3x as much Pt to efficiently capture its beta particles shielding against ^{241}Am's gamma rays, which needs about 600 µm of Pt to capture 99% of the gammas, and 900 µm of Pt to capture 99.9% of the gammas. To achieve 99.9% capture of Sr-90 betas, the cladding thickness would need to be 3 mm thick. However, Sr-90 releases essentially 100% of its energy as 0.546 MeV betas, while Am-241 releases only about 1% of its energetic output at gammas. For the equivalent capture in Sr-90 Pt cladding as in AM-241, the Sr-90 clad would need to be 5 mm thick.

In addition, ^{238}Pu has higher volumetric and gravimetric energy densities compared to either ^{90}Sr or ^{241}Am, especially at end of life, as shown in Table 1. From this ^{238}Pu was selected as one of the primary radioisotope sources for this design moving forward, discarding ^{90}Sr. However, due to the constrained supply of ^{238}Pu, ^{241}Am was also selected, though the isotope radiation capture mass (Pt cladding) would need to be increased.

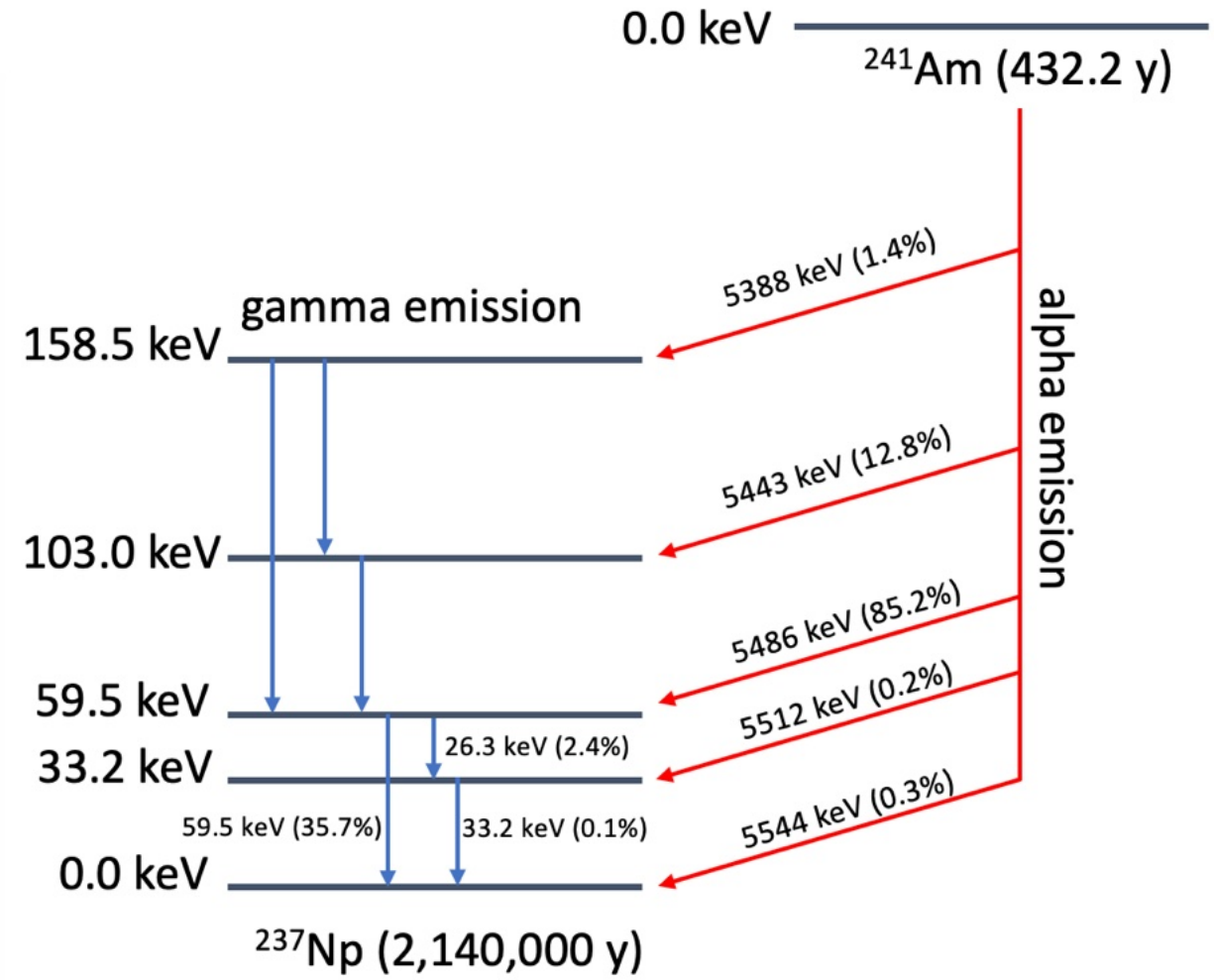

Figure 7. Am-241 decay scheme, showing predominant alpha emission for its decay to Np-237.

A key consideration in design of the APPLE RPS is the capture of the radioisotope decay emission to reduce damage to the thermoelectric components as well the adjacent electronic components of the spacecraft, in addition to protecting to integration and test radiation workers. To calculate the required cladding thickness for the ^{241}Am source, the first concern was to verify that a sufficient proportion of the isotope decay energy would be captured within the isotope oxide itself, or within the isotope cladding. For this, we simulated a continuous Pt cladding around the isotope core, and set a minimum of 99% of the radiation energy being converted to heat. Simulations of the Pu case confirmed that almost 99.9% of the energy was captured within the oxide itself, with very little additional energy conversion to heat was accomplished by the cladding. Figure 8 shows the capture depth within the Pt cladding for ^{238}Pu and ^{241}Am, indicating that >99.9% of the Pu energy is captured within the Pt cladding, while >99.8% of decay energy is captured within the Am cladding. The high capture rate for the isotope core and cladding is due to the high percentage of the energy that is emitted from these two isotopes in the form of alpha particles. These particles are efficiently captured and converted to thermal energy.

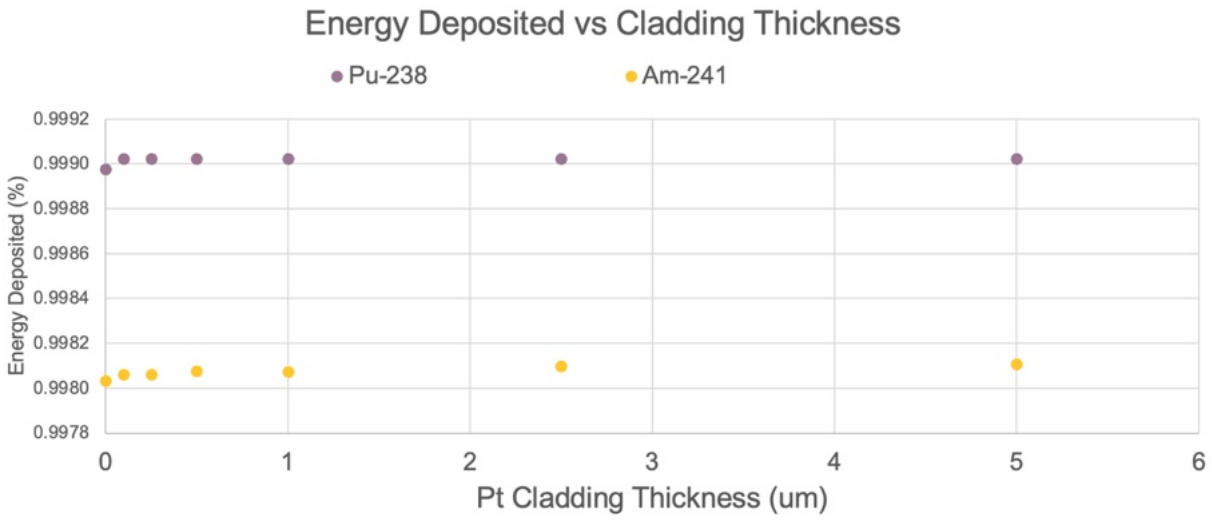

Figure 8. Simulations of the energy deposited within the Pt cladding for Pu-238 and Am-241.

^{241}Am decays to ^{237}Np primarily through α emission as well as low energy γ rays. As shown in Figure 7,[32] the decay of ^{241}Am to ^{237}Np proceeds through alpha particle emission to various excited states of Np. The residual nuclear excited state energy is then emitted through gamma rays to the ^{237}Np nuclear ground state, with the most populous gamma ray at 59.5 keV. The penetration depth of the α particles emitted by ^{241}Am is short in the Am_2O_3 as well as the Pt cladding, there are also some secondary particles produced by the interaction of the α particles with the oxide and Pt. The most concerning particles produced thorough these interactions are neutrons from the (α,n) reaction with the oxygen in the oxide, generating neutrons that are more difficult to shield than the primary α's. This secondary interaction however is rare and does not pose a significant radiation exposure risk.

2.2. Methodology

Radiation models and simulations for this project were developed within the GEANT4 simulation toolkit.[33,34] GEANT4 is well-validated for modeling space hardware and both nuclear and space radiation environments.

2.2.1 Solar and Galactic Radiation Exposure

For the APPLE components, the isotope radiation was not the only ionizing radiation risks. Due to the small and lightweight materials used in the APPLE design, external radiation sources are also an important source of potential damage.

We modeled the interplanetary space radiation environment for both solar particle event (SPE) and galactic cosmic ray (GCR) radiation. The space environment model was based on NASA's Badhwar-O'Neill 2014 model for GCRs,[35] the August 1972 SPE spectra as a "worst-case" example, and typical "average" SPE spectra and frequency based on solar cycle data.[36,37] Separate simulations were run to calculate dose equivalent from an average SPE, worst-case SPE, and daily GCRs. The effect of the 11-year solar cycle on the frequency and intensity of SPEs was also considered, and

the worst-case dose estimates were selected for each case. These sources were modeled in GEANT4 as large spherical sources with particles incident across a wide range of angles to simulate the space environment.

2.3 Calculated Radiation Dose

For the radiation evaluation portion of this project, the radiation dose from expected sources was calculated. Absorbed dose (D) is the fundamental dose quantity that describes the energy deposited by ionizing radiation. It has the SI unit of joule per kilogram (J/kg) or gray (Gy) and is given by:[38]

Equation 1.

$$D = \frac{d\bar{\varepsilon}}{dm}$$

where:
$d\bar{\varepsilon}$ = mean energy imparted by ionizing radiation
dm = mass

Absorbed dose was calculated in our simulations by collecting the energy deposited in the scoring volume (water phantom) per unit mass. This calculation was done within the GEANT4 code and also includes a calculation of the standard error of the mean dose deposited in the volume of interest. This data for SPE dose was calculated for 1 AU, and will decrease as $1/r^2$ for distance from the sun. Once in the outer solar system (past Mars) vehicle dose will primarily be from GCR, unless a worst case SPE occurs.

Dose to the APPLE materials per solar particle event (SPE) or galactic cosmic ray (GCR) "day" in interplanetary space was evaluated. The dose deposited in the materials from an "average" SPE, "worst-case" SPE, GCR protons (H), GCR alphas (He), and the remainder of GCR heavy ions (Z=3 to Z=26). We conclude that the dose due to "average" SPEs, "worst-case" SPEs, and GCRs are fairly constant throughout the materials. This agrees with what we expect from high energy, high atomic number (HZE) particles that are extremely penetrating and require a large mass of passive material to shield against.

Approximately past Jupiter's distance, dose accumulation from GCR dominates over SPE. After passing this distance, for any mission destination GCR will be the dominant source of radiation. This does not account for any additional radiation present at the destination, such as the high energy electrons and protons in Jovian radiation belts.[39]

2.4 Translation of Dose Equivalent to Dose

Doses calculated in simulation can then be compared to the doses deposited during laboratory radiation testing to begin estimating and calibrating the ratio of dose to battery material damage. A concern in comparing calculated simulation dose to measured laboratory dose is a consideration of units. Our simulations report absorbed

dose in the SI unit of Gy. This unit converts to the conventional unit of rad by a factor of 100. However, the laboratory measurements used in this work use dose equivalent, which is in the conventional unit of rem. Rem is a unit of exposure, not dose, and is designed as an equivalent dose for a human. The testing facility used for this experiment was designed for human exposure rather than to simulate space exposure. This rem unit can be converted to the dose equivalent SI unit of Sv by a factor of 100, but the conversion between absorbed dose and dose equivalent still remains.

Absorbed dose is scaled to dose equivalent via one of several methods including the radiation quality factor (Q), relative biological effectiveness (RBE), or radiation weighting factor (w_R) to account for the relative biological effect of different types and energies of ionizing radiation (ICRP 2007). For the purposes of this project, the laboratory sources have low RBE (~1) and thus the margin of error between converting absorbed dose and dose equivalent is very small. For this specific case, we can compare the absorbed dose from simulation (Gy) to the dose equivalent measured in the laboratory (rem converted to Sv) without significant concern for conversion error.

2.5 Skutterudite Ionizing Radiation Hardness

The skutterudite thermoelectrics will be exposed to ionizing radiation potentially from the isotope source, but also potentially from the space environment. As shown previously in Phase I, the galactic background radiation as well as solar flare particles are the primary source of ionizing radiation for the APPLE unit. Stability of the thermoelectric properties of the SKD materials is needed for long term operation of the APPLE device, especially for missions with long transit times. Figure 9 shows the APPLE design with the SKD legs sandwiched between CU hot and cold shoes, Pt cladding around the isotope sources (^{238}Pu and ^{241}Am), and an Al radiator facing the space environment. The two SKD materials (p-type $Ce_{0.9}Fe_{3.5}Co_{0.5}Sb_{12}$, n-type $Yb_{0.15}Ba_{0.05}Co_4Sb_{12}$) were then simulated for total accumulated dose for a representative long duration Mars mission. The mission was assumed to be 9 months of transit time, and total operating time of 15 years. Depending on the approach to Mars and the solar activity, there is a high variability in total dose, as a large solar flare could cause substantial variation in total accumulated dose. The calculation included radiation from the Am and Pu isotope source generated isotopically within the isotope

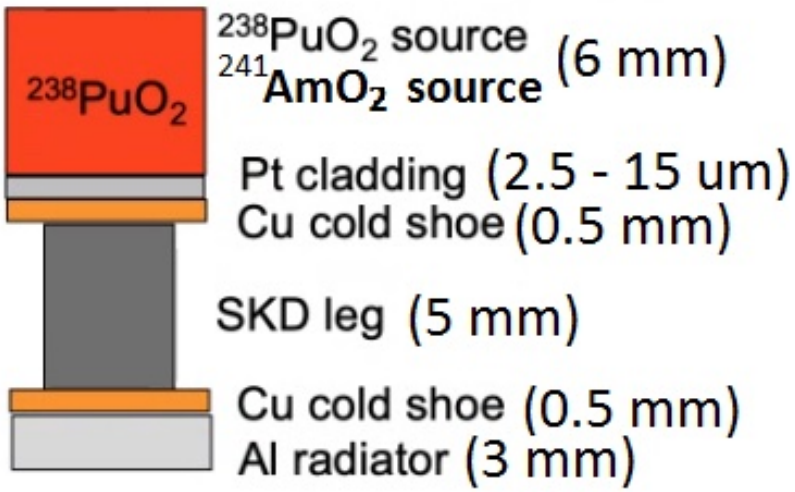

Figure 9. SKD leg geometry and shielding arrangement from ionizing radiation.

oxide. For solar flare event, a 90% worst case event was assumed, with 1.32E10 particles and 1E9 cm^{-2} average flux. The solar wind was simulated as 2.79E17 protons, low energy 0.0005 MeV and high energy 0.002 MeV. Total dose within the SKD leg types was calculated, and found that for Pu APPLE, the primary dose was from external source, while the Am APPLE had much more dose from the Am isotope core. This internal dose in this calculation is with only 10 μm of Pt protecting the thermoelectrics from the isotope particles. This isotope dose can be reduced 10x for every 300 μm of Pt clad above the minimum 10 μm of Pt simulated in this case. Outside of radiation belt destinations such as Jovian orbits, inner solar system missions would see most dose as solar particles are the dominant ionizing radiation. Dose was calculated in "Equivalent neutron flux," the number of 1 MeV neutrons per cm^2 passing through the sample that would deposit the same dose as environmental simulated conditions. This is a standard dose metric allowing for comparison across different radiation environments and radiation types.

Figure 10 shows the calculated dose for the n- and p-type SKD legs from the isotope and from the environment. For the Pu APPLE case, the majority of the dose comes from the environment, with 4E14 neutrons per cm^2 for both n- and p-type legs. However, for the Am case, far more dose was accumulated from the residual unshielded radiation from the isotope clad. The relatively low amount of environmental dose for both types of devices comes from the exterior shielding, as 3 mm of Al is a very good radiation shield for spacecraft. It should be noted that the connection between calculated gamma equivalent neutron dose (the primary ionizing radiation from the Am-241) and neutron testing is imperfect and needs investigation.

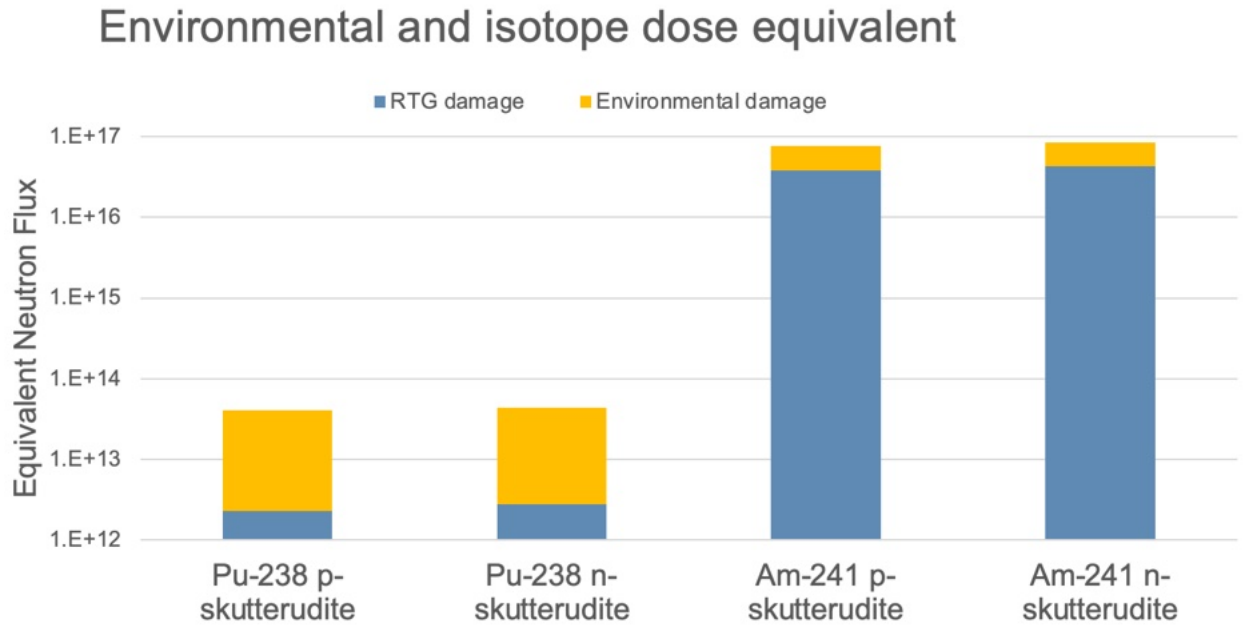

Figure 10. Total dose in the SKD legs from isotope sources (blue) and external sources (yellow) such as solar flares and solar wind.

To evaluate the radiation hardness of the SKD materials, JPL performed neutron irradiation of the SKDs, as the TE materials are potentially susceptible to displacement damage from radiation. In the TE materials lattice thermal conductivity and other properties may change due to the radiation induced displacement damage. To evaluate a Pu-type RTG on a mission to Europa, the total fast neutron fluence tested was 2.4E13 n/cm^2 and showed minimal effects on n- and p-type SKD materials' thermal and electrical conductivity. The thermal conductivity actually increased ~2% for both types of materials, and the electrical conductivity was essentially unchanged. APPLE's estimates for equivalent unshielded neutron flux are about 1000x this tested dose in the Am-241 case. This Am-241 radiation can be reduced 10x per 300 μm of Pt added to clad, allowing for potentially reducing this dose. In addition, the equivalency between 'equivalent neutron dose' and actual neutron testing is weak for gamma radiation, as the two types of radiation are the most different in interactions of material. Finally, the neutron testing essentially showed no effects on the SKD performance, but further testing is warranted to ensure that the SKD materials can either withstand the Am-241 source or be sufficiently shielded from degradation.

2.6 Cladding Design

The isotope oxides will be contained in a platinum clad for several reasons. The metal clad has a high melting point and low reactivity with the isotope oxides under the expected operating temperatures (500-600˚C). Testing[40] at Oak Ridge National Laboratory found that Pt and related alloys with Rh did not show signs of oxidation from exposure to oxides at temperatures up to 1200˚C and melting points of 1700˚C. These high temperatures are also required for launch safety operations, as in the case of an explosion or fire from burning of fuels from rockets, including liquid hydrogen, kerosene, or methane. The clad is intended to contain any powder or fragments of the isotope oxides that may happen from handling, thermal expansion, or other mechanical impacts. The containment of the oxide particulates is a key safety requirement to prevent dangerous radiation exposure to humans. While as discussed above the alpha particles have very low penetration depths, often less than exists in the outermost layers of dead skin or clothes from exposed workers, ingestion of alpha emitter is a severe radiation hazard, and must be prevented. Metals are ideal for containment of particulates, as they are both hard and high melting point, but also have elastic flow mechanical failures. Under impact metals, unlike ceramics or composites, undergo plastic deformation rather than fracturing, which would potentially allow for the release of isotope particles.

In addition, the isotope clad for Pu-238 and Am-241 also requires a gas release mechanism, as the alpha particles emitted by each isotope will eventually accumulate electrons from their environment and become helium atoms. This helium gas will accumulate and create pressure in the clad, potentially leading to failure if not released. To this end, clad designs for alpha sources typically have a gas release mechanism in the form of a metallic frit, composed of sintered metal such as Pt. A Pt sintered frit would not significantly reduce shielding effectiveness, but would permit the release of small amounts of He gas over time. Over a 15 year operational life, the 0.6 mol of AM-

241 in a single clad would generate about 1.6L of He gas at STP. Buildup of this gas within the clad over life could lead to internal stresses that may deform or fracture the clad structure.

As seen above, the thickness of cladding required to capture the energy from the Pu and Am isotopes is very thin, verging on unnecessary. Within 5 μm of Pt <99.8% of the energy is captured. However, thicker metal clads are needed as mentioned above for mechanical containment, and indeed, 5 μm of Pt would be insufficient to ensure plastic deformation in the event of impact, and in fact be so thin as to be very difficult to work with. In addition, while the majority of the energy is captured within the oxide and clad, there is still residual penetrating radiation that escapes, typically secondary neutrons from the alpha particle interactions for the Pu case, and the addition of a small amount of gamma rays from the Am case. Both of these sources need to be considered in clad design, as well as for potential worker hazards when building and testing any components utilizing the APPLE system.

To evaluate this, we calculated the dose for a radiation worker that would be handling an APPLE source, typically while integrating it into a spacecraft, payload, or other application. The United States Nuclear Regulatory Commission has an annual total effective dose equivalent limit for the whole body is 0.05 Gy.[41] Assuming and average of 1 m separation between the worker and the APPLE isotope clad, and using only a minimum of Pt shielding of 10 μm (an no other shielding in the form of components), no measurable dose reached the radiation worker 1 m from the Pu-APPLE clad. The alpha particle absorption by the isotope oxide and clad is essentially perfect. The maximum dose deposited by the Am-APPLE unit over 100 hours at 1 m is 0.004 Gy per Am-APPLE unit (161g of Am_2O_3) and for a 10 μm thick Pt clad. For 10 units, 17 W_e for the application, this gives a total effective dose equivalent of 0.04 Gy, just below the dose limit for the 100 hours. This dose can be reduced 10x with the addition of 300 μm of Pt cladding, and reduced by 10x for each additional 300 μm of Pt used. 300μm of Pt cladding adds 22g of mass per 161g Am-241 core, or ~13% more mass for the total device. For mechanical reasons, the need to be able to mill out the clad prior to filling with isotope, 1 mm is a more practical thickness for the Am-241 core, resulting in a reduction of the 0.004 Gy per APPLE radiation dose 2000x. A 1 mm thick clad adds 79g of Pt, or a 50% increase in total clad mass over 10μm of Pt cladding. As noted above, the 5-10μm thick Pt cladding is impractical and insufficient for handling and mechanical protection, showing that there is no significant radiation hazard for human handling or electronics impact from an intact isotope clad. For context, the amount of absorbed dose for a transcontinental flight is 0.000035 Gy,[42] so 1750 hours exposure at 1m of an Am-PPLE would be equal to the absorbed dose of one flight.

2.7 Mission Applications

The above simulations and calculations apply to an APPLE mission solely to interplanetary space where the space radiation environment has been characterized by prior sensors and spacecraft. If APPLE is to be dispatched on a mission to a new or poorly characterized environment, new models, estimates, and simulations will be

required. For example, if an APPLE mission were to spend significant portion of its mission in the near vicinity of the Sun, another planet, moon, or asteroid, additional considerations regarding trapped radiation (similar to Earth's Van Allen belts), X- or gamma ray radiation, albedo (reflected) radiation from the surface, etc. must be considered and accounted for.

In the example of a direct transit 2-year Jovian mission, APPLE would spend the majority of its time in interplanetary space, which we have simulated and studied as part of this project. During the portion of the mission in the Jovian environment, however, additional trapped electron radiation will likely be present. Additionally, a portion of the SPE and GCR radiation will be blocked by the planet itself, so additional simulations will be needed based on the specific geometry and location of the vehicle to determine the effects to total dose in the Jovian environment. This would apply to any mission destination that has significant radiation source, and should be simulated for each mission path. For a lunar mission, the unit would be exposed to the GCR continuously, though at ~1/2 the deep space level as one direction (local down) is perfectly shielded from the GCR by the regolith. It would also be exposed to SPE during the lunar day, and would need to accommodate the space weather based on the solar cycle, but this would be as shown above, the primary source of radiation dose compared to the GCR as it would be in the inner solar system.

2.8 Next Steps in Phase III

Proposed follow on work for this segment of the project include improved fidelity of the radiation simulations. Specifically, we plan to update the geometry as the overall design advances with increased knowledge of the battery structure and thermal environment. We also plan to conduct further scenario-based simulations for a variety of potential mission types, such as radiation simulations of the high energy radiation belts around Jupiter, and lunar SPE forecasting. This will allow the team to focus laboratory radiation exposures on the most feasible mission concepts.

3. Battery Design and Testing

3.1 Need for a Solid-state, Radiation Hard Battery

A radiation hard, solid-state battery is needed for the APPLE design due to the potential incident radiation from external radiation sources such as solar particles and galactic cosmic radiation, as noted above. Due to the long duration of the missions planned for using APPLE, 15-50 years, the expected dose of radiation to the battery can be high. As seen in destructive physical analysis of conventional Li-ion batteries (Figure 2), the organic components of conventional cells degrade under ionizing radiation,[43] even when in a steel case where the jelly roll design results in substantial self-shielding. With the proposed small scale design of the battery in APPLE, the lack of a solid metal case for the cell components, and the necessary placement of APPLE on the exterior of the vehicle the battery materials will be uniquely exposed to radiation during mission. To avoid degradation over life, a solid-state, radiation hard battery was proposed. This design would remove the organic electrolyte, typically a carbonate, ether, glyme, or polymer in favor of a solid ceramic material that would not be able to polymerize in response to an ionization event.[44] In addition, this material has a much higher operational temperature range, unlike the organics, which are typically restricted to a narrow (20˚C $\pm$ 10˚C) temperature range. The typically wide temperature operating range of ceramic electrolytes (20˚C to 200˚C) allows for the removal of active battery temperature regulation, and to use passive regulation based on the generated heat from the isotope decay and a radiator. This not only removes a failure prone system, but also reduces the bus power needed to regulate battery temperature from the power requirements, allowing for a smaller power source.

Neutron irradiation is also a concern for the APPLE battery. Plutonium(IV) oxide Am(III) oxide emit alpha particles which interact with the oxide material to produce neutrons, more than ^{238}Pu and ^{241}Am metals, at the rate of 2.1x10^{4} n/sec/g of plutonium-238[45] and 2.7×^{103} n/s-g of americium-241.[46] This production of neutrons is approximately 10x the neutron flux from ^{238}Pu, with the remaining flux of neutrons coming from the interaction of the ^{238}Pu alpha particles interacting with the oxygen atoms of the oxide, particularly the ^{18}O components which have a higher alpha particle cross section than ^{16}O. This production of neutrons from the isotope source is the reason that ^{7}Li was investigated as the lithium isotope for the radiation hard battery, even though natural Li sources are ~93% ^{6}Li.[47] ^{6}Li has a cross section for neutron capture approximately 29,000x higher than ^{7}Li.[48] ^{6}Li when undergoing neutron capture produces a triton and an alpha particle, which both destroys the ^{6}Li needed for energy storage chemistry, but also generates particles (^{3}H, He)[49] which will form gasses that can nucleate inside the battery forming stress bubbles which can fracture the solid-state battery structure and further reduce battery performance. Using ^{7}Li was determined to be critical for a battery in any proximity to alpha sources like ^{238}Pu and ^{241}Am. The neutron flux from the alpha source will not be significantly shielded before it reaches the battery in either the initial design

of APPLE, with the battery at the hot shoe, mounted on the isotope source, or in the final Phase I design of APPLE with the battery at the radiator interface.

3.2 Solid-state Radiation Hard Battery

Battery fabrication was constructed from isotopically enriched materials grown in thin film form based on the well-established lithium phosphorus oxynitride (~$Li_{3.3}PO_{3.6}N_{0.36}$) (LiPON)[50,51] based all solid-state battery[52,53] developed[54,55] at the Oak Ridge National Laboratory.[56,57] Briefly, these cells consist of vapor deposited cathode films grown on a platinum coated Al_2O_3 substate. The cathode films were annealed at 700°C in air to compensate for oxygen deficiency and crystalize the materials. A 1 mm glassy LiPON solid electrolyte (~$Li_{3.3}PO_{3.6}N_{0.36}$) was vapor deposited on the cathode followed by a thickness matched silicon film (full cell configuration) or 2 mm Li metal. Silicon was chosen for radiation tolerance and high temperature electrochemistry; Lithium was chosen to explore the cathode chemistry more rapidly.

The cathode in this work was selected to be $LiMn_{1.5}Ni_{0.5}O_4$. This material is a cubic spinel that has an operating voltage of 4.9V (vs. Li/Li^+).[58] The benefit of this approach is multifold. First the cubic spinel structure (Figure 11)[59] allows faster Li-ion transport than the layered 2D materials like $LiCoO_2$ that were explored in Phase I. The faster transport is envisioned to allow faster discharge rates during use. This is important as the final electrode needs to be on the order of 40 mm to get appreciable energy densities and higher discharge rates will produce more pulsed power. Second, the cubic phase is more dimensionally stable than the layered materials during extended cycling preventing materials degradation. Finally, the 4.9V potential will produce 20% higher power than typical LCO cathode. The challenge we tried to address was the synthesis and scale up of this material. Further, we wanted the material to contain exclusively ^7Li to minimize neutron radiation capture and resulting daughter products generating high energy particles causing defects within the electrode and the resulting loss of electrochemical performance. LMNO thin film electrodes have been investigated by ORNL in 2015. These materials were cycled at rates of 5C but were only a few microns thick. Figure 12 shows cycling data for the LMNO films in the solid-state.[60]

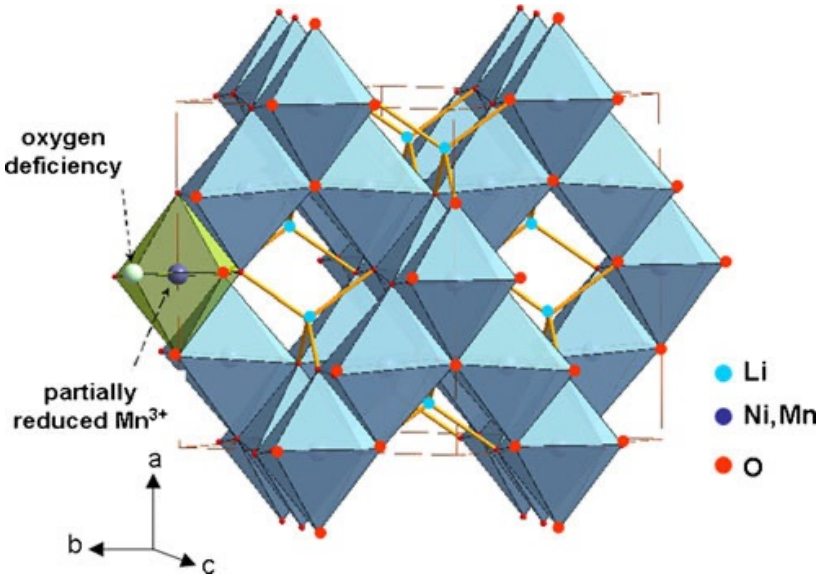

Figure 11. Schematic representation of the cubic spinel LMNO investigated for this work.

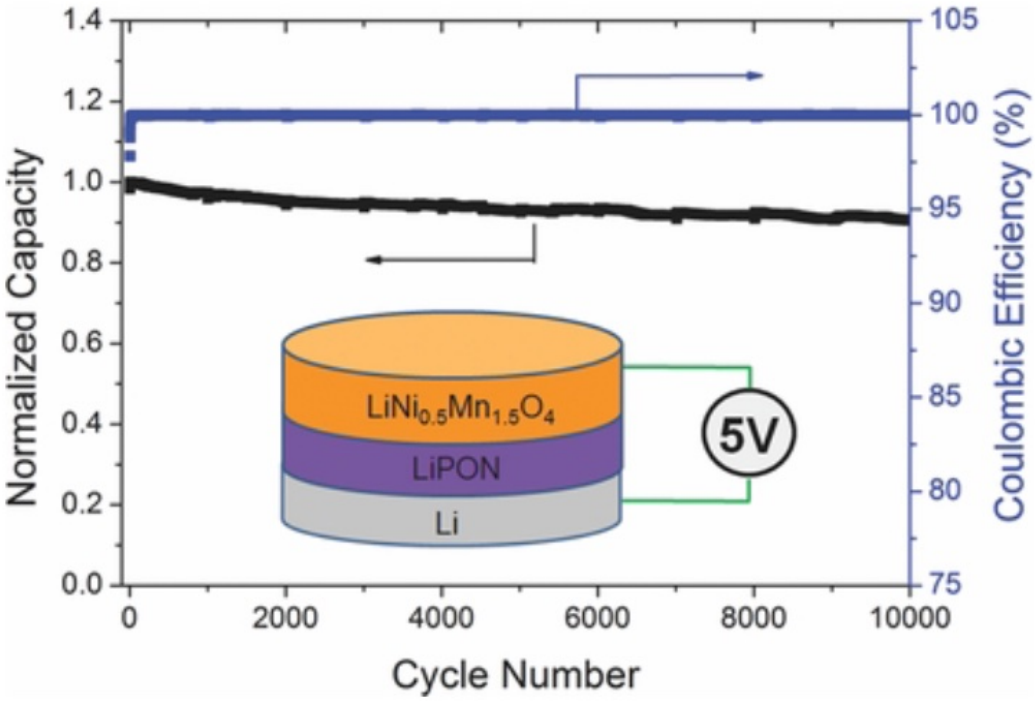

Figure 12. Electrochemical cycling data for few micron thick LMNO cycled at 5C and room.

3.3 Battery Fabrication

For this work we focused on surrogates for isotopically enriched cathode materials. The idea was to process materials in the same way as one would theoretically process the ^{7}Li materials. In this case multiple approaches were undertaken to fabricate the LMNO targets. This proved to be a major challenge. Multiple sets of targets were fabricated with different lithium stoichiometries ($Li_xMn_{1.5}Ni_{0.5}O_4$ where X = 1.0, 0.75 and 0.5). The range of compositions was due to the preferential sputtering of Li during the film growth creating a film that was lithium rich resulting in extensive Mn^{3+} redox activity. By reducing the Li content ideal stoichiometries of LMNO were more likely to be obtained. This means that the starting materials are not thermodynamic line compounds but mostly likely heterogeneous mixtures of various spinel phases. A representative image of a fabricated sputtering target is shown in Figure 13. The gold layer on the side is part of the bonding process.

Figure 13. Image of combustion synthesized sputter target after bonding (gold layer).

3.3.3 Solid-state synthesis

In this process Li_2CO_3, $NiCO_3$ and $MnCO_3$ were ball milled for 24-48 hours to ensure mixing. The materials were heated at 700°C in air and the final material was isostatically compressed to 2000 lb/2 in^2 and sintered at 900°C for 18 hours in air. The resulting material was bonded to indium foil and mounted on a copper cooling plate.

3.3.4 Combustion synthesis

The mechanical issues with the solid-state synthesized LMNO (*vide infra*) necessitated the formation of smaller LMNO precursors to ensure stress free consolidation. Using a proprietary combustion synthesis process (fuel is withheld as proprietary and highly dangerous to those not experienced in the art) metal nitrates were mixed in solution and heated on a hot plate to ignition resulting in a black MNO precursor, Figure 14 (left). Note the combustion synthesis of Li-materials is highly dangerous due to the exothermic reaction. Therefore, Li_2CO_3 was added to the resulting MNO material through wet milling in isopropanol. The dried precursor Figure 14 (right) was isostatically pressed at 2000 lb/2 in^2 and heated to 1000°C for 18 hours in air. The resulting pellet was approximately 92% dense.

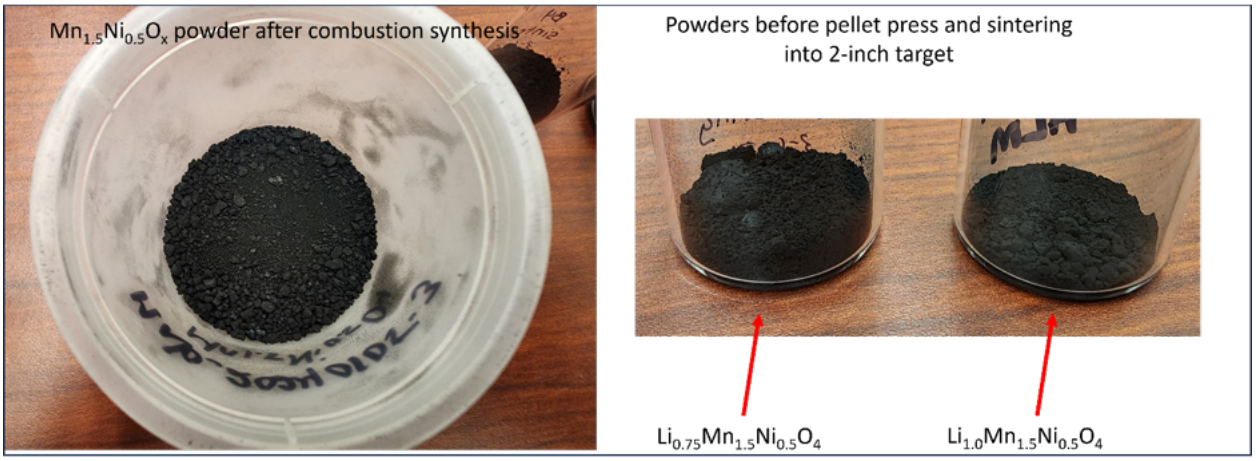

Figure 14. Image of combustion synthesized LMNO powders used for sputter target fabrication.

3.3.5 Current Collectors

For the batteries investigated in this work double side polished lapped alumina (Valley Design Substrates) were used as supporting media. The materials are surrogates for thinner current collectors and not representative of a real potential battery which would use a thinner substrate for better heat conduction and weight to energy ratio. A set of masks were used to confine the current collector (2 cm^2 active area) as part of the build. Heterolayers of a cobalt underlayer followed by platinum metal were deposited on the alumina. For an unknown reason the heterolayers play a role in the nucleation and growth of the cathode. Indeed, without the 20 nm cobalt a LCO film grown on a 1 mm Pt layer will become poorly crystalline. Figure 15 shows images of the current collector and substrates.

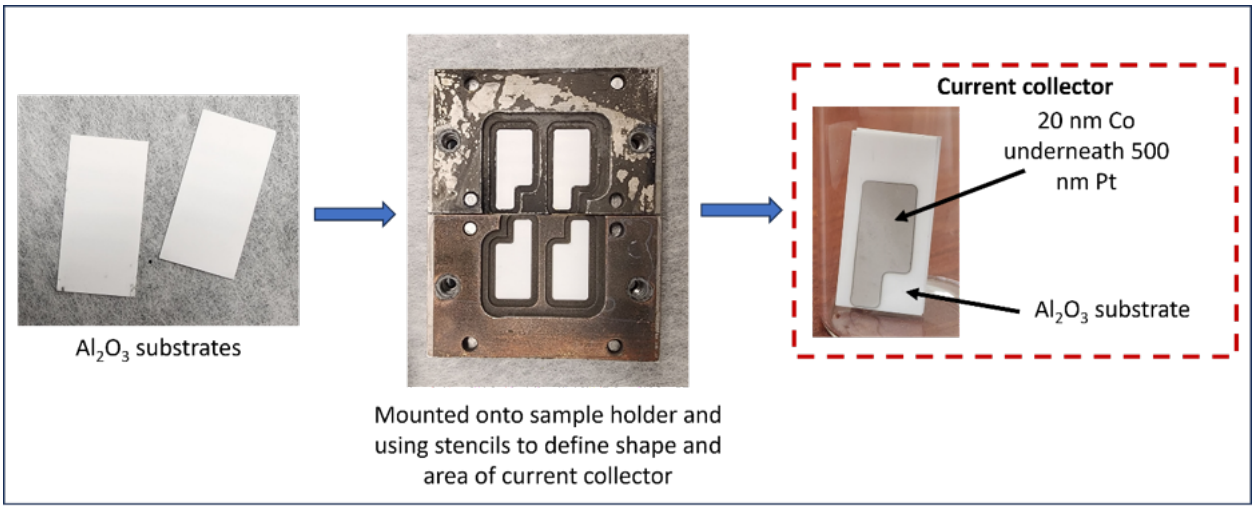

Figure 15. Image of corundum substrates (left), substrates with masks (center), and substrates after Co/Pt deposition for battery current collectors.

3.3.6 Cathode growth

The batteries in this project were made by physical vapor deposition. The 2" diameter targets were mounted to a sputter source and r.f. sputtered at an applied power of 70-140 watts in argon gas. Key variables include distance from substrate to target and deposition pressure. These two variables control the energy of the deposited ad-atoms and the resulting stress in the cathode films. Film depositions took 2 to 60 hours depending on film thickness. Figure 16 shows an image of the deposition chamber while depositing the LMNO films. The mauve plasma is indicative of an argon plasma with nickel being deposited.

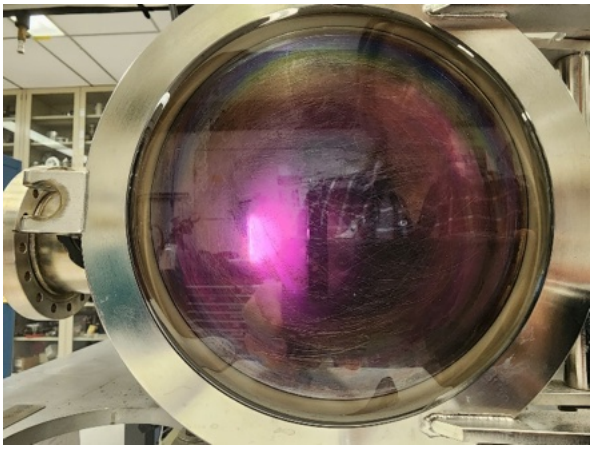

Figure 16. Image of argon plasma during deposition of LMNO.

Figure 17 shows representative cathodes deposited on the Pt current collectors using the shadow masks (black area). The as grown film is confined to the working area of the Pt current collector. The films were collected and annealed in an oxygen atmosphere for 1-2 hours at 700°C to crystalize the cathode crystal structure. In parallel circular witness samples were prepared (Figure 18) as a control to evaluate the electrochemistry of the LMNO. These small samples were loaded in standard Swagelok type cells and cycled in liquid electrolytes to measure the electrochemical properties and estimate the available Li-inventory for use during cycling. This set of experiments was a control to experimentally measure film thicknesses. During the deposition the film growth rate was estimated using a quartz crystal microbalance. The problem is the resulting films were highly Li rich (even with the Li-deficient target)

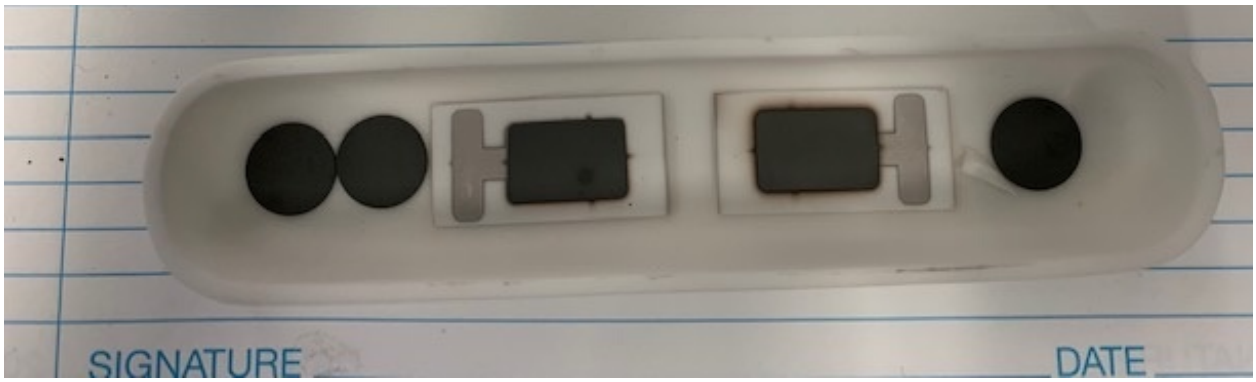

Figure 17. Image of LMNO samples on circular disks and 2 cm2 solid-state batteries post 700oC oxygen anneal.

producing films with lower densities than LMNO and lower materials modulus which effectively increased the film thickness over what was expected based on the properties of LMNO. This will manifest itself in higher apparent capacities.

One problem was identified during the synthesis of the cathodes. The sputter targets were under a great deal of stress during the deposition causing extensive cracking and degradation of the cathodes. This degradation is evident from the images presented in Figure 18 which show two of the targets prepared post depositions for 60 hours. It is evident the bonding process holds the targets to the backing plate but crack propagation occurs throughout the targets. For this reason, extensive work was performed using the combustion synthesized sputter targets which had much less mechanical stress compared to the traditional solid-state process. The data presented from here on uses these combustion grown targets. It was observed that targets with less Li content were more mechanically robust during cycling. The origin of this effect is unknown.

The annealed substrates were reloaded into the deposition chamber for LiPON coating. LiPON is a glassy electrolyte material with a composition of ~$Li_{3.25}PO_{3.87}N_{0.17}$. The material is stable against lithium metal and up to 5.5 V (vs. Li/Li^+).[61] LiPON is grown by

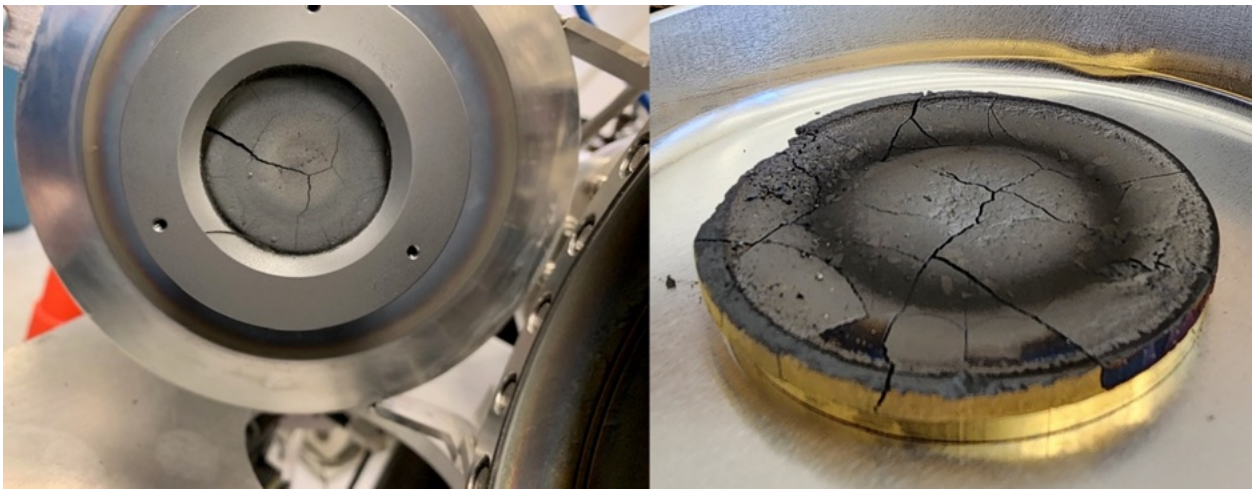

Figure 18. Image of LMNO sputter targets from solid-state LMNO synthesis demonstrating extensive cracking and failures post deposition.

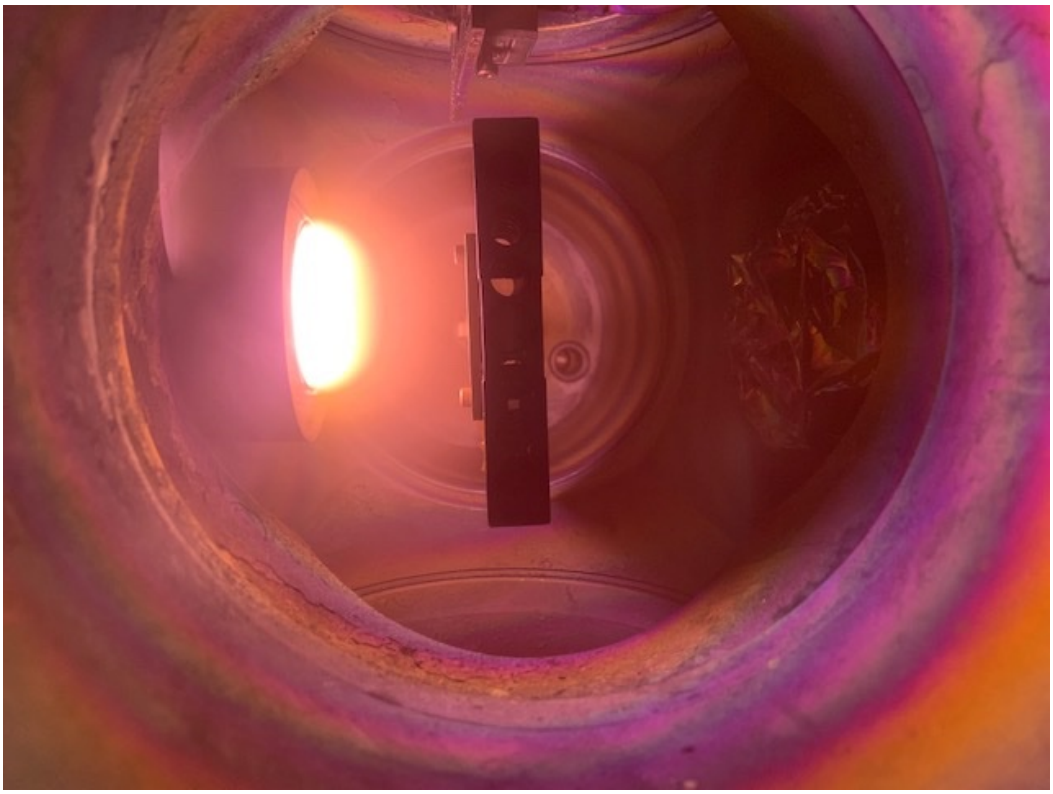

Figure 19. Image of sputter deposition of LiPON in N_2 plasma.

sputtering a Li_3PO_4 sputtering target in a pure N_2 plasma (Figure 19). During the deposition process nitrogen is incorporated into the film and charge balanced is maintained by pulling in additional Li from the sputter target.

Figure 20 shows images of the setup before LiPON deposition. The LiPON area is larger than the cathode area to avoid electrical shorting. After deposition a characteristic yellow layer (Figure 20 (center)) is evident in the images consistent with the growth of about a 1 mm LiPON layer. Several challenges were observed at this point as evident in Figure 20 (right) where after LiPON deposition on thick cathodes

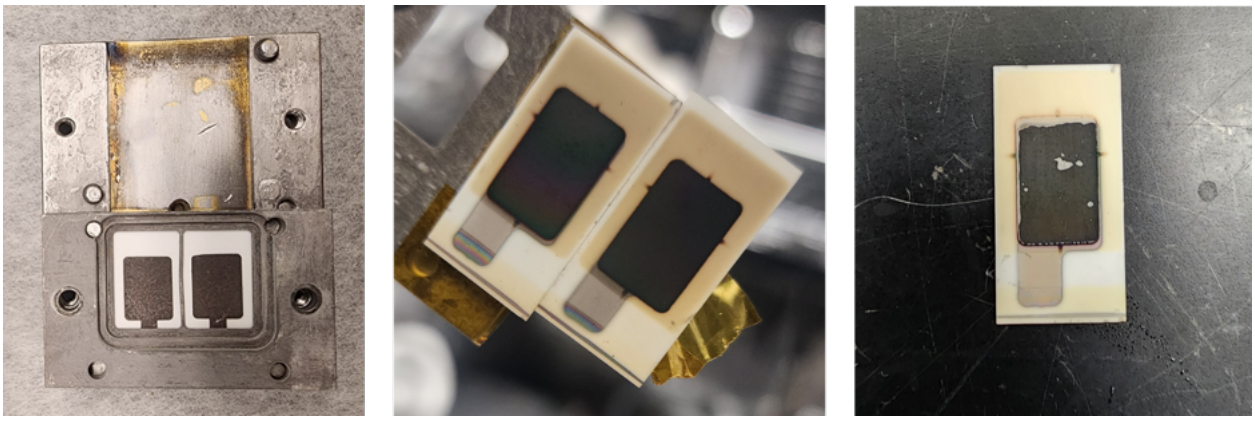

Figure 20. Image of substrates with LMNO films (left), samples after LiPON deposition showing the yellow LiPON film (Center), and 20 µm LMNO film with 1 µm LiPON causing the LMNO to spall from the surface (right).

(>15 mm) spalling of the cathode was observed. This is likely due to mechanical stress the cathode is under where the mechanically tough, compliant LiPON coating causes pressure release and flaking of the films. This challenge could be ameliorated with the application of stress measurements through optical profilometry and a short study on the stress/deposition pressure/composition relationship. There was not enough time or resources to complete this study for this project.

Cathodes less than 15 mm thick were loaded into a lithium deposition tool (Figure 21-left) where 5 mm of lithium metal were thermally evaporated onto the stack. Figure 21-right shows an image of the final cell. The lithium extended away from the cathode current collector (metallic area to the top of battery). The shinny metallic lithium is evident in the center of the battery overtop of the black LMNO cathode. In this work we used the lithium metal as the anode current collector as it is soft and makes a good electrical contact with the potentiostat.

The batteries shown in Figure 20 (right) were loaded in stainless steel cans shown in Figure 21. In this configuration the cells were sealed under argon in a glove box but could be viewed during cycling to observe morphological changes. Alligator clips were used to grip the Pt and Li current collectors for the cathode and anode respectively. The samples were connected to a Maccor battery cycler with a 2TW input impedance to avoid electrical shorts.

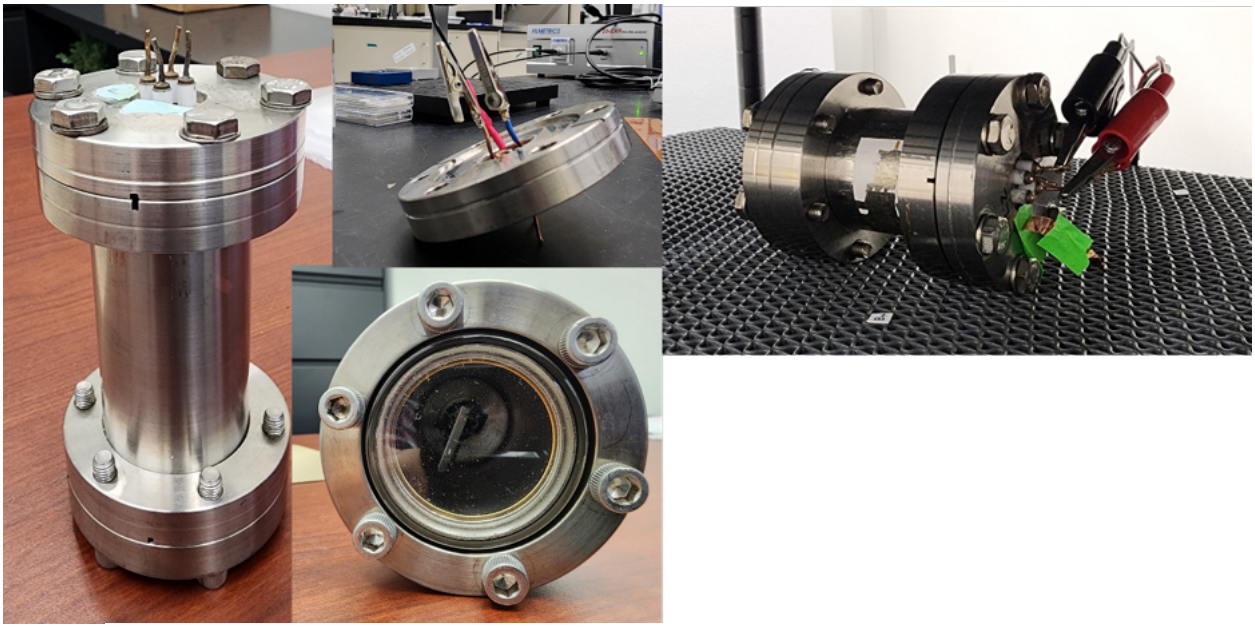

Figure 21. Test fixtures for cycling thin film batteries.

3.4 Electrochemical Cycling Data

Example cycling data is presented from 4 sets of batteries. Numerous other batteries shorted or delaminated prevented their cycling. The shorting is believed to have occurred from small areas spalling off or lithium electrodeposition on the cathode. Second, a key parameter to follow in these measurements is cell open circuit voltages.

The OCV is a measure of the starting chemical potential of the cell. Voltages less than 3V are indicative of excess Li. This would be analogous to turning the cathode into an anode. Such over-lithiation can occur in $LiCoO_2$ and other transition metal materials.[62] A typical OCV voltage should be 3.3 V (vs. Li/Li^+). Note the data presented here was collected on lithium anode cells. These cells were investigated first to explore cathode chemistry without having to introduce a new variable with the sloping voltage profile of the next generation silicon anode.

Figure 22. Image of ORNL Li deposition tool (left) and LMNO/LiPON/5 µm Li heterostructure after deposition (right).

Figure 23 shows Li:LMNO cycling data for LMNO deposited from $LiMn_{1.5}Ni_{0.5}O_4$ target material. The LMNO was annealed in O_2 for 1H at 700°C and had a theoretical thickness of 8 mm. There are several characteristic features of the cycling data. First, the OCV data shows a potential of 2.7V (vs. Li/Li^+) indicating a slight excess of lithium within the electrode. Upon charging there is a small plateau at 3.75V consistent with a small amount of Mn^{3+} being oxidized to Mn^{4+}. This oxidation is attributed to the small excess of Li within the electrode evidenced in the OCV data. Upon charging the cell exhibits a plateau at a potential of 4.35 V. This potential is less than the expected voltage plateaus of 4.65 and 4.75 for the Ni^{2+} to Ni^{3+} (4.65V) to Ni^{4+} (4.75V) redox states. The first charge profile exhibits a capacity of almost 200 mAh/g cathode. Together this electrochemistry data is consistent with the formation of $LiNi_{1/3}Mn_{2/3}O_2$ layered cathodes which have a capacity of about 180 mAh/g and a flat voltage profile consistent with what is observed in these materials.[63] This cathode has approximately the right Mn to Ni ratio 66:33 (versus 75:25 theoretically) consistent with off-stoichiometry of LMNO. Together this indicates that the material has picked up extra

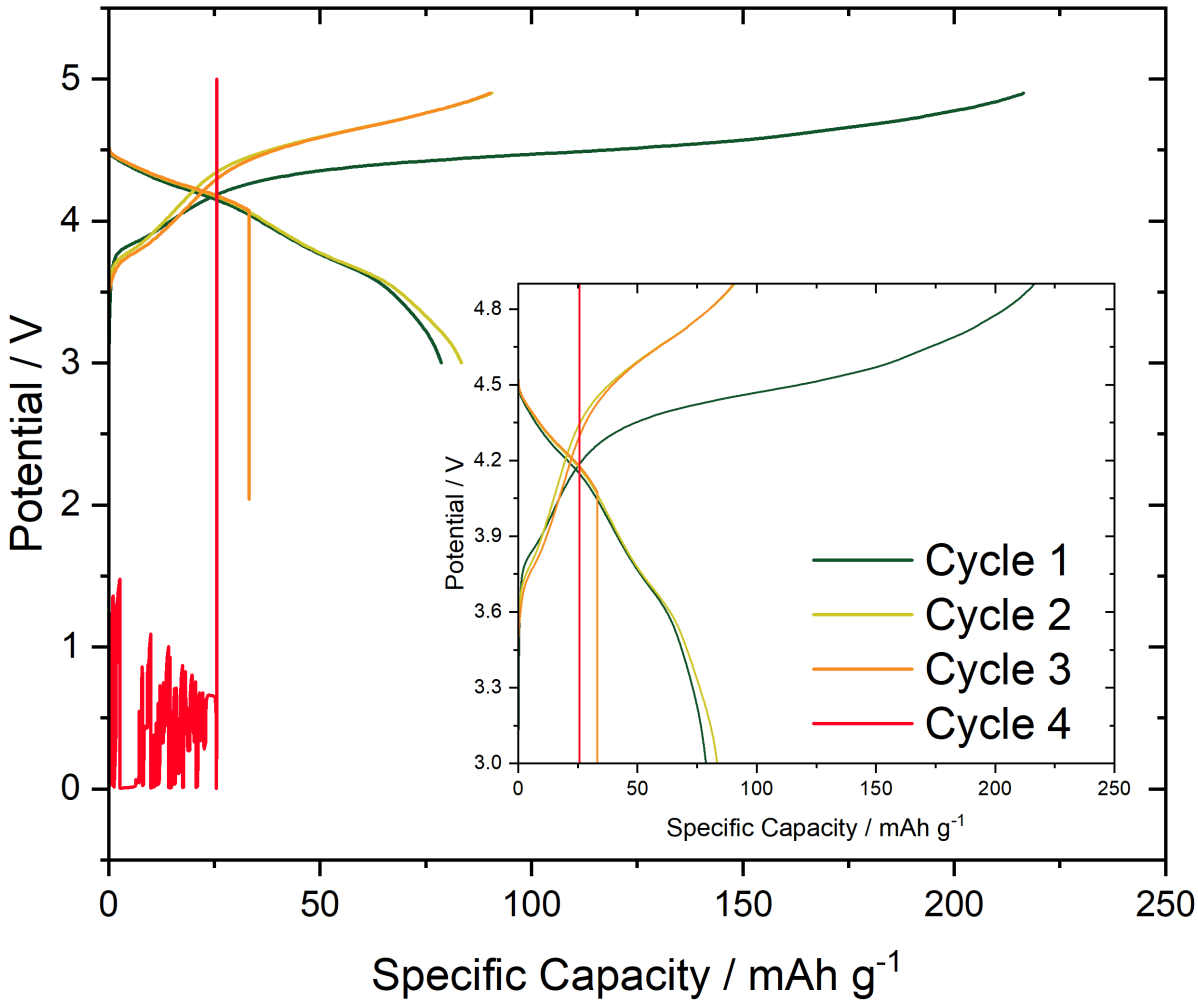

Figure 23. Cycling performance of LMNO from $Li_1Mn_{1.5}Ni_{0.5}O_4$ sputter target. Films annealed at 700˚C for 1h in O_2.

lithium within the grown film and shifts the structure from the cubic spinel to the layered oxide. The cell shorts after 4 cycles consistent with mechanical degradation of the materials from over charging to 4.9V and the resulting delamination.

Figure 23 shows Li:LMNO cycling data for LMNO deposited from $LiMn_{1.5}Ni_{0.5}O_4$ target material. The LMNO was annealed in O_2 for 2H at 700ºC and had a theoretical thickness of 8 mm. This 2h anneal is longer than the previous sample and is known to promote Li reorganization within the electrode (including evaporation). The voltage profile of this cell evolves significantly compared to the previous cell. There is still a voltage plateau at 3.75V consistent with a slight concentration of Mn^{3+} from excess Li. Further, there is still a large voltage plateau at 4.3 V consistent with the layered $LiNi_{1/3}Mn_{2/3}O_2$-type cathodes. However, upon cycling one notices a significant shift in the voltage profile to higher potentials (~4.7 V) which is evidence of approaching more spinel like structural composition. Further the capacity retention of this particular phase is significantly improved over the layered containing cathode (i.e. $LiNi_{1/3}Mn_{2/3}O_2$) which

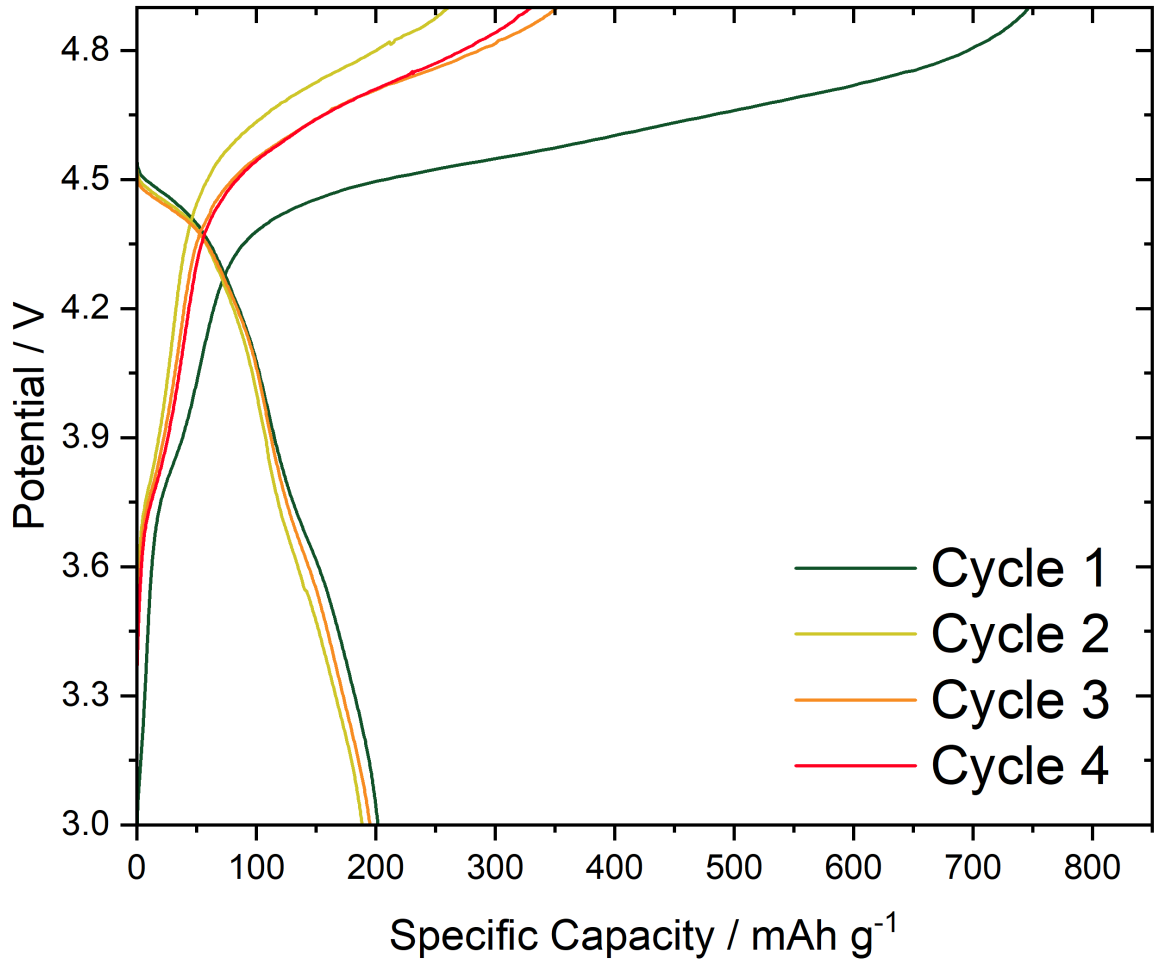

Figure 24. Cycling performance of LMNO from $Li_1Mn_{1.5}Ni_{0.5}O_4$ sputter target. Films annealed at 700˚C for 2h in O2.

exhibits anion redox activity. This capacity retention is important as it indicates the structure is becoming more stable.

Together these two data sets demonstrated that Li stoichiometric sputter targets promote the formation of layered $LiNi_{1/3}Mn_{2/3}O_2$ type materials and the extended annealing aids in driving off Li from the cathode and the formation of a small amount of higher voltage phases (likely spinel). With this in mind the following experiments were performed with Li deficient targets ($Li_{0.75}Mn_{1.5}Ni_{0.5}O_4$).

Figure 24 shows Li:LMNO cycling data for LMNO deposited from $Li_{0.75}Mn_{1.5}Ni_{0.5}O_4$ target material. The LMNO was annealed in O_2 for 1h at 700ºC and had a theoretical thickness of 8 mm. Several things are noticed from this data. First, the plateau at 3.75V is gone indicating we don't have Mn^{3+} in the cathode. Second, upon charging one sees a clear voltage plateau at 4.75 V consistent with Ni^{4+} redox activity. However, the capacity of this electrode is physically not realistic (>10,000 mAh/cm^2). This likely indicates that the cathode is undergoing a side reaction or there is redox activity with cathode current collector and the LiPON.

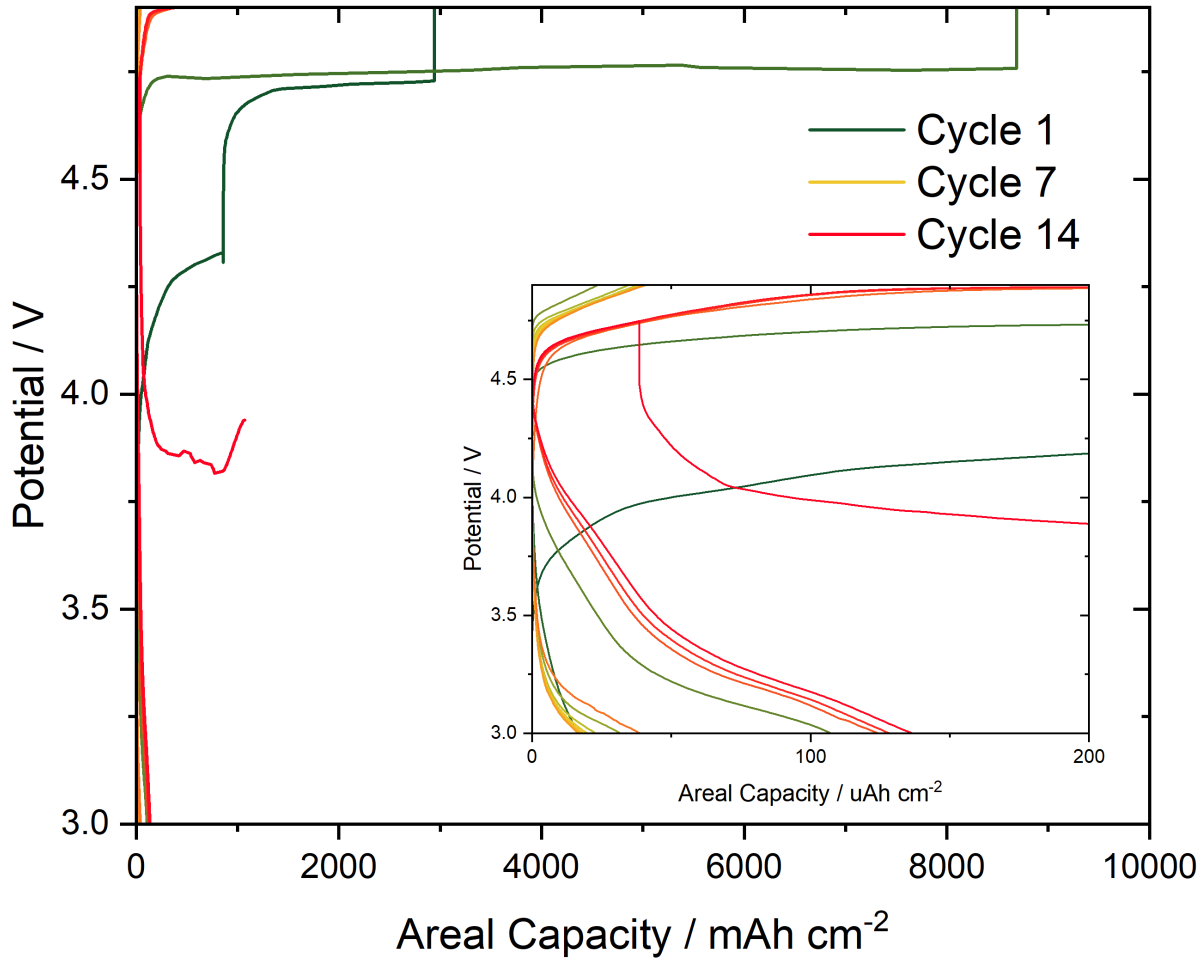

Figure 25. Cycling performance of LMNO from $Li_{0.75}Mn_{1.5}Ni_{0.5}O_4$ sputter target. Films annealed at 700˚C for 1h in O2.

Figure 25 shows Li:LMNO cycling data for LMNO deposited from $Li_{0.75}Mn_{1.5}Ni_{0.5}O_4$ target material. The LMNO was annealed in O_2 for 2h at 700°C and had a theoretical thickness of 8 mm. This data is the most exciting electrochemically. First, like the previous sample there was no voltage plateau at 3.75V indicating all the Mn was Mn^{4+}. Second, cycles 2-100 show the characteristic voltage plateaus for the spinel $LiMn_{1.5}Ni_{0.5}O_4$ at 4.65 and 4.75 V. However, on the first charge profile the OCV was 1.8V and the electrode had a large plateau at 4.3 V. This indicates that there is a large excess of Li in the cathode (hence the low OCV) and the material likely contains a mixture of the spinel $LiMn_{1.5}Ni_{0.5}O_4$ and the layered $LiNi_{1/3}Mn_{2/3}O_2$-type cathodes. These layered cathodes give the large voltage plateau and capacity in the green data but this seems to be a single redox active reaction that is not reversible as evidenced in the previous data. Interestingly, the $Ni^{2+} \rightarrow Ni^{3+} \rightarrow Ni^{4+}$ redox is highly reversible and stable with time and cycle (very promising). However, the charge capacity is nearly 2x larger than the discharge capacity, Figure 26. This indicates an irreversible side reaction is occurring with charging. Second, the specific capacity upon charging is nearly 3X larger than the theoretical value for stoichiometric LMNO. However, discharge is capacity is nearly 30% larger than theoretical. This indicates that the

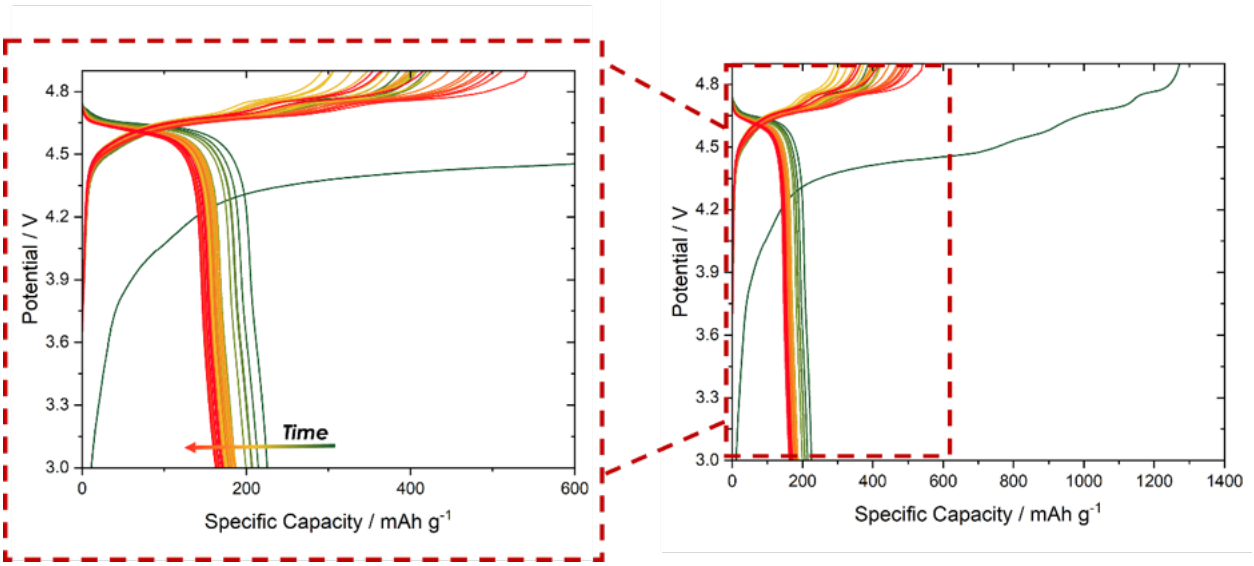

Figure 26. Cycling performance of LMNO from $Li_{0.75}Mn_{1.5}Ni_{0.5}O_4$ sputter target. Films annealed at 700˚C for 2h in O2.

thickness of the cathode is nearly 30% larger than theoretically predicted (~10.4 mm). This thicker electrode likely leads to spalling and flaking as observed for the films from the Li_1MNO targets and could be contributing to the irreversible capacity and side reactions from reactions with the Pt or Co/Pt in the current collector. Despite this limitation the data shows significant Li transport through the film indicating high-rate performance capabilities. Further refinements in the film growth conditions are likely to push the performance to higher values.

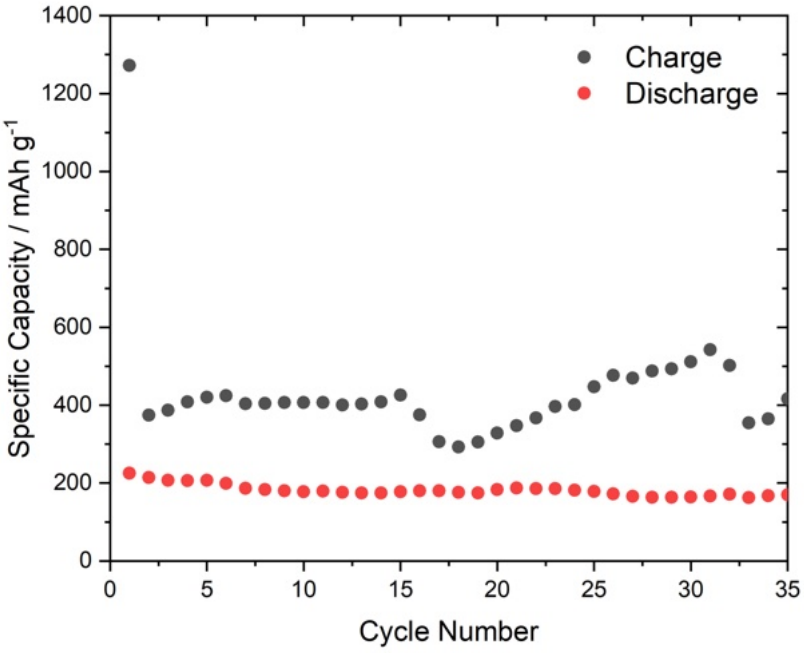

Figure 27. Capacity retention of LMNO from $Li_{0.75}Mn_{1.5}Ni_{0.5}O_4$ sputter target. Films annealed at 700˚C for 2h in O2.

3.5 Discussion

The results indicate that we can grow thick films of LMNO cathodes but there are critical challenges regarding adhesion, lithium content, and phase stability. Particularly, the deposition process is incorporating extreme excesses of Li during the deposition promoting the formation of layered lithium transition metal oxides. The precursor selection and synthesis process clearly affect the mechanics of the resulting sputter targets. However,

combustion synthesis appears to be a successful approach to make materials suitable for target densification and mechanical stability. Attempts to complete elemental analysis through inductively coupled plasma spectroscopy were put on hold due to resources but should be performed when time is available to quantify the composition and provide an estimate of the film thicknesses to compliment the quartz crystal microbalance measurements. Despite the chemical composition concerns the cells with LMNO cycled well as indicated by the clear, and maintained, voltage plateaus at 4.65 and 4.75V.

3.6 Conclusions

Synthesis of LMNO-Li cells using solid-state LiPON electrolyte was demonstrated, with the highest thickness of deposited LMNO cathode materials to date. These cells fabricated through combustion synthesis, a manufacturable method for LMNO fabrication demonstrated capacity retention and stability when used with LiPON and lithium anodes. This fabrication method for solid-state batteries using LiPON and LMNO cathodes demonstrates a good path forward for this critical technology.

Due to the changes in the overall design over Phase II, the radiation hard battery component of the study was deemphasized to focus on mission designs and planning. To this end, radiation testing was not completed in Phase II for the LMNO-Li cells, nor was isotopically enriched Li utilized. With the battery now being part of the spacecraft within the vehicle chassis, the battery will still experience direct heating from APPLE without the need for a flat, conformal design around the radiator. All of the vehicle internal components can be heated, including the battery without placing the battery on the external radiator. It follows then, that the battery will also not be exterior to the vehicle, exposed to the radiation environment without shielding, and with the cladding studies in the radiation section, will not be exposed to significant ionizing radiation from the isotope source.

3.7 Next Steps In Phase III

In Phase III we will not continue radiation hard battery development for APPLE. While the benefits for a long duration radiation hard battery for space missions, particularly where the battery is small, thin, and/or lightweight can extend the battery life to meet the longer mission requirements and low masses for trips to the Oort cloud, Pluto, or the solar gravity focal point, near term deployment of APPLE to the moon or Mars will not require 20+ years of operation through a full solar cycle and the importance of matching APPLE to a radiation hard battery becomes a lower priority. In addition, as noted above, the battery in the Phase II final design are not expected to be exposed to significant radiation dose.

The radiation hard battery collaboration between the Aerospace Corporation and DOE's Oak Ridge National labs will continue and focus on batteries for high radiation environments such as nuclear accident response drones and instrumentation for DOE,

high-radiation operations for environments for DoD applications, and laboratory radiation testing and monitoring.

4. Thermal Design Simulations

4.1 Thermal Design Introduction

The APPLE power system concept is a small, modular design with an overall minimum mass, targeting <50g for Pu and <200g for Am. This enables the utilization of the APPLE system in the widest range of vehicle designs including very small missions, utilizing the surfaces of the vehicle such as the chassis, instruments, and other structures. The key constraining factor in the design of APPLE is the thermal dissipation to the environment, as the core energy generation technology is thermoelectric materials (TEM) which convert heat to electrical energy and must dissipate heat from the thermoelectric junctions through a combination of radiators to space and conductive heat transfer to the rest of the vehicle. A decaying radioisotope provides the heat source for the TEM, and the radiation hard battery in the initial design acted as a radiation shield to other components. Figure 28 shows the final APPLE design concepts evolved from Phase II thermal design. This design can have a radiation hard battery at/as the radiator of the device, allowing the heat generated and dissipated from the isotope decay to keep the battery warm, though as noted above, it is not critical to have the battery at this interface. With the target temperatures for the radiators being ~20˚C, this means the battery would not need additional heating to function at this temperature, removing the mass of a heater and power overhead for temperature regulation.

This design can use the battery exterior as a radiator to keep the battery at operating temperature or it can have the battery within the vehicle as the exterior of the vehicle serving as the radiator. The target temperature for the battery is based on current temperature ranges of solid-state electrolytes for batteries based on the ionic

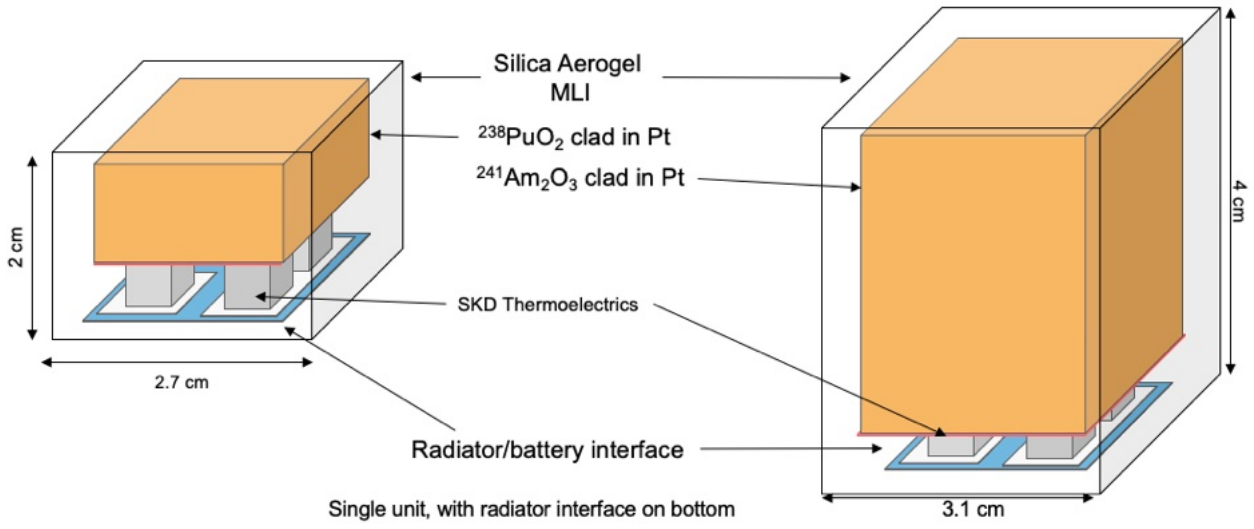

Figure 28. Two APPLE designs from the Phase II work. On the left is the PuO_2 design, using 31g of PuO_2 and on the right is the Am2O3 design, using 154g of Am_2O_3. Each unit produces 16.7W_{th} of thermal energy and is converted to 1.7 W_e of electric energy through the skutterudite thermoelectric legs. The thermal energy is dissipated through the radiator interface at the bottom of the unit to the vehicle chassis.

conductance of the materials. As discussed above in the Current Battery Capability section, these materials typically have a lower ion conductivity than the organic solvents plus lithium salts used in conventional Li-ion batteries. While extensive collective research efforts are underway to develop high power room temperature solid-state ceramic electrolytes, the nature of the APPLE application needs only relatively low power rates (C/5-C/3) much less than is needed for terrestrial applications such as electric vehicles, which often need 2-3C rates for charging and peak discharge rates of up to 5C. As noted these solid-state ceramics typically have acceptable ion conductance (while remaining electrically insulating) up to 60˚C. The ion conductance at these temperatures combined with having the radiator surface at a temperature that can be still used as a heat source for other vehicle components allows for the optimized performance from APPLE for both power generation and heating. In addition, with APPLE being located internal to the vehicle placed with the spacecraft systems, target temperatures can be designed around component temperature requirements.

The minimum component temperature was a significant constraint for the APPLE design, as geometry, thermoelectric conversion, and heat rejection need to be tailored to achieve a room temperature (10-30˚C) component temperature in close proximity to the isotope heat source. In addition to the Li-ion battery functioning optimally in the 10-30˚C temperature range, essentially all spacecraft components operate at these temperatures (with the exceptions of certain payload components that can be provided for separately). Choosing a target temperature in this range not only insures ease of vehicle and application design, but also reduces qualification efforts, as the maximum predicted thermal environments (MPE) can be kept close to room temperature and place limited thermal stress on the components.

The target temperature of 20˚C was also derived from the TEMs targeted in the design, skutterudites, chosen over the heritage materials of the MMRTG (PbSnTe-TAGS) and

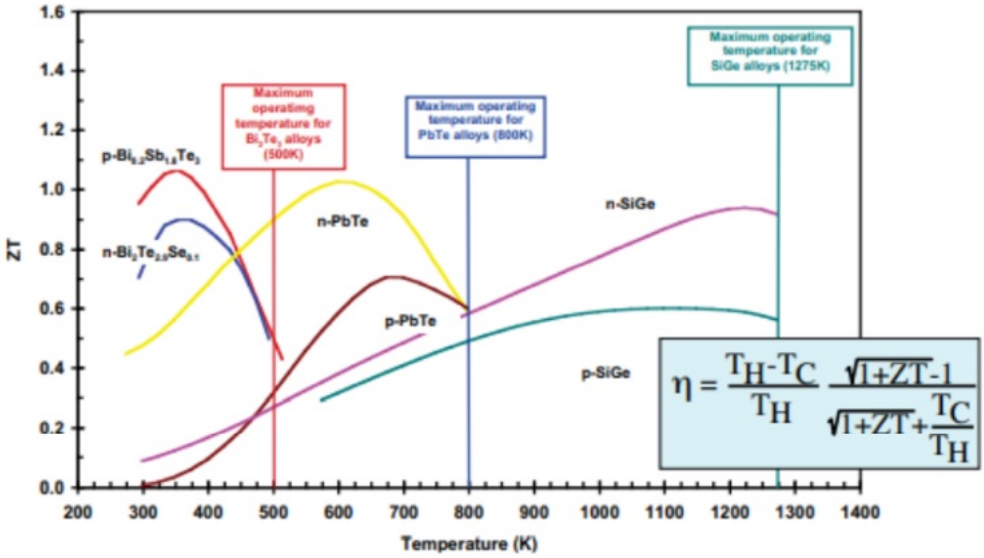

Figure 29. ZT values for heritage thermoelectric materials. The TEMs targeted in Phase I were the TAGS system, with optimal ZT values in the 600-700K range before moving to the SKDs in Phase II, from Calliat, et. al., 2013.

GPHS-RTG (Si-Ge) designs. These previously used materials have extensive heritage in NASA RTG mission, being used in the MMRTG and SNAP designs, and powering missions such as Mars Science Laboratory, Perseverance, Pioneers 10 and 11, and the Viking missions. It was decided to use the new SKD materials for thermoelectrics for APPLE due to their higher efficiency at lower temperatures. The maximum temperature limits for these materials are 800-850 K. Given the geometry of the APPLE device, the largest ΔT should be selected, as well as keeping the cold shoe/radiator temperature around 20˚C. The maximum operating temperature from this figure as well as the component constraints was then less than 60˚C, and the minimum temperature was set to greater than 0˚C for our thermal optimization process.

4.2 Isotope Properties

The isotopes investigated for this design were ^{238}Pu and ^{241}Am. $^{238}PuO_2$ was chosen as the primary plutonium oxide material due to its long history of NASA RTGs, the ongoing production of additional ^{238}Pu at DOE labs, and the absence of non-alpha ionizing radiation. In Phase II, ^{241}Am was also added as a design to take advantage of the potentially larger isotope supply from fission reactor waste as refinement ramps up in Europe. ^{241}Am is primarily an alpha emitter, though it does also have a low energy gamma emission. $^{238}PuO_2$ decays through alpha emission to generate heat at beginning of life (BOL) of 0.50 W/g and at end of life (EOL-15y) at 0.45 W/g for the IV oxide.[64] $^{241}Am_2O_3$ is the most commonly considered as alternative option to $^{238}PuO_2$ as the radioisotope material, but has a lower heat output per gram of 0.10 W/g for $^{241}Am_2O_3$ at BOL and EOL.[65] These thermal outputs were used for the thermal simulations for this study. This study considers the ^{238}Pu and ^{241}Am cases due to the radiation penetration and capture depths discussed in the Radiation Simulations section above despite their different thermal outputs. The general lessons of the thermal simulations apply to both isotopes in terms of thermal output if the isotope masses are scaled to an equal thermal output, ignoring any capture length or materials. For ^{241}Am, as discussed above, the Pt cladding may need to be increased compared to the ^{238}Pu design for radiation suppression, but from a mechanical standpoint, the cladding thickness will the same, at 1 mm, based on mechanical and fabrication requirements .

4.3 Thermoelectric Design Considerations

The electric performance of the APPLE design will depend on the TEM materials and design, with their constraints of conversion efficiency based on the equilibrium hot and cold shoe temperatures. Figure 30 is a thermoelectric device configuration with the hot and cold shoe locations, and heat transport from the heat source to the heat sink.[66] Copper was used as the hot shoe and cold shoe material for this design for its high thermal conductivity. TEM designs were based on a single material for the n- and p-type legs.

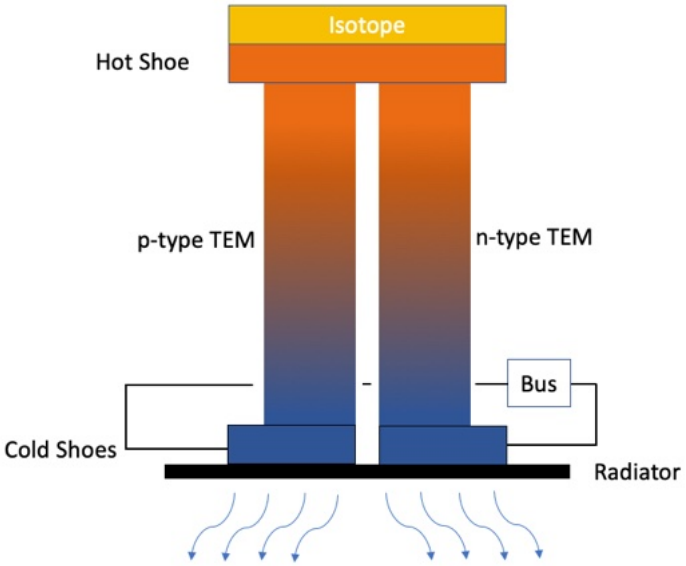

Figure 30. Thermoelectric junction scheme, showing the heat transport in the n- and p-type materials between the hot and cold shoes.

The efficiency of thermoelectric conversion depends on the equilibrium ΔT between the hot and cold shoes and the ZT of the thermoelectrics, scaled to the total heat passing across the thermoelectric junction. To this end, insulation is needed to surround the isotope heat source and the thermoelectrics to avoid thermal losses to the environment before passing fully through the thermoelectric junction, in addition to thermal insulation surrounding the isotope. Figure 30 shows the heat flow through the TEM between the hot and cold shoes through the n- and p-junctions.[67] Research on the best materials to compliment the TEM to minimize heat losses focused on aerogels and multi-layer insulation (MLI). The work presented uses aerogel as the insulation material due to its ease of application, as it can be cast around the thermoelectric components. The aerogel used had a thermal conductivity of 0.015 W/mK, and a density of 0.1 g/cm^3. The effective thermal conductivity for MLI (not used in this analysis, but likely for future designs) depends on the number of layers and the emissivity of the material. With a lower emissivity and by increasing number of layers, MLI designs can have lower thermal conductivity than the aerogel alone. MLI would help to minimize heat losses and mechanical assembly and function, but the design would be more complicated for the initial design concept analysis. A combination of both aerogel and MLI would likely be the optimum design to minimize heat losses and ease of fabrication.

The conversion efficiency of the TEM module is a function of both the thermoelectric materials and the equilibrium temperature delta across the hot and cold shoes. Equation 2 and
Equation 3 present the conversion efficiency equation. The efficiency (η) is derived directly from the properties and the temperature drop across the shoes. The Seebeck coefficient (S), the electrical resistivity (ρ), and the thermal conductivity (λ) are the properties of the TEM module that describe its performance.[68]

Equation 2

$$ZT = \frac{S^2 T}{\rho \lambda}$$

Equation 3

$$\eta_{max} = \frac{T_{hot} - T_{cold}}{T_{hot}} \frac{\sqrt{1+ZT}-1}{\sqrt{1+ZT}+\frac{T_{cold}}{T_{hot}}}$$

For smaller vehicles the chassis can serve as the radiator, resulting in a whole vehicle temperature range compatible with long term battery and component function (10-30˚C). One APPLE design has the battery at the radiator surface, resulting in thermal constraints on the radiator. This design allows the battery design to target the 10-30˚C temperature range, and allows for optimization of the ΔT of the thermoelectric conversion with a very low cold shoe target temperature but still keeps the battery temperature in a range where the electrolyte conductance is acceptable to mission discharge performance. With this design, the vehicle chassis can serve as the radiator, because the cold shoe temperature (the only thermal interface exposed to the interior of the vehicle), is at component compatible temperatures. This enables the entire vehicle exterior to serve as the radiator, bringing much more radiative area compared to heritage RTG systems. A large radiator will increase the ΔT for energy conversion and increase the TEM efficiency for a given ZT compared to these older systems.

Figure 31 shows a comparison between the TAGS and SiGe systems used in the MMRTG (TAGS) and the GPHS-RTG (SiGe) and APPLE. While the two heritage systems had very different ΔTs, the heat-to-electricity conversion efficiencies were similar, primarily due to the different ZT values of the thermoelectric materials used. The TAGS/PbTe based MMRTG had an efficiency of 7.0% based on a ΔT of 315K and similar radiator profiles. The large effective radiator of APPLE through using the chassis as enables highly efficient heat to electricity conversion when using the SKD

	n-PbTe	p-TAGS/ PbSnTe	n-SiGe	p-SiGe	n-SKD	p-SKD
Average ZT	0.90	0.84	0.69	0.41	1.05	0.65
Max T (K)	800	675/800	1275	1275	873	873
Efficiency	7.0% (800-485K)		7.5% (1275-575K)		10.9% (773-300K)	
Design	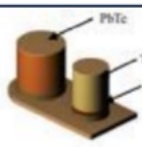 Conductively coupled		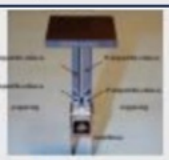 Radiatively coupled		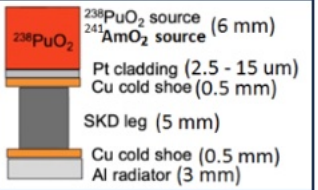	
Application					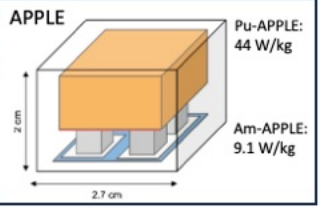	

Figure 31. TEM space heritage materials with efficiency and temperature application, comparing TAGS and SiGe systems to APPLE. Adapted from Calliat, et. al., 2013.

materials. The larger ΔT enabled through the APPLE chassis as-radiator-design allows for heat dispersion of the distributed APPLE units throughout the vehicle, and increases the ΔT by 50%, from 315K to 473K.

A key concern was allowing for sufficient distance for the heat transfer along the TEM. The thermal conductance (thermal conductivity*leg cross-sectional area)/(leg length) describes the heat flow from the hot shoe and cold shoe for their temperatures. The thermal conductance for the individual thermoelectric materials and the heat to be transferred dictated the required lengths of the TEM legs. This analysis used temperature dependent functions for the thermal and electrical conductivities for both the n-and p-legs. Phase II analysis included the temperature dependence and size variation between the n- and p-legs, with the legs segmented and calculated stepwise down each leg. The values for the leg cross-sectional area and the leg lengths were fixed for this analysis for the n- and p-type legs. The APPLE design uses a single isotope source in the device, insulated from its environment by an aerogel insulation layer except for its interface with the hot shoe and the TE thermal pathways. With the target chassis temperature of 20˚C, there can be some future optimization of the TEM leg length, area, and design, and thus the overall system size.

4.4 Thermal Simulations

Thermal simulations using the PATRAN SINDA/FLUINT[69] approach was used to evaluate the thermal design considerations for a single core APPLE unit containing ^{238}Pu and 241Am with Skutterudite thermoelectrics. Unlike the previous Phase I studies, this next iteration of the design embraces several changes in design for the thermal simulations.

The changes to the design focus on a single larger isotope core mated to thermoelectrics, encased in the insulating aerogel. These simulations, rather than focusing on a fixed, integral radiator as the previous thermal simulations, simulates radiator surfaces of variable sizes, as the radiative interface between the vehicle and the environment. This is not the area of a fixed radiator, but rather thermal design input to be passed up to the vehicle design. The PATRAN finite element model was used to perform a parametric analysis of the singular APPLE Core, focusing on hot and cold shoe equilibrium temperatures, thermal to electrical conversion efficiency, and the effects of total radiative area on the hot and cold shoe temperatures. The model simulates the PuO_2 Am_2O_3 and cores, the thermoelectric legs, and a variably sized radiative surface. SINDA/FLUINT was used for the parametric model and is based on finite difference mathematics using temperature dependent materials properties. The tool utilizes the temperature dependent thermal transport coefficients, heat capacities, interfacial transport dynamics for the thermoelectric, the insulating material, and the radiator. The Phase II APPLE design was simulated through a range of design inputs using the SINDA/FLUINT analysis across a range of sizes and geometries of the isotope core, as well as the radiator. The goal of this parametric design simulation was to determine the effects of isotope geometry, thermoelectric properties, radiator dimensions, and insulation properties on the heat to electricity conversion efficiency.

4.5 Skutterudite Thermoelectrics

A key update to this Phase II design is the replacement of the TAGS/PbSnTe thermoelectrics with more heat-to-electricity efficient skutterudite materials. The materials were for the p-SKD: $Ce_{0.9}Fe_{3.5}Co_{0.5}Sb_{12}$ and for the n-SKD: $Yb_{0.15}Ba_{0.05}Co_4Sb_{12}$, chosen for their low operating temperatures (hot shoe max between 500˚C (773K) and 600˚C (873K)) and high efficiencies. This lower temperature was selected as it will allow for the cold shoe temperatures to operate at component compatible temperatures (10-30˚C), reducing or eliminating the need for the APPLE unit to be isolated from other portions of the spacecraft, as well as removing the need for heat pipes to distribute heat to temperature sensitive components. Figure 32 and Figure 33 show the TE properties of the SKD materials to be used in this phase for the APPLE leg materials. The temperature range for these materials, both p and n-type show broad peaks in performance in the 600-800K range, leaving substantial design space for optimization of the devices. The ZT values for these materials, the ultimate measure of the efficiency of the heat to electricity conversion both peak around 773K, or 500˚C. This is now our target hot shoe temperature for optimal thermal design, much lower than the hot shoe temperatures proposed under the SiGe designs, which were over 1000˚C, and comparable with the hot shoe temperatures of the TAGS/PbSnTe materials. Key to utilization of the APPLE device integrated into a vehicle is lowering the cold shoe temperature such that the cold shoe is compatible with vehicle components, unlike the 200-300˚C temperatures for the heritage TE materials. This lower temperature can then have several benefits, not only allowing for APPLE devices to be placed closer key spacecraft components without damage or impact, but also allowing for easier emission of thermal energy to the environment, through the spacecraft itself, in effect turning the entire spacecraft into a radiator, and obviating the

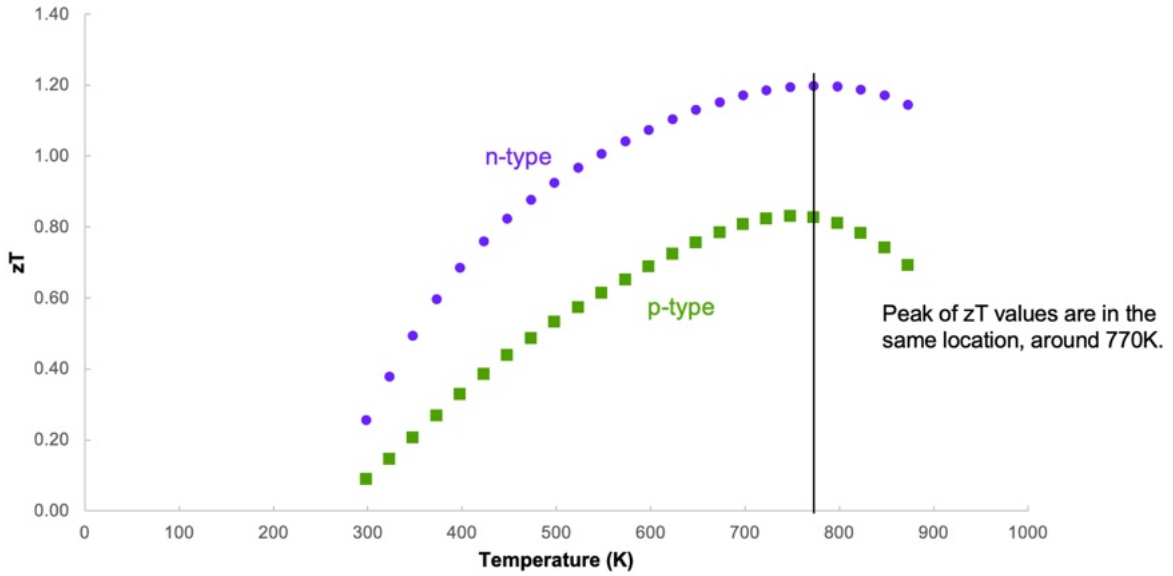

Figure 32. The thermal gradient down the TE legs means that the most efficient device would have a hot shoe hotter than the 770K temperature, to optimize the electrical conversion. However, higher sublimation rates limit this hot shoe temperature.

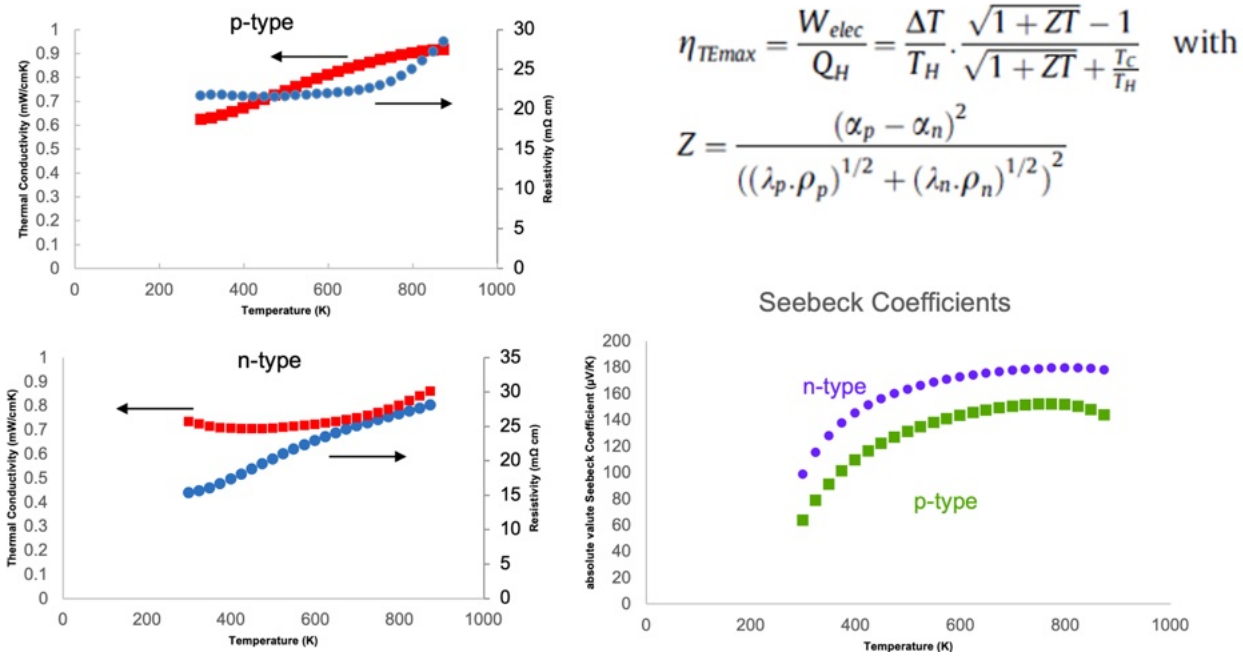

$$\eta_{TEmax} = \frac{W_{elec}}{Q_H} = \frac{\Delta T}{T_H} \cdot \frac{\sqrt{1+ZT}-1}{\sqrt{1+ZT}+\frac{T_C}{T_H}} \quad \text{with}$$

$$Z = \frac{(\alpha_p - \alpha_n)^2}{\left((\lambda_p \cdot \rho_p)^{1/2} + (\lambda_n \cdot \rho_n)^{1/2}\right)^2}$$

Figure 33. Resistivity starts increasing for p-type at 773K and Seebeck coefficient decreases after 773K, giving the most efficient conversion in this temperature area for p-type. n-type has a continual increase in resistivity, and has a flatter Seeback curve.

need for dedicated radiator surfaces, and particularly, materials and their masses and volumes. The spacecraft components and chassis can act as the APPLE radiator without the need to carry additional radiator mass or structures to keep the hot RTG away from the spacecraft and its instruments, and reducing the components needed to utilize the RTG heat to warm the spacecraft (i.e. no heat pipes, or heat transfer materials).

4.6 Thermal Limits to SKD Thermoelectrics

The primary anticipated limit for the lifetime of the SKD thermoelectric devices is degradation of the SKD material through sublimation of the TE material at the hot shoe junction. SKD material sublimating from the legs can impair the thermal and electrical connections to the hot shoe, increasing the electrical resistive losses and voltage drop, and reducing the rate of thermal transport. Testing of the sublimation rates of SKD materials (p-SKD: $Ce_{0.9}Fe_{3.5}Co_{0.5}Sb_{12}$, n-SKD: $Yb_{0.15}Ba_{0.05}Co_4Sb_{12}$) in vacuum with and without an aerogel encapsulation indicated that 17+ year lifetimes may be possible. Target sublimation rates are $5x10^{-5}$ g/cm^2/h of material for a given temperature to meet this 17+ year life. Figure 34 shows rates of sublimation measured for these materials in vacuum at 500 and 600˚C. Samples at 600˚C were also tested encapsulated in a silica aerogel to mitigate sublimation through containment of material. For the n-SKD a substantial reduction in sublimation was seen through encapsulation even at 600˚C, reducing the sublimation rate even below that of the bare n-SKD at 500˚C. Testing of the encapsulated materials was not performed at 500˚C due to timing issues. The p-SKD also showed reduction in sublimation rates over two orders of magnitude through encapsulation, though it had a more significant temperature based change in sublimation rates than the n-SKD, as sublimation rates decreased from 9.00E-2 at

600˚C to 1.70E-4 at 500˚C. As both materials showed appreciable reductions in sublimation through encapsulation in the silica aerogel, it is projected materials encapsulated in aerogel will meet or surpass the 5E-5 g/cm^2/h requirement though this will be to be verified. From this data the upper limit for the hot shoe of the SKDs was set at 500˚C for the thermal simulations. It should be noted that increasing this temperature will shorten the operational life of the thermoelectric device, but many applications considered for APPLE are far shorter than the 17 year target life, which was selected for maximum mission range, including deep space missions that take many years to reach their destination. For missions to the Moon or Mars, or other inner solar system missions, durations of 5 years or less will be sufficient. In addition, for Phase III, the SKD material will be switched to a SKD increasing the maximum temperature at the hot shoe and more efficient energy generation.

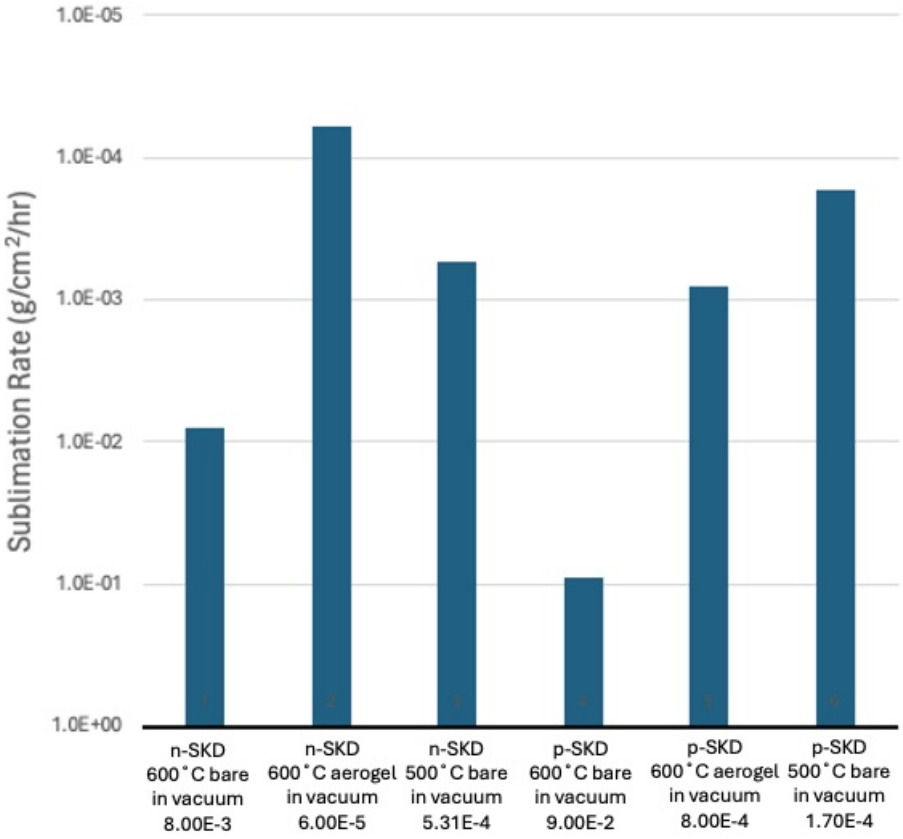

*Figure 34. Encapsulation is a potential path to reduce sublimation and extend device life. Target sublimation rates are 5E-5 g/cm^2*h. This enables devices to last 17+ years.*

4.7 Thermal Simulation Results

To perform a parametric scan for the APPLE design, thermal simulations were performed in PATRAN SINDA/FLUINT software using the thermal properties of the SKD TEs above, an insulator of aerogel MLI material (thermal conductivity: 0.015 W/m•K), and radiator properties of 3 mm thick Al (237 W/m•K). The SKD TE material properties were treated as temperature dependent functions, and the legs were segmented and each segment was piece-wise continuous, with the specific thermal and electrical conductivities used for each discrete volume element, resulting in a more accurate simulation of the TE legs of the APPLE device. The parameterization of the design was performed through varying the isotope xy dimension, isotope z dimension, and radiator xy size (radiator and hot shoe/isotope xy dimensions were assumed to be square) as shown in Figure 35. The TE legs were simulated as a fixed geometry and dimensions, with n and p-type legs being 4 x 4 mm in xy and 5 mm long (z). This fixed geometry for the legs was selected to match the TE junctions being fabricated in this study. The range of radiator sizes simulated was from the range of 5.0 cm x 5.0 up to 20.0 cm x 20.0 cm in 0.5 cm increments. Even though the final design does not include an integral radiator, the thermal simulations included an assumed radiator surface for calculation. This radiator is simulated as having one side facing space with the opposite side having the cold shoe interface with the remainder of that side backed by insulation. Final performance of the device will depend on the vehicle it is integrated into and the heat flows through its chassis and thermal design of the vehicle, as the thermal dissipation from the radiative surface will depend on the environment (i.e. lunar surface, Martian cave, deep space, planetary reflections, etc.) In translating to mission integration of the APPLE units into a vehicle, the thermal simulations can be used as an

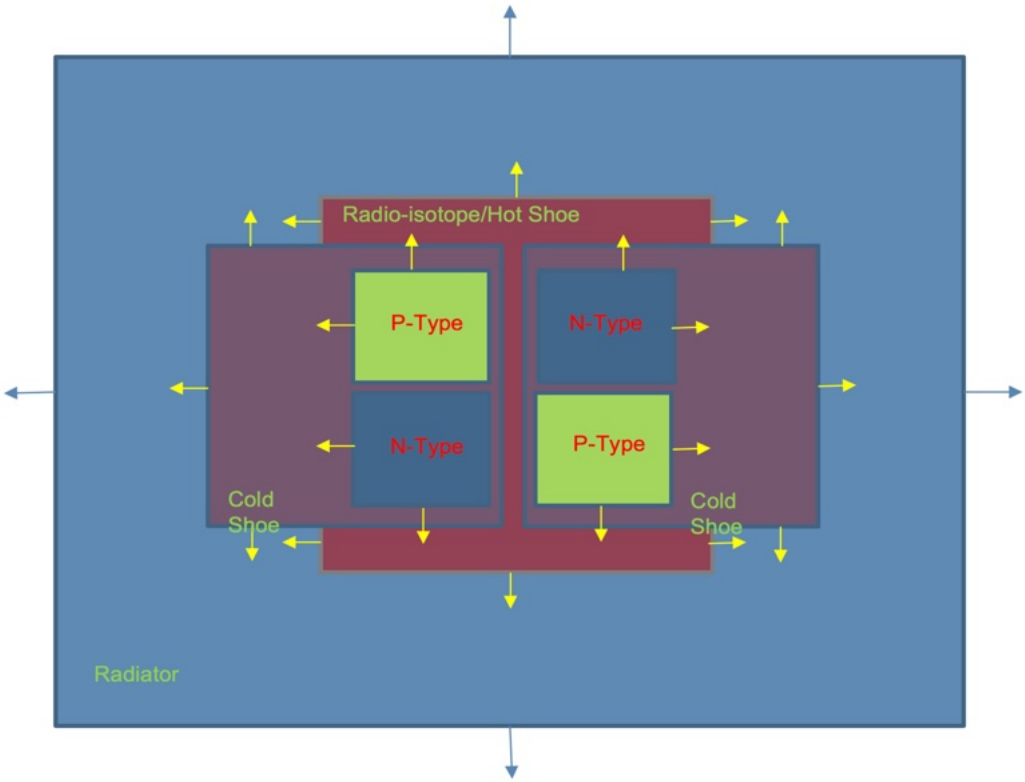

Figure 35. Radiator size scan: 5.0 cm x 5.0 cm to 20.0 cm x 20.0 cm incrementing by 0.5 cm. System was simulated with an integral radiator and aerogel encapsulation. Final design does not need a dedicated radiator, can use the chassis.

approximation of the required radiative surface per APPLE unit, but will require vehicle and mission specific thermal analysis. In general for planning purposes electrical output of an APPLE increases with more radiative surface/capability and decreases with less through changing the efficiency of energy generation through an increase in ΔT. Isotope dimensions were from 1.2 cm x 1.2 cm up to 2.2 cm x 2.2 cm, in 0.1 cm increments. The minimum isotope dimensions were chosen to space the TE legs in a 2x2 fashion with 2 mm between and a minimum of 1 mm to the hot shoe/isotope edge. The SKD leg dimensions and arrangement were fixed early in Phase II based on the dimensions of the most certainly deliverable hardware for testing. A wider range of device designs can be contemplated beyond those simulated here, including designs having more than four legs/two junctions, allowing for control of the series/parallel configuration and the current/voltage output of the device. The n- and p-type legs were simulated as having the same dimensions, though the p-type material is less efficient, and to match current throughput the p-type leg will be larger. The model utilized a high nodal count to ensure fine grained simulation results and to minimize edge interactions and errors. The APPLE design was matured by using the SINDA/FLUINT analysis to simulate the thermal/electric response with varying radioisotope decay heat (varying mass/volume of the isotope core).

Design boundary condition constraints were driven by the radioisotope decay heat under BOL and EOL conditions. The heat sink temperature for space was at 3 Kelvin. For simulations the tile was simulated as single sided, with one face (radiator) facing space and the other side considered to be a zero net heat transfer interface. Figure 36 shows a plot for parts of the parametric model output. Both the electrical output and the efficiency of conversion increased as the radiator size increased. The total electrical output strongly increased as the radiator (the device limiting parameter) increased, due to the increase in heat being generated/emitted, up to the TE maximum temperature for

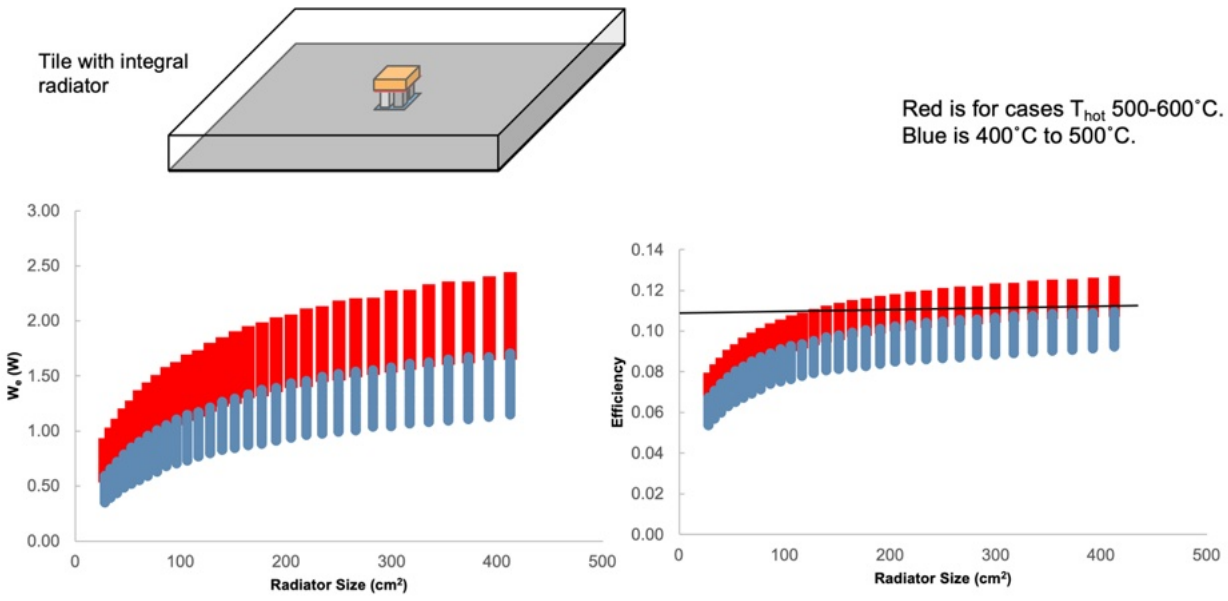

Figure 36. APPLE TE/isotope core was simulated with integral radiators. This radiator was modeled at 3 mm thick Al, a stand in for the vehicle chassis acting as a radiator. Efficiency starts to plateau at ~11% for T_{hot}=500˚C.

the SKD of 600˚C. This figure shows each vertical stack of points (both red and blue) as increasing volumes of Pu isotope, thus increasing the thermal input into the system. These stacks show both the outputs for cases where the maximum hot shoe temperature was 500˚C or below (blue), and for cases where the hot shoe was between 500˚C and 600 ˚C (red). The distinction in temperature regimes is due to the sensitivity of the SKD thermoelectrics to high temperature, showing increased sublimation at temperature over 500˚C. This sublimation could be life limiting, and to ensure a 17y mission life, the 500˚C maximum temperature was targeted for this study. For designs that encapsulate the SKD or otherwise takes steps to minimize sublimation, the 500˚C+ data can be instructive as to additional potential for the design as this would serve as a floor for device performance.

The beneficial effects on electrical conversion from the radiator as its size increases begins to plateau for the 300 cm^2 to 400+ cm^2 radiators, due to limits in thermal transport in the Al radiator. This limit stems from the capability of the radiator deliver heat out in a 2D plane if no other thermal transport components are considered. The balance of the in-plane thermal transport and radiation to space was the ultimate limitation of the device size and power output. Increasing the thermal inventory of the device for the radiator size quickly increased the hot and cold shoe temperatures as the radiator was unable to efficiently disperse the heat. Increasing the thermal inventory, and thus device size, show diminishing returns of electrical output, especially considering the imposed 500˚C hot shoe temperature. This restriction not only limits the efficiency and energy delivery capacity, but also the size extent and the spacing of multiple isotope units in the device, limiting them to ~every 20 cm for efficient thermal transport in the radiator surface in the absence of other thermal transport mechanisms. Utilization of components such as heat pipes, convective thermal transport (atmospheric missions), or conductive transport (beneficial environmental contact with a surface feature) can improve thermal dissipation and thus increase electrical output.

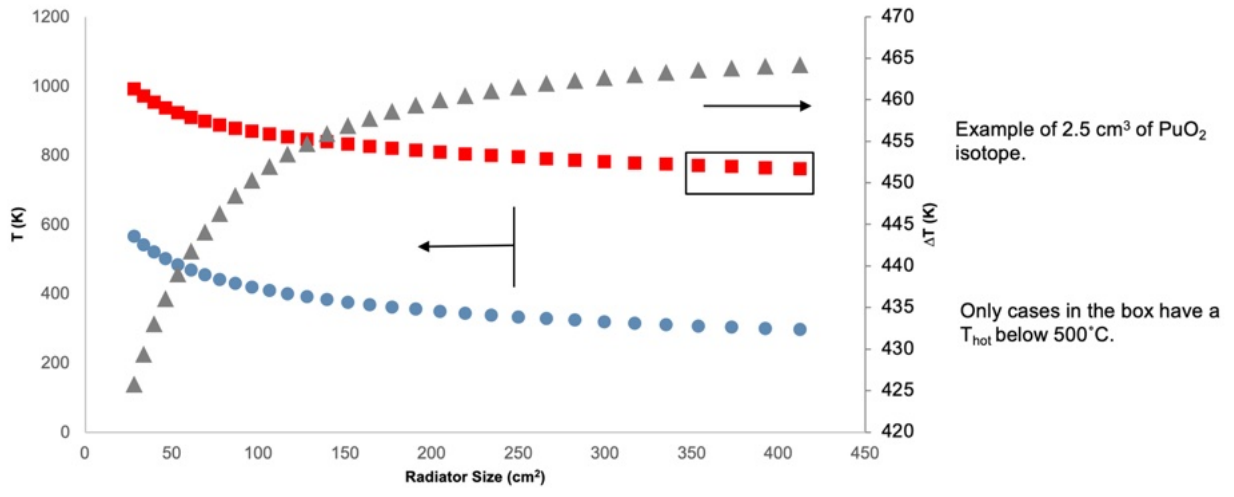

Figure 37. Increasing the radiator has a slightly larger effect on T_{cold} compared to T_{hot}, increasing ΔT for a fixed amount of isotope (thermal load). This can generally be said that increasing the radiator improves electrical conversion.

However, as Figure 37 shows, tailoring the size and extent of the radiator is necessary not only for electrical conversion, but also for keeping the TE legs at a temperature that suppresses sublimation to extend life. For a fixed isotope thermal load, increasing the radiator does lower the hot shoe temperature, as well as lowering the cold shoe temperature. By maintaining a T_{hot} below 500˚C the TE will operate longer, but also as the radiator grows, there is also a lowering of T_{cold}, the cold shoe temperature by a larger amount than T_{hot} is lowered, resulting in a larger ΔT, contributing to the increasing efficiency, though this is mitigated by the lower zT values in the legs towards the cold shoe as the temperature drops from hot shoe to cold shoe in the TE legs.

The result of this radiator and isotope size limitations is shown in Figure 38 where the power out in Watts actually peaks at a lower ΔT for a given isotope thermal input rather than at the maximum radiator size and ΔT value. Whereas for this case of 2.64 cm^3 of PuO_2 the maximum electrical output is calculated to be 1.65W for a 265 cm^2 radiative surface with a ΔT of 460K, as the radiator size is increased, the power output declines slightly to 1.63W at 420 cm^2 despite the higher 465K ΔT. However, it would be necessary to keep the design with the slightly lower electrical output and larger radiator to keep the hot shoe temperature below the 500˚C temperature for optimal unit life. The loss in output though from the larger radiator is very small, and the overall conclusions to be drawn is that power output is fairly flat over a large range of design parameters, allowing for variations in the radiator size, but more importantly, quality, as the APPLE device is moving to a chassis mounted position, and using the vehicle and its components as a radiator surface.

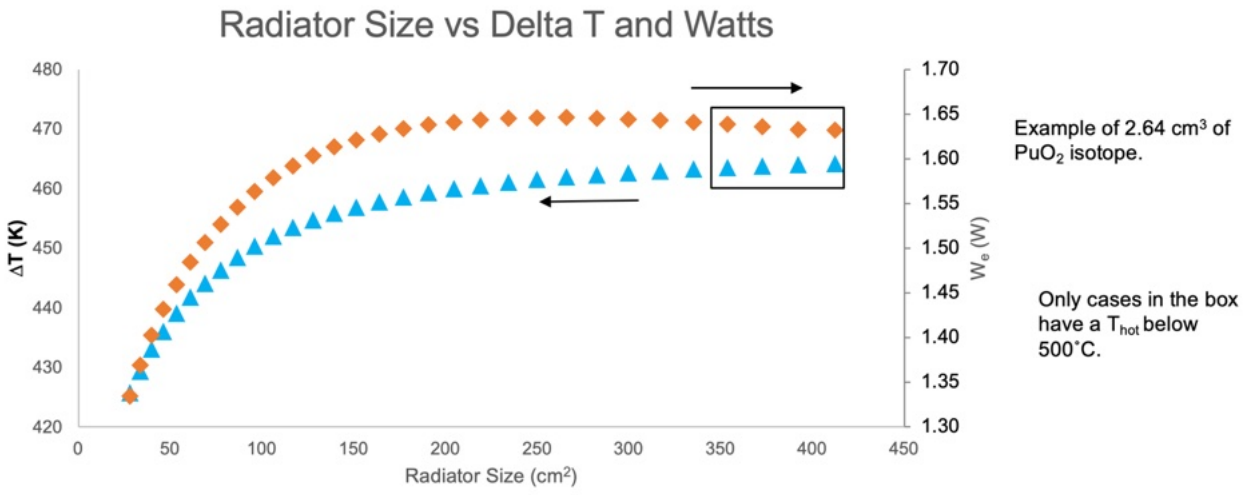

Figure 38. Conversion efficiency is fairly flat for a fixed amount of isotope above a certain radiator size. Extra radiator area increases ΔT, as the larger radiator lowers the T_{cold} more than T_{hot}, increasing ΔT. However, as temperature declines, this increase in ΔT is offset by lower thermal conductivity and Seebeck coefficient throughout the TE legs, lowering efficiency.

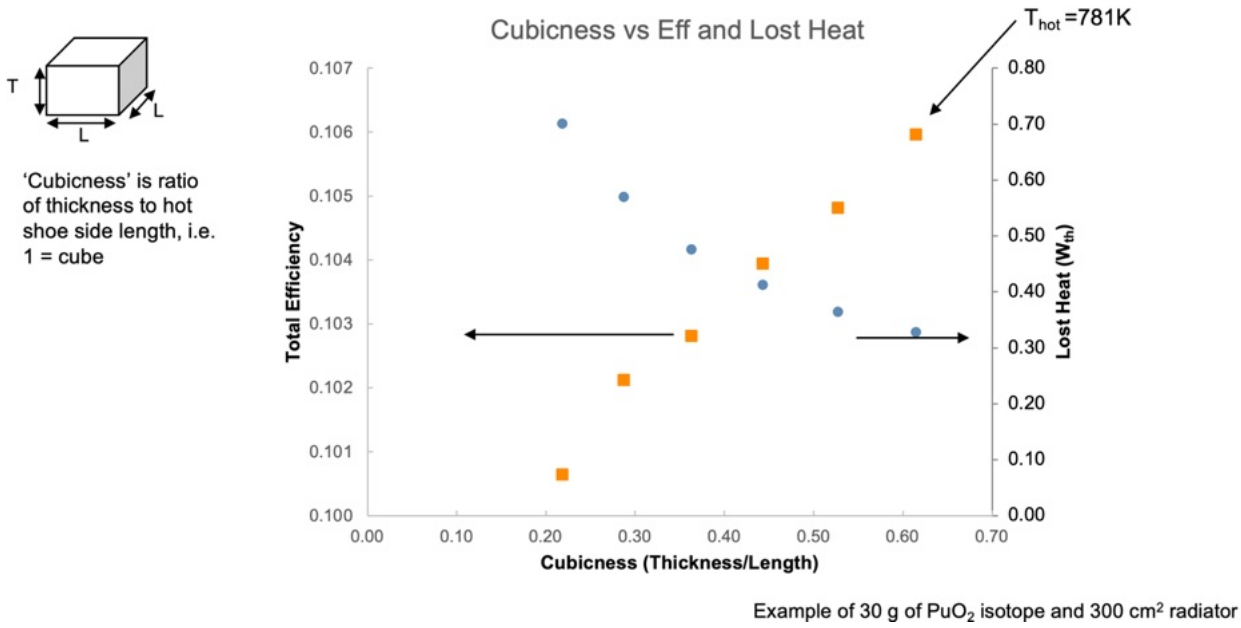

Figure 39. Efficiency increases for a given amount of isotope and radiator as the isotope is made more cubic. However, we cannot pursue this indefinitely, as it also drives the hot shoe temperature up as well. Hot shoe dia is limited by TE leg size and spacing. This results in a somewhat squat Pu source, rather than a surface area and waste heat minimizing shape given the fixed TE leg size and spacing.

The design study showed that the shape of the isotope has some effect on the efficiency, as the geometry of the isotope core was varied. Figure 39 shows 'lost heat' for a range of isotope rectilinear volumes, where this heat is lost to changes in the total surface area not at the hot shoe of the isotope. This heat is being insulated by the aerogel covering, but still has some losses. As the isotope becomes more cubic, i.e. each dimension x, y, and z are equal, less heat is lost from the lower surface area. This results in slightly higher efficiencies, but also higher hot shoe temperatures as less heat is lost to the insulation. For this particular study, there were no cubic isotope shapes that satisfied the simulation requirements. The xy parameters were fixed by the spacing of the TE legs, at a minimum of 1.2 x 1.2 cm, but an isotope thickness of 1.2 cm had a heat loading that was above the 600˚C absolute temperature limit for the thermoelectrics, much less the desired 500˚C hot shoe temperature for optimal unit life. This excess thermal input could also not be dispersed by the radiator as the radiator in plane thermal transport was insufficient as discussed above.

4.8 Americium-241 Thermal Simulations

The $^{241}Am_2O_3$ isotope source delivers 1/5 the thermal output of $^{238}PuO_2$ by mass, but has advantages in supply for RTG missions going forward, and a longer half life (432y vs 87.7y). This increase in half life has some small relative benefits to Pu-238, with the thermal output at EOL-17y being essentially unchanged compared to BOL (decreases by 2.7%), while Pu-238 decreases by 12.5%. To drive the same amount of heat into the TE legs as with a plutonium design, there needs to be ~5x the mass of Am_2O_3. In performing the thermal design for Am the simulations used the same SKD leg size and spacing for comparison to Pu design, as well as compatibility with the JPL fabricated

thermoelectrics. This allows for direct comparison to Pu design, but this may not be the optimal spacing for the larger Am design. The larger volume of Am_2O_3 with the same insulation results in somewhat higher thermal loss to the insulation, but overall the design performance is similar, if larger and heavier, as heat lost to non-TE pathways scales with surface area of isotope core. Since the thermal output is essentially the same, just from a larger, but still insulated isotope core, the radiator parameters don't change. Vehicle designs would not change much from a thermal standpoint, only a mass and volume consideration. This would allow for vehicle designs to be somewhat agnostic to APPLE type, Pu or Am, for cases where the RTG mass is not a significant fraction of the vehicle mass.

- The 1.7 W_e Am design, using 165 g Am_2O_3 and the same 2x2 TE leg design is more elongated.
  - *Same 500˚C limiting hot shoe temperature.*
- A larger 2.1 W_e Am design can also be considered, where hot shoe temperature limits are relaxed. A 186 g Am core for a 4x3.3 cm device would have a hot shoe temperature of 562 ˚C, similar to the 2.1 W_e Pu case.

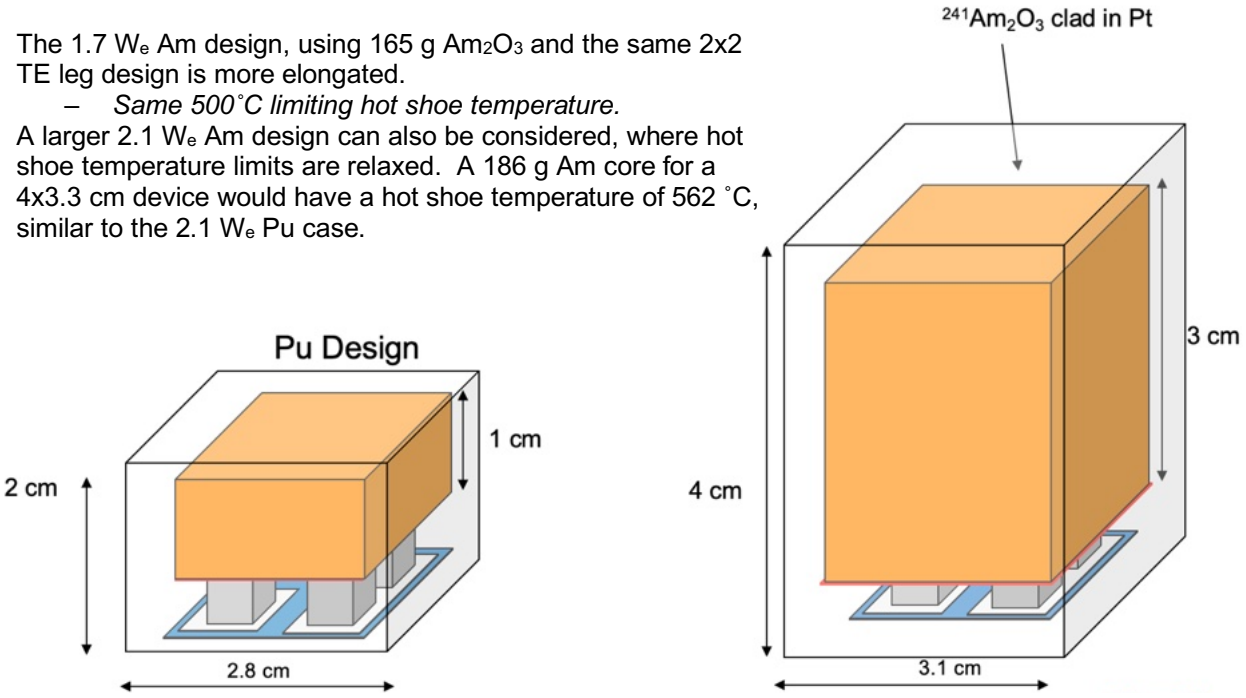

Figure 40. Comparing the Pu-238 design to the comparable Am-241 design, using the same 2x2, 2 junction thermoelectric design.

4.8.1 Am Thermal Parametric Simulations

The Am-241 thermal parametric simulations were performed similarly to the Pu-238 simulations above. The radiator area isotope volume/mass was varied to optimize the design. However, the thermoelectric junction remained the same as the Pu-238 design, with the 5 mm high, 4x4 mm area TE junction as for Pu-238 for congruence with the SKD TE junction being fabricated for testing. As shown in Figure 41, the primary consequence of varying the radiator area or capability was to raise both the hot and cold shoe temperatures fairly equally, resulting in a fairly flat ΔT, the primary impactor to the efficiency of TE conversion. This figure shows the results for 20.2 W_{th} of Am-241 (16.7 cm^3 of Am_2O_3) with T_{hot} below 500˚C.

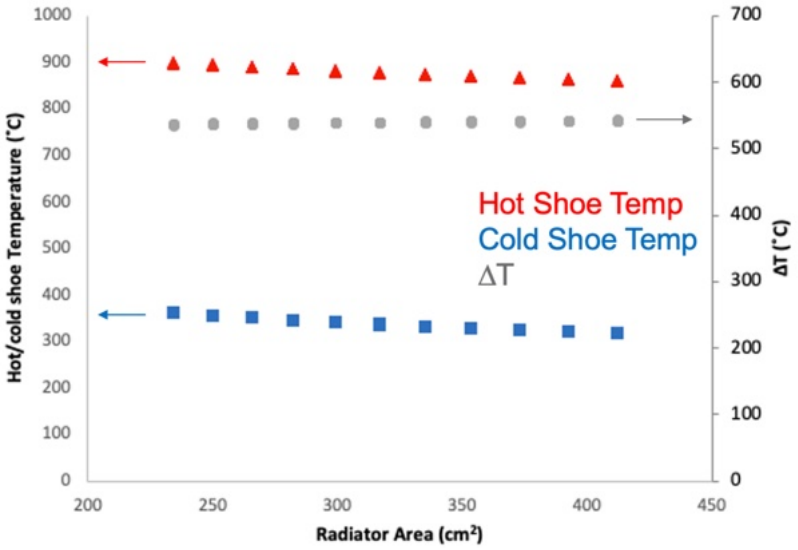

Figure 41. The trending of the radiator area vs. resulting hot and cold shoe temperatures and their ΔT. Similar to Pu-238, the Am-241 design had a relatively flat ΔT based on radiator area variance for 20.2 W_{th} of Am-241.

The effects of the more elongated form factor for the Am_2O_3 are very modest, as the most significant impact is expected to be slightly increased thermal loss through the insulation rather than through the thermoelectrics. However, as seen in Figure 42, the effect is essentially zero. The aerogel simulated in these calculations are sufficiently insulating that increasing the area for heat loss has very little effect on the efficiency of thermoconversion.

This is shown in Figure 41, where the aspect ratio is compared to the thermal loss. While there is a trend in thermal loss by varying the aspect ratio of the Am-241 core (<1 is squat, >1 is tall), the effect is relatively small, varying between 8.2 and 9.2%. The minimum is not located at the total surface area minimum, however, because as the core becomes more squat, the bottom (cold shoe) area expands beyond the TE junction, meaning more thermal transport must occur in the plane of the cold shoe to the TE junctions. By keeping the TE junction design fixed based on the fabrication plans, we have located more of the thermal surface away from the junction and increase the thermal transport path, leading to additional insulation and loss. This could be mitigated by redesigning the TE junction to reflect the larger surface area and interface of the Am-241 clad in a follow-on study.

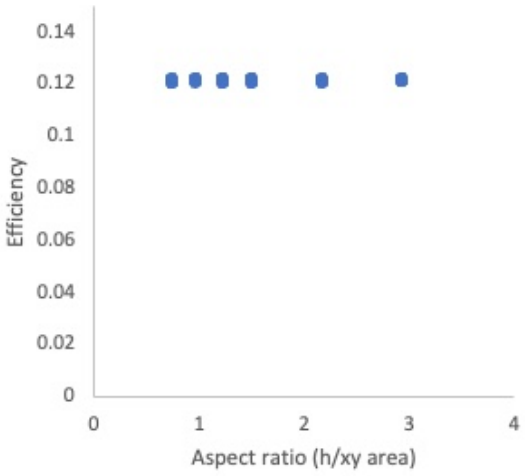

Figure 42. Efficiency of thermoconversion versus aspect ratio of the Am-241 source. The essentially flat conversion regardless of isotope height (isovolumetric) demonstrates the effectiveness of the insulation.

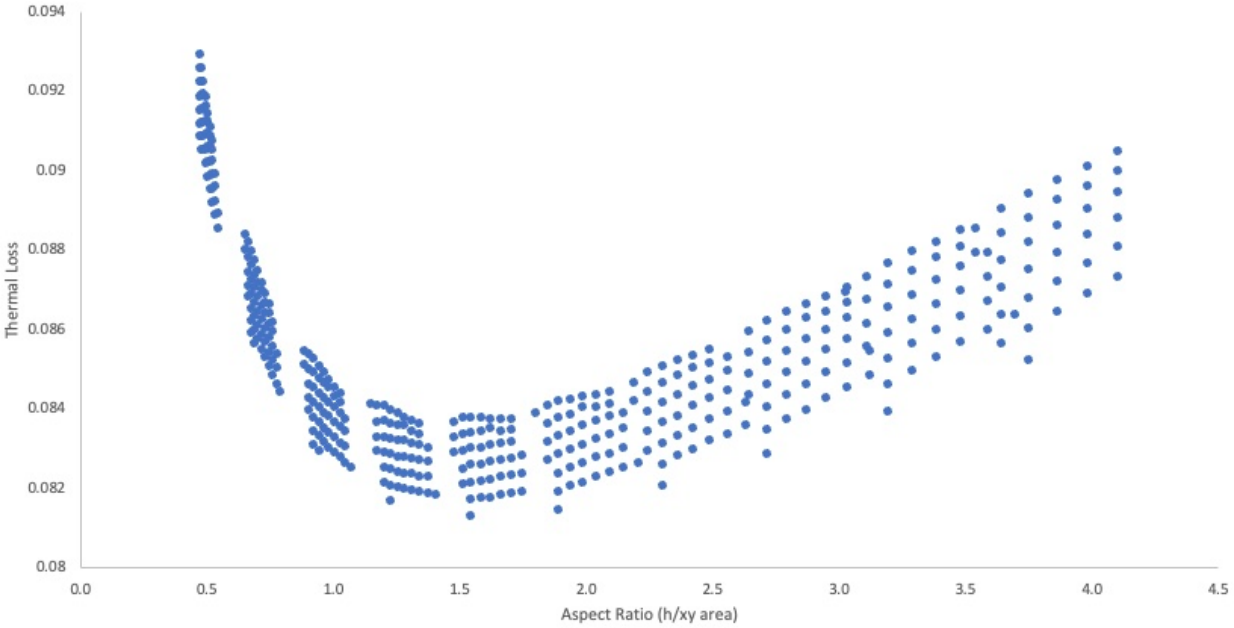

Figure 43. Heat loss through the insulation from elongation of the Am-241 clad. The minimum thermal loss is seen around 1.5, which is not the area minimum. This is caused by the invariant size and spacing of the TE junction.

4.9 Thermal Design Conclusions

The thermal design in Phase II drove the overall design of the APPLE device, and unlocked a new approach to placement of the unit in the vehicle and a new range of missions. The switch to the SKD materials, as well as relatively small amount of thermal inventory for the isotopes leads to what is a unique approach to RPS design, that sits between small RHU and large RTG technologies. By focusing on a compact APPLE design, we overlap with many of the RHU applications, and deliver heat for those missions, but also enable powered operations as well. In addition, our small size and efficient use of heat for power generation match the APPLE design well to the current isotope landscape, with powered missions possible with very small amounts (<50 g Pu-238, <200 g Am-241) of the hard to obtain isotopes. With demand for both Pu-238 by NASA's MMRTG (and potentially the GPHS-RTG revival program), and Europe's production of Am-241 primarily for their own missions, APPLE may be still enable missions with the excess or spare isotopes not used in the other RPS programs.

4.10 Next Steps in Phase III

The Phase II design with analysis shows that the APPLE concept can be used in many applications. These applications include satellites, planetary vehicles, stationary applications, localized heat and power spacecraft needs, etc. Essentially any application where sunlight is not an option for power, and where there is the capability to effectively dissipate heat to the environment (i.e. not Venus, sun side Mercury).

Phase III of this project will work with advanced skutterudite materials in JPL's Thermal Energy Conversion Materials Research Group for development and fabrication of more efficient TEM couples. In a new design, the target temperatures and design dimensions will likely be adjusted, but due to the higher efficiencies this next generation of device will exceed those simulated in Phase II.

5. Thermoelectric Fabrication and Characterization

5.1 Skutterudite Thermoelectric Background

As discussed above, efficient thermoelectric conversion is evaluated from the ZT value of the material. Zintl materials are a class of materials with high ZTs and have been a focus of thermoelectric development for years. Zintl materials are covalent intermetallics with significant ionic bonding. Zintl materials have an alkaline earth or rare earth and a transition metal with a metalloid. They are typically poor thermal conductors and semiconductors. The high ZTs in these materials are attributed to their glass-like thermal conductivities as a result of the structural complexity from their mixed bonding. The thermoelectric properties of Zintl materials can be tuned via doping to improve the ZT values. Zintl phases in skutterudites (SKD), which are in the family of $CoAs_3$ have been developed as high ZT value for RPS programs. In this work, we synthesize n- and p-type Zintl phases of SKDs in the $CoSb_3$ family through substitution of the Co transition metal sites with rare earths.[70]

The conversion efficiency of thermoelectric materials comes from the balance between the two key thermoelectric properties, the Seebeck coefficient and electrical conductivity. Good thermoelectric materials are typically semiconductors and the free carrier concentration may be tuned through doping the material as in other semiconductor materials. Doping either adds additional electrons or holes to the material through substitution of elements from one higher (electron, n-type) or lower (hole, p-type) column on the periodic table, or by introducing additional atoms in crystal lattice vacancies. The SKD materials of the n- and p-type skutterudites developed at JPL were designed to maximize their ZT values for the MMRTG thermal profile (200˚C to 600°C). The SKD formulations selected for APPLE are n-SKD: $Yb_{0.15}Ba_{0.05}Co_4Sb_{12}$; p-SKD: $Ce_{0.9}Fe_{3.5}Co_{0.5}Sb_{12}$. However, efficient operation can be accomplished in the lower temperature range of the Phase II APPLE design, which targets a much lower cold shoe temperature to enable component compatibility as shown in the thermal design section above. The larger ΔT enables us to use this material without undergoing a lengthy and expensive reoptimizing of the composition and still deliver higher efficiencies than the eMMRTG baseline conversion (9%).[71]

JPL has been developing SKD materials and performed tech transfer to the eMMRTG program, with a goal of increasing the power output of the MMRTG design by 50% EOL only replacing the TE modules, preserving the MMRTG heritage for other components.[72] The work herein leverages this work for development and synthesis of the APPLE SKD materials and module fabrication.

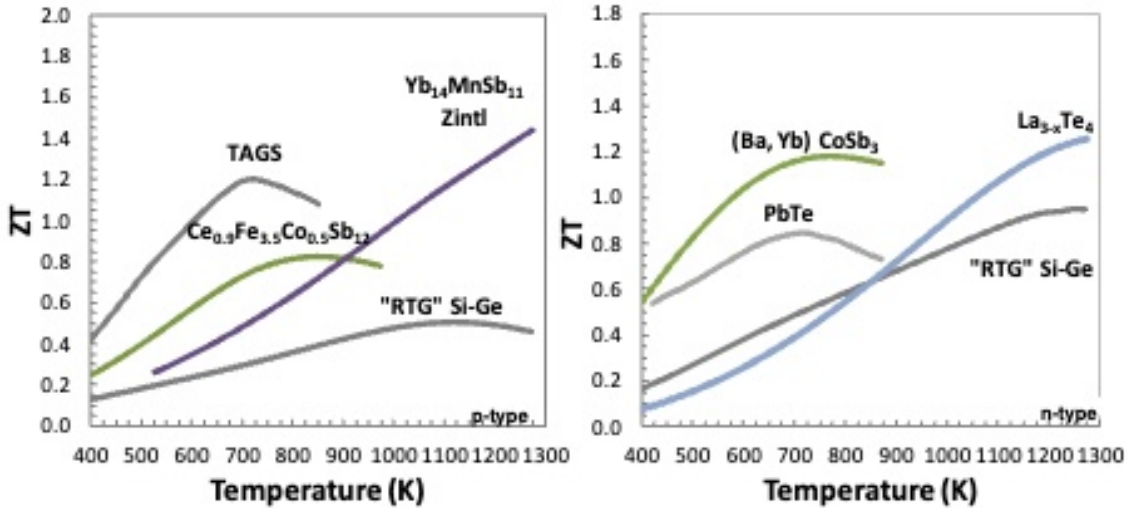

Figure 44. ZT vs T for p-type and n-type thermoelectric materials developed at JPL and collaborators. The SKD materials (green), especially for the n-type leg substantially improves the ZT values and energy conversion for the materials.[96]

5.2 Skutterudite Thermoelectric Bi-couple Design

The design of the skutterudite (SKD) thermoelectric bi-couple was based upon the thermal stimulation work presented in the previous chapter. The finalized schematic of the skutterudite thermoelectric bi-couple is shown in Figure 45. The bi-couple consists of two skutterudite couples (a bi-couple) that are connected electrically in series through the conductive hot and cold shoe interface materials. The p-type ($Ce_{0.9}Fe_{3.5}Co_{0.5}Sb_{12}$) and n-type ($Yb_{0.15}Ba_{0.05}Co_4Sb_{12}$) skutterudite materials were baselined for the NIAC phase II as they possess a higher conversion efficiency than state-of-practice TAGS/PbSnTe or Bi_2Te_3 thermoelectric materials in the relevant temperature range (500˚C to 20˚C). A maximum power output of 2.0W was predicted for the skutterudite thermoelectric bi-couple with a hot-side temperature at 550°C (773K) and a cold-side temperature at ~50°C (333K). The bi-couple fabrication process consists of: 1) synthesis of thermoelectric materials (p-type and n-type) and high-temperature thermoelectric properties measurements and qualification, 2) co-hot pressing metallization to produce metallized pucks for thermoelectric leg fabrication, and quality

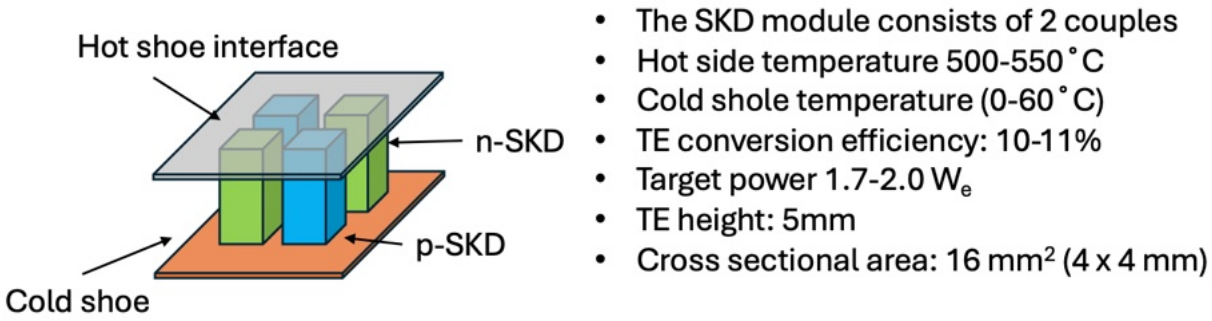

Figure 45. TE unit design and targets for fabrication.

assurance, 3) the use of a pre-fabricated hot-side interconnect, 4) bi-couple assembly and bonding, and 5) aerogel encapsulation.

5.3 Thermoelectric materials synthesis and characterization

The first step in the fabrication of the skutterudite bi-couple was the synthesis of the TE materials. The p-type and n-type thermoelectric materials were synthesized via a process previously developed for the eMMRTG/skutterudite technology maturation project[70] using a combination of ball milling and annealing to produce 100g (nominal) batches. For the NIAC phase II project, two batches of p-type and n-type were made, with the second batch being considered as a back-up, if required. The powders were stored inside a glovebox to prevent oxidation and ensure longer shelf life.

Figure 46. Ball milling was performed to make the SKD precursor materials.

Once the synthesis was completed, the materials were then sintered for high temperature TE properties characterization and qualification. Figure 47 shows the QA samples for room temperature and high temperature TE properties measurement for p-type and n-type skutterudite materials. Typical qualification samples are hot-pressed into a 12.7 mm diameter, 3 to 4 mm thick coupons. Each coupon was then cut and polished to obtain a ~1mm thick samples for measurements. The room temperature properties density, four point probe resistivity, and Seebeck coefficient are shown in Table 2, Table 3, and Table 4, respectively. These properties all met the previously established acceptance values for both the p-type and n-type SKD TE materials with the exception of the n-type skutterudite batch #2 which had higher resistivity than the acceptance range. This is likely due to under-doping. This batch was not used for the production of the couple.

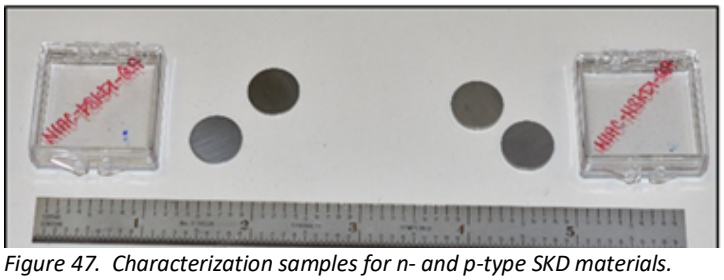

Figure 47. Characterization samples for n- and p-type SKD materials. Samples were 12.7 mm dia. and 3-4 mm thick.

Table 2. Room Temperature Density Measurement of p-type and n-type skutterudite materials.

Materials	Density (g/cm^3)	% of Theoretical Density
p-type Skutterudite Batch #1	7.83	99.68
p-type Skutterudite Batch #2	7.79	99.20
n-type Skutterudite Batch #1	7.56	99.12
n-type Skutterudite Batch #2	7.55	98.97

Table 3. Room Temperature Resistivity Measurement of p-type and n-type skutterudite materials.

Materials	RT Resistivity (mΩ·cm)	Acceptance Range (mΩ·cm)
p-type Skutterudite Batch #1	0.59	0.57-0.67
p-type Skutterudite Batch #1	0.62	0.57-0.67
n-type Skutterudite Batch #2	0.53	0.40-0.60
n-type Skutterudite Batch #2	0.65	0.40-0.60

Table 4. Room Temperature Resistivity Measurement of p-type and n-type skutterudite materials.

Materials	RT Seebeck (μV/K)	Acceptance Range (μV/K)
p-type Skutterudite Batch #1	80.11	78-86
p-type Skutterudite Batch #1	80.57	78-86
n-type Skutterudite Batch #2	-120.19	-110 to -125
n-type Skutterudite Batch #2	-120.39	-110 to -125

To ensure the high temperature thermoelectric properties are within the established values, the high temperature resistivity, Seebeck coefficient, and thermal conductivity was measured for each batch of materials. Figure 48 and Figure 49 show the measured high-temperature resistivity, Seebeck coefficient, and thermal conductivity values for n- and p-type skutterudite thermoelectric materials. The data was compared to JPL's internal n-type skutterudite reference data. All the properties were within the qualification range except for the resistivity of the second batch of n-type SKD, which may have been slightly under doped. The second batch was not used in the production of the bi-couples.

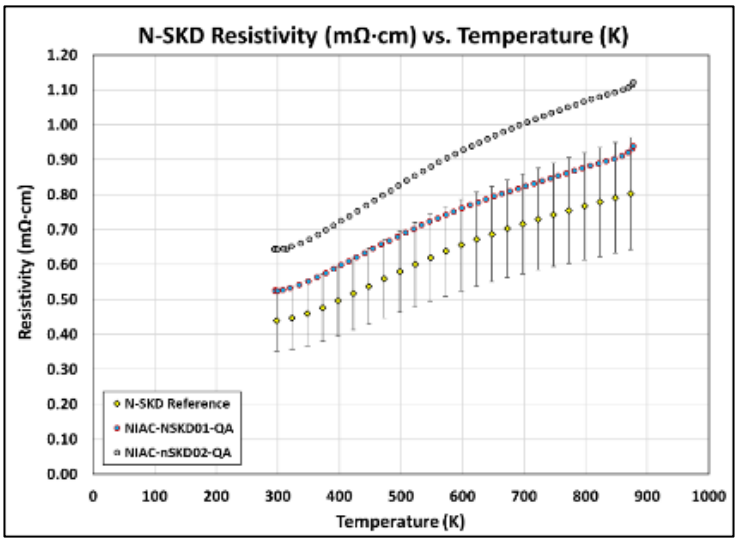

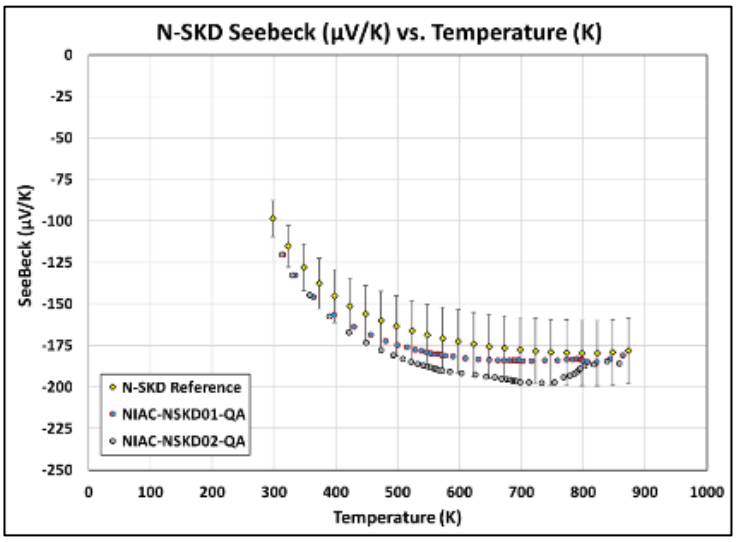

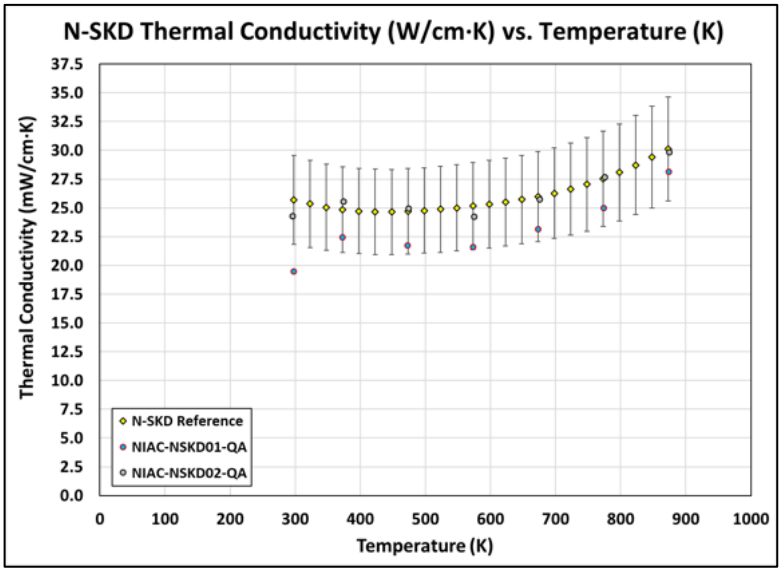

Figure 48. High temperature resistivity, Seebeck coefficient and thermal conductivity for n-type skutterudite TE materials.

Figure 49 shows the high temperature resistivity, Seebeck coefficient, and thermal conductivity for p-type skutterudite thermoelectric batches. The data was compared to internal JPL's internal p-type skutterudite reference data. All the properties were within acceptance range. Batch #1 powder was used for the final fabrication of the SKD bi-couple.

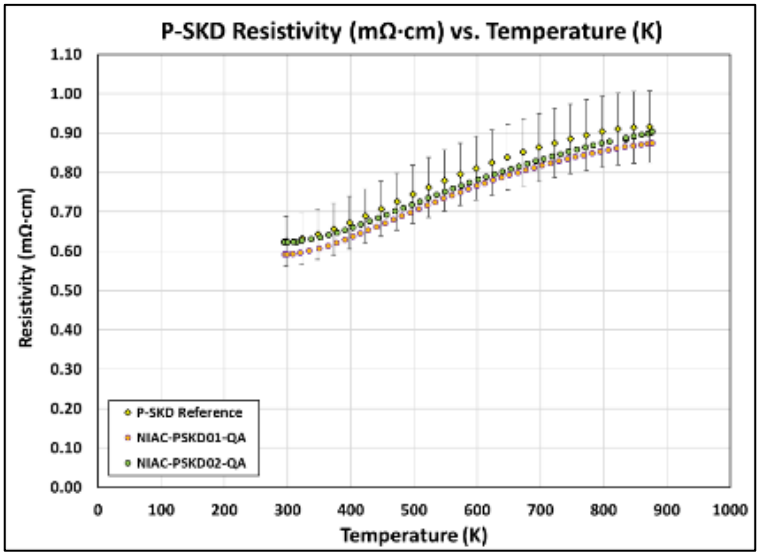

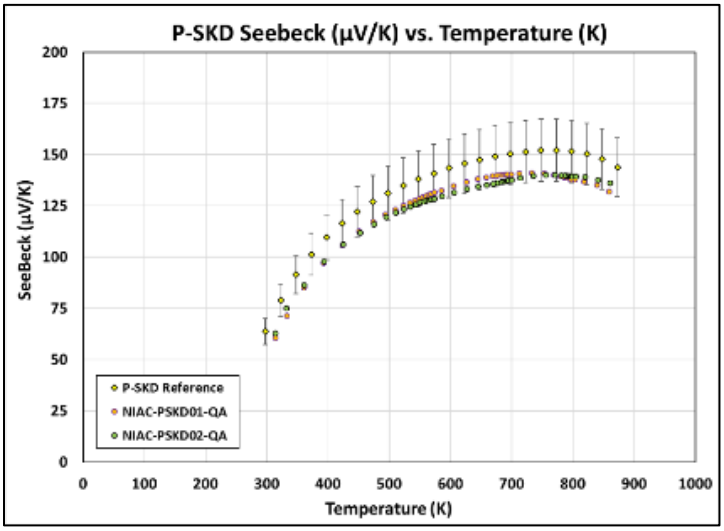

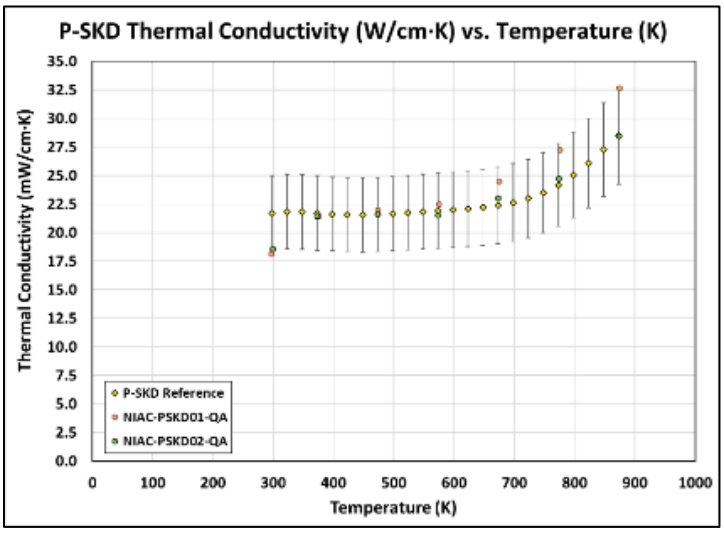

Figure 49. High temperature resistivity, Seebeck and thermal conductivity for p-type skutterudite TE materials.

5.4 Thermoelectric Leg Fabrication

Upon verification of the TE materials properties, the next step in the fabrication process was to sinter skutterudite powders into metallized pucks. JPL has previously developed a co-hot press metallization technique where the skutterudite powders are sintered and simultaneously metallized in a single step process. Figure 50 shows the process flow for the co-hot pressing metallization process. The graphite dies were cleaned and coated with a thin layer of release layer to prevent the metallized pucks from adhering to the graphite dies after sintering. Next, metallic foils were machined to 31.75 mm diameter supports. In Figure 50, two different metal foils were used (one metal is the capping layer and the other is an adhesion layer). The metal foils were chemically

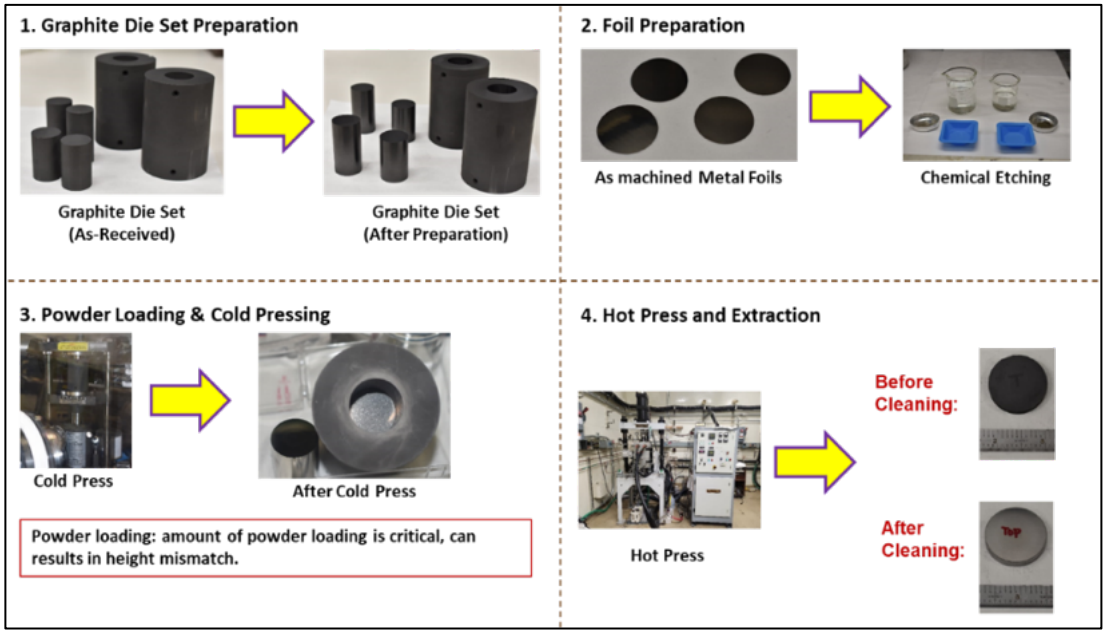

Figure 50. Process flow of co-hot press metallization of thermoelectric materials.

etched to ensure the removal of any oxide on the surface of the metal prior to loading into the graphite die. The skutterudite materials were then loaded in the graphite die. Powders were initially cold-pressed, then the metal layers (top and bottom side) were loaded with the graphite plunger and spacer. The powder weight was calculated based on the density values that were measured for the qualification coupons to achieve the target height of 5 mm. The loaded graphite die assembly were loaded into a uniaxial hot-press and processed using the same sintering temperature and pressure profile as the qualification pucks.

Overall, three (3) p-type and three (3) n-type skutterudite metallized pucks were fabricated, as shown in Figure 51. There were no cracks or delamination observed in p-type and n-type skutterudite metallized pucks after hot-pressing. The metallized pucks then cleaned via a polishing process prior to dicing so that the p-type and n-type metallization pucks were of the same height (5mm ±25μm). A flatness and parallelism

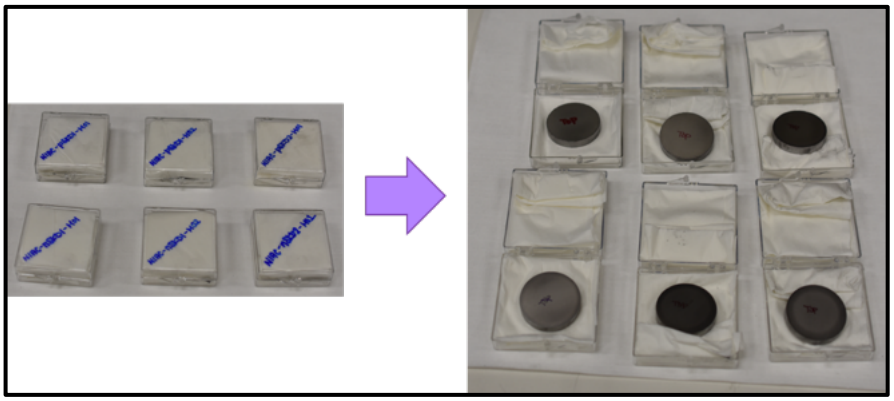

Figure 51. 1.250" metallized p-type and n-type skutterudite pucks.

inspection of the pucks was performed to ensure they are within specifications for the device to be fabricated.

Upon ensuring the parallelism and flatness of the metallized pucks, the next step was to dice the pucks into legs. Figure 52 shows the dicing process. The pucks were mounted onto a mounting block and diced using a wafer saw. Each leg was oversized by ~400 µm for post-surface cleaning and final dimensioning. A total of 26 legs can be diced from a 31.75 mm metallized puck. As shown in Figure 52, the legs were labelled based on their location in the puck. Overall, two (2) p-type and two (2) n-type skutterudite metallized pucks were diced. No delamination was observed for any of the legs post-dicing.

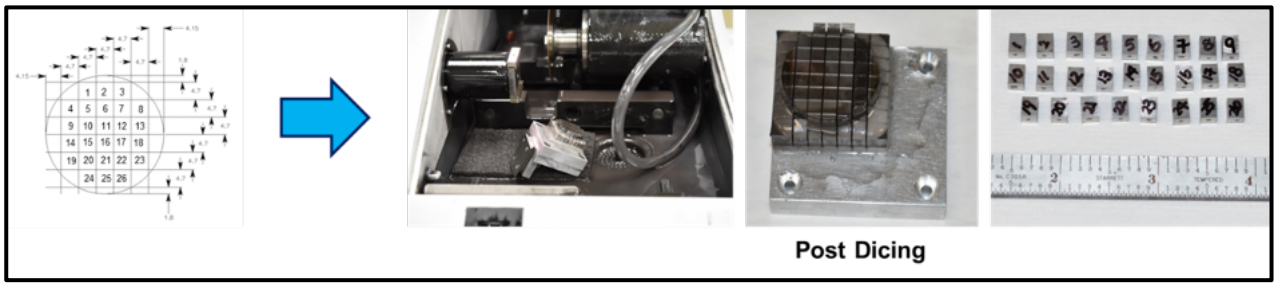

Figure 52. Metallized puck dicing process.

After dicing, each leg was inspected to check for any cracks. It was observed that legs towards the edge of the pucks show some degree of cracking in the bulk TE materials. These elements were not used for the SKD bi-couple fabrication process (total yield was ~54%). After the as-diced leg inspection, the legs were then polished to the targeted dimensions (5 mm high and 4x4 mm cross section) as shown in Figure 53, followed by a final optical inspection.

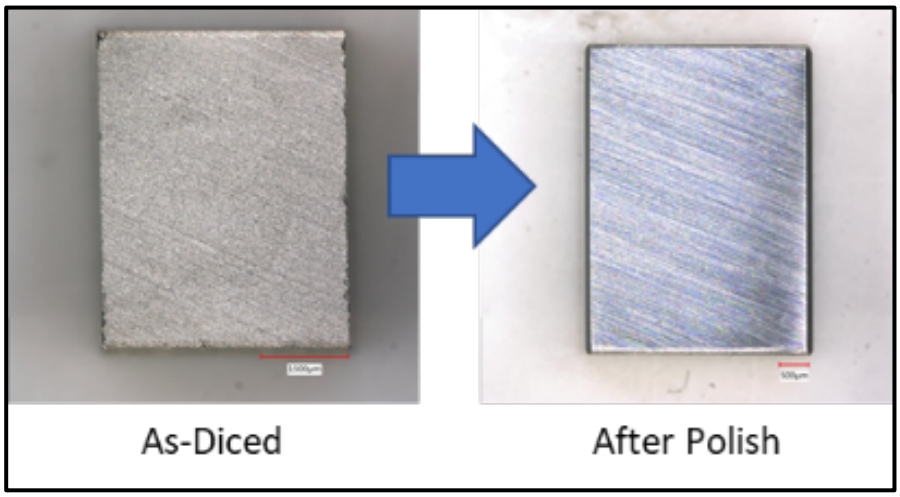

Figure 53. TE Element preparation: as-diced and after polishing.

5.5 Pre-made hot-side interconnect

Before starting the bi-couple fabrication process, the hot-side metal interconnect was attached to a commercially available metal coated dielectric pad, to prevent shorting of the couples. Prior to bonding, the metal interconnect was sputtered with an adhesion layer. Next, the hot-side interconnect was pre-attached to the dielectric pad with an active braze in between the metal interconnect and the dielectric pad. Then the dielectric pad was brazed at a temperature higher than the operating temperature, as shown in Figure 54 After the brazing process, a resistance check was conducted to ensure the pads are not electrically connected, as shown in the figure. A total of 4 hot-side interconnects were fabricated.

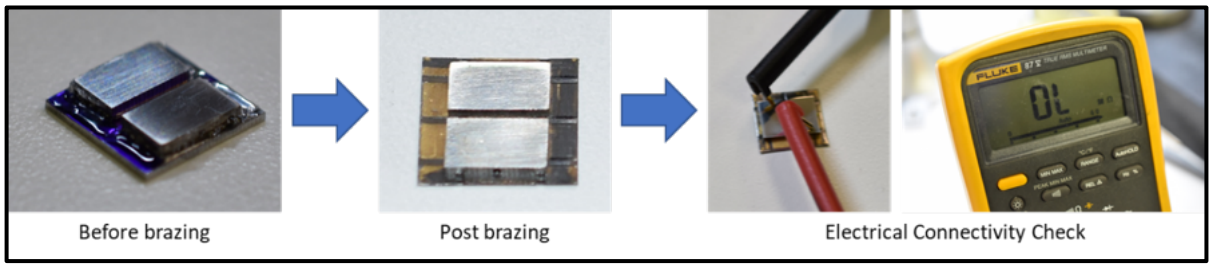

Figure 54. Pre-made hot-side interconnect and electrical connectivity check.

5.6 Bi-couple Fabrication

The next step in the SKD bi-couple fabrication was to join the TE legs (p-type and n-type) to the pre-made hot-side metal interconnects and cold-side metal interconnects via a brazing process. Prior to bonding, the hot-side metal interconnects, TE legs, and cold-side metal interconnects are sputtered with metal prior to the brazing process. Figure 55 shows the skutterudite bi-couple fabrication process flow. First, the cold-side metal interconnects were attached to the pre-made alignment grid pads. The spacing between the pads was then inspected to ensure that spacing was ~1mm for electrical isolation. A thin layer of braze material was then applied on top of the p-type and n-type SKD elements prior to attaching them to the cold-side interconnects. The process was repeated to attach the SKD elements to the hot-side metal interconnects. After all the TE elements were attached, a final check was conducted to ensure proper alignment prior to the final brazing step. The SKD bi-couple fabrication was done in one final brazing step to attach the hot-side interconnects and cold-side interconnects simultaneously.

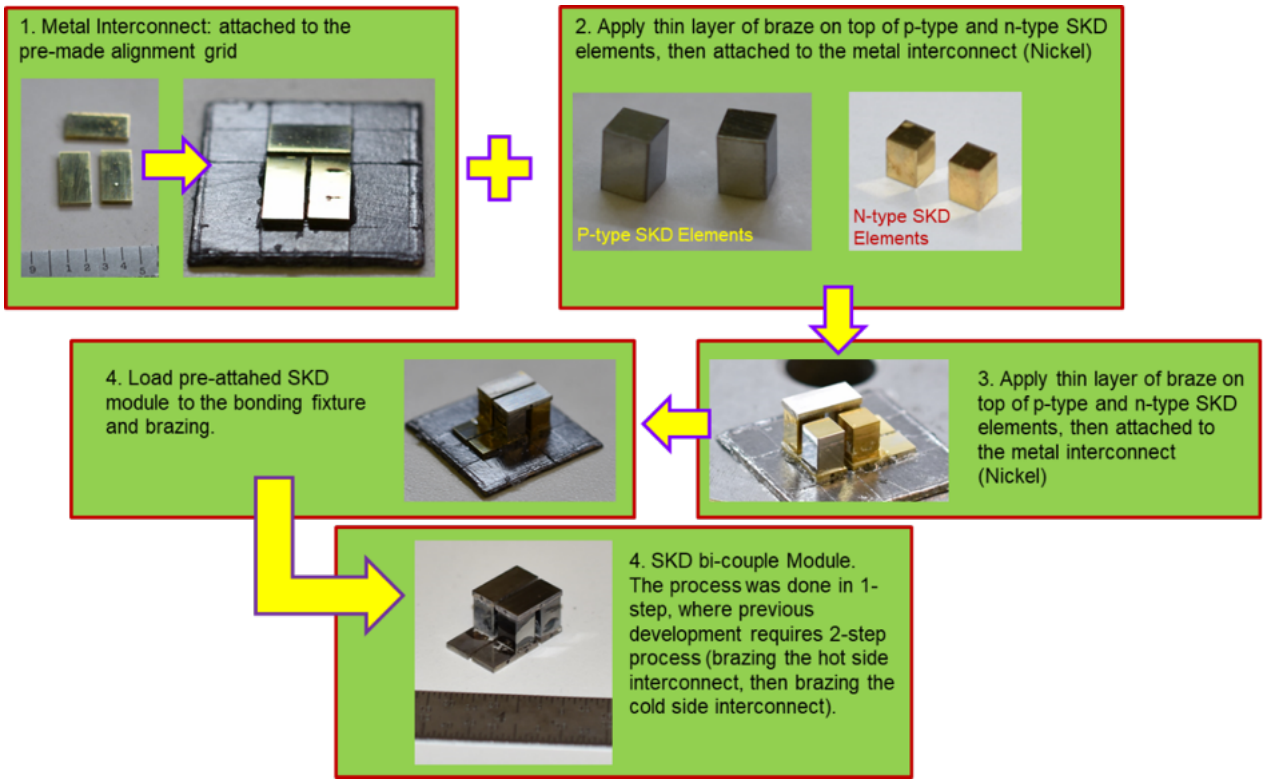

Figure 55. Skutterudite bi-couple fabrication process flow.

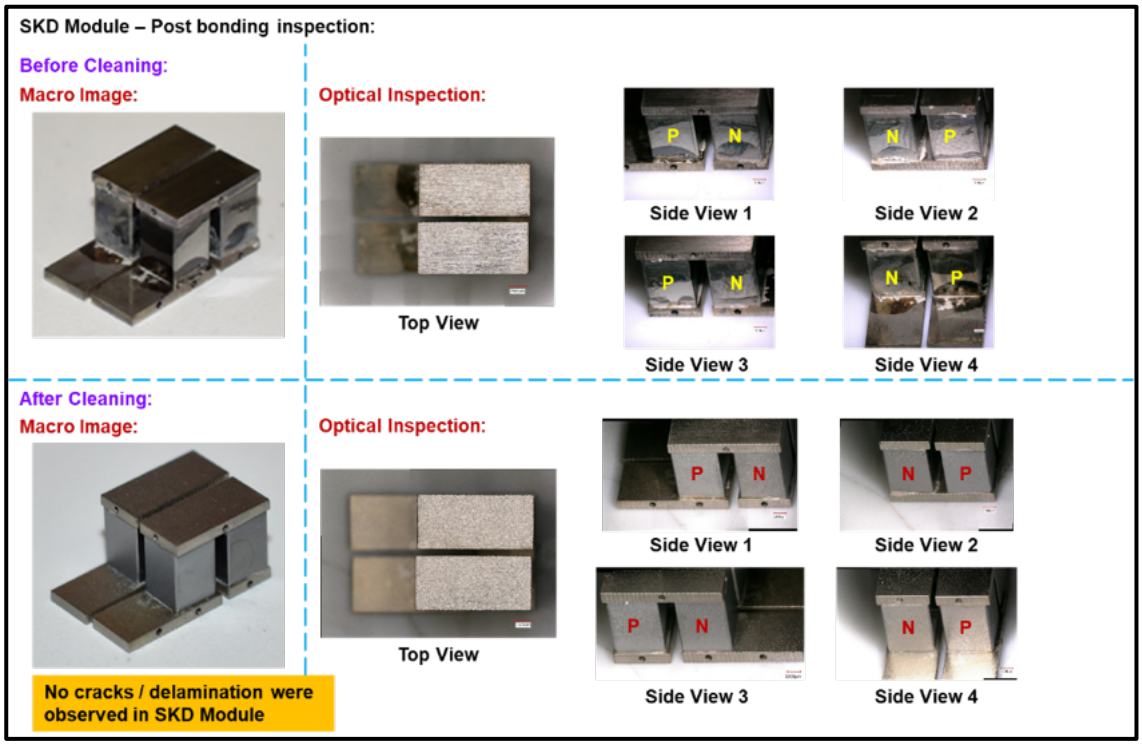

Figure 56. Skutterudite bi-couple #1 post bonding inspection.

After the brazing process, an optical inspection was conducted to check for any cracks before and after cleaning, as shown in Figure 56 for bi-couple #1 and Figure 57 for bi-couple #2. For skutterudite bi-couple #1, the cross-sectional area of the p-type and n-type SKD elements was 4.00mm x 4.00mm and the height of the TE materials was 5.1 mm. For Skutterudite bi-couple #2, the cross-sectional area of the p-type and n-type SKD elements was 4.00mm x 2.91mm, and the height of the TE materials was 5.1mm. The change in the cross section was implemented to better accommodate the hot-side dielectric relatively small footprint. The elements that were used for fabricated bi-couple #1 and #2 was from the 1st batch of p-type and n-type skutterudite powders.

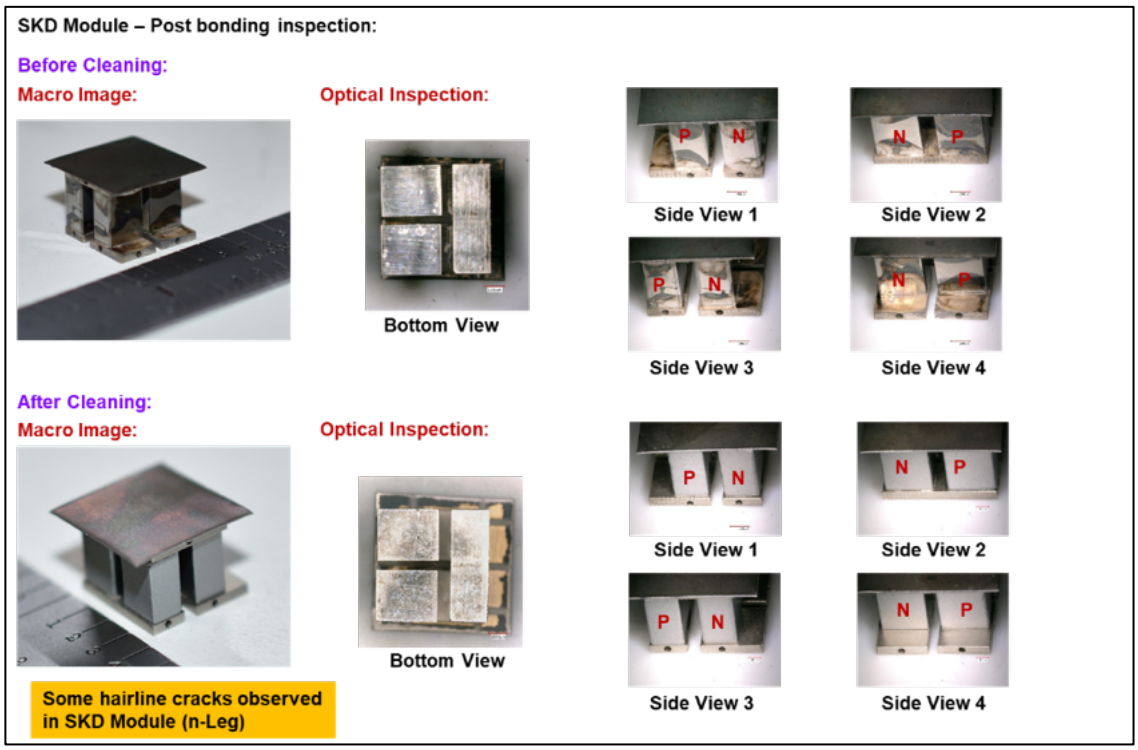

Figure 57. Skutterudite bi-couple #2 post bonding inspection.

For skutterudite bi-couple #1, it was delivered for the testing and characterization. For skutterudite bi-couple #2, the goal was to include the dielectric layer and encapsulate the bi-couple with aerogel for power performance testing at Aerospace Corporation. All sides of the bi-couple were inspected prior to cleaning to see if there are any cracks observed in the TE bulk material. From the optical inspection, there was no cracks or delamination observed in the skutterudite bi-couples. After the post-brazing inspection, the bi-couple was sand-blasted to remove to clean up SKD elements for optical inspection prior to aerogel encapsulation. The end-to end bi-couple electrical resistance was measured before and after cleaning and the results are captured below. A hairline crack was observed in the n-leg of the bi-couple #2.

5.7 Aerogel Encapsulation

The final step for bi-couple #2 was to encapsulate the bi-couple with insulating aerogel. The purpose of the aerogel encapsulation was to minimize the heat loss during operation as well as to minimize sublimation of the skutterudite materials at the higher temperatures. An ambiently dried aerogel was used in this case.[73] Figure 58 shows the aerogel encapsulation process. First, the bi-couple was placed in the encapsulation mold, and a metal wire was inserted as a mask for the thermocouple/voltage tap hole. The sol-gel solution was then poured into the mold up to the cold-side metal interconnect which is left exposed. The mold was then covered with an aluminum foil to allow for slow curing as well as protection from debris and was left to cure overnight. After the aerogel process was completed for bi-couple #2, a crack in the aerogel was observed at the edge of the hot-side interconnect (possibly a crack initiated from the sharp edge in the corner). This is not expected to impair the insulation of the bi-couple. The final step is to trim the excess of the aerogel off, as shown in the last image.

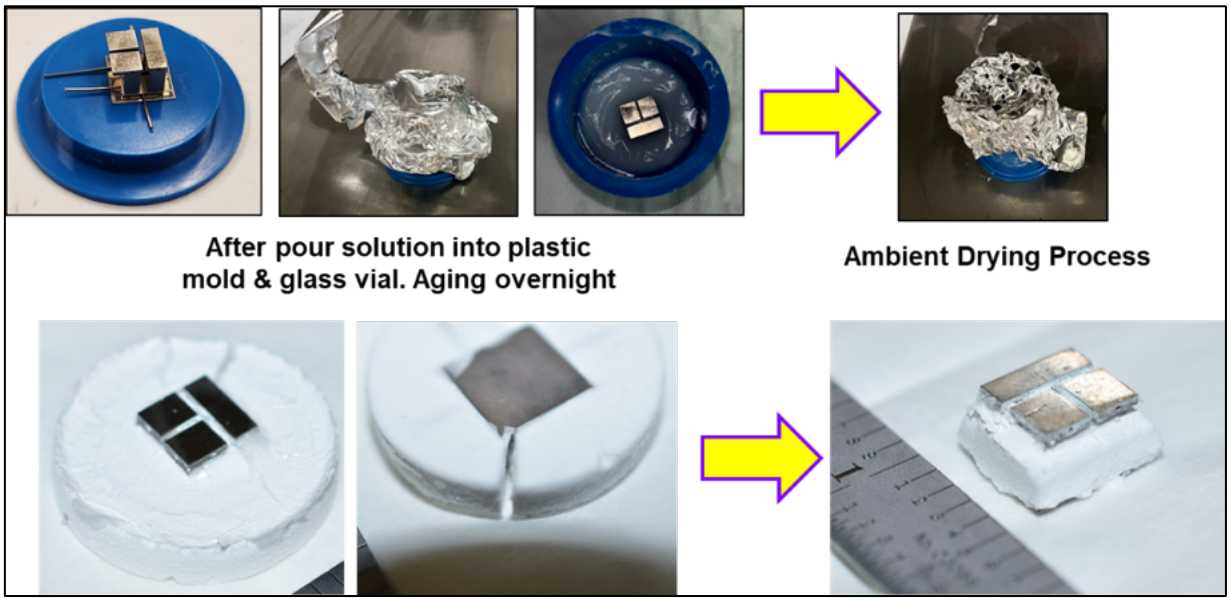

Figure 58. Aerogel encapsulation process.

5.8 Bi-couple Resistance Measurement

Figure 60 and Figure 59 show the end-to-end resistances of the skutterudite bi-couples #1 and #2. For skutterudite bi-couple #1, the end-to-end resistance (P1-N1-P2-N2) is consistent, with an increase of ~2% in resistance after the bi-couple final clean-up. For skutterudite bi-couple #2, there was an increase in end-to-end resistance after cleaning, which was consistent with the optical inspection (a hairline crack was observed after cleaning). It is possible that there is a microcrack that was not observed prior to the cleaning process. After the aerogel encapsulation, there was a small change in end-to-end resistance, within the measurement uncertainty. Bi-couples # 1 and # 2 have

Skutterudite Module #1

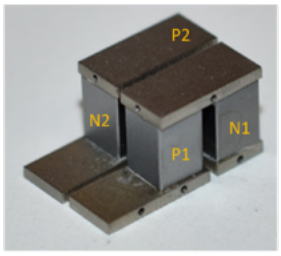

End-to-end Resistance Measurement:

	Calculated Resistance (mΩ)	Resistance Before Cleaning (mΩ)	Resistance After Cleaning (mΩ)
P1	2.45	2.40	2.44
P1-N1	4.42	4.47	4.49
P1-N1-P2	6.91	6.84	6.97
P1-N1-P2-N2	8.87	8.95	9.07

Figure 60. End-to-end resistance measurement for skutterudite bi-couple #1.

Skutterudite Module #2

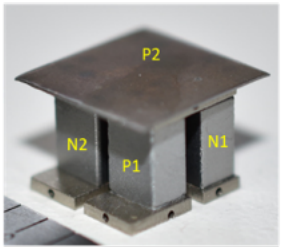

End-to-end Resistance Measurement:

	Calculated Resistance (mΩ)	Resistance Before Cleaning (mΩ)	Resistance After Cleaning (mΩ)	After Aerogel Encapsulation (mΩ)
P1	3.39	3.35	4.73	-
P1-N1	6.06	6.15	7.86	-
P1-N1-P2	9.47	9.38	11.38	-
P1-N1-P2-N2	12.16	12.19	14.37	14.41

Figure 59. End-to-end resistance measurement for skutterudite bi-couple #2.

different calculated resistivities, is mainly due to the cross-section area difference (as it was mentioned in the skutterudite bi-couple fabrication section).

Skutterudite bi-couple #2 was assembled into the fixture for benchtop measurement as shown in Figure 61. The two bi-couples were delivered for testing (bi-couple #1) and proof of performance validation (bi-couple #2). For bi-couple #1, the n-leg were broken during handling and could not be used for testing. Bi-couple #2 was used to conduct temperature dependent performance as shown in the next section.

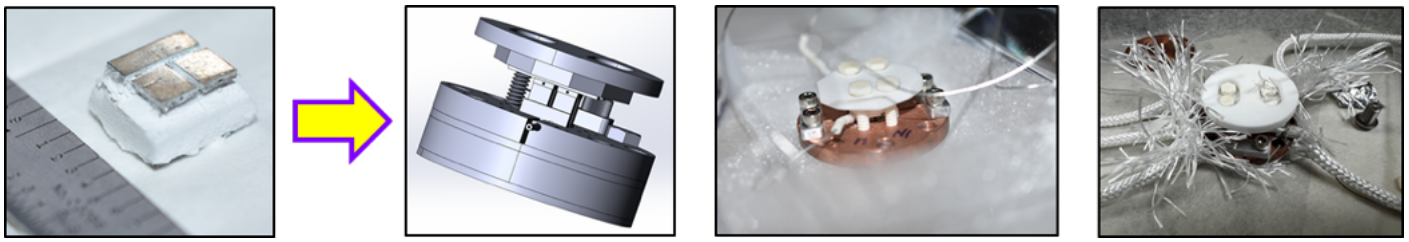

Figure 61. Integrate skutterudite bi-couple #2 into benchtop fixture.

5.9 SKD Junction Fabrication Conclusions

The SKD fabrication process overall delivered a single unit for testing at Aerospace, and had some cracking the in the junctions that limited testing. Synthesis and fabrication of single units such as performed here are very expensive and time consuming, and

required extensive hand labor. Commercialization of this material will require investment in the milling and hot pressing, as well as cutting and brazing steps to ensure high quality units and volume production.

6. Thermoelectric Testing

6.1 Introduction

For verification of thermoelectric properties of the SKD arrays fabricated at JPL as well as experimental investigation of the thermal simulations performed at Aerospace, thermoelectric energy generation was tested using a thermal simulator, a resistive heater, as neither Pu-238 or Am-241 was available for testing. Thermal simulators such as the one used in this study are the standard method for testing thermoelectric devices for RPS due to the difficulty and cost associated with procurement of appropriate radioisotopes. As seen above, the differences between using resistively generated heat and an isotope source are similar, as the thermal simulations only account for total heat generated, and the amount of radiation contributed by the isotopes is negligible with respect to heat generation.

6.2 Experimental Setup

An experimental apparatus was developed to test the SKD thermoelectric interface developed at JPL for APPLE. The experimental goal was to measure the operation of the prototype device by measuring the open circuit voltage as a function “hot shoe” temperature. Figure 62 shows a schematic of the thermoelectric generator (TEG). The skutterudite TEG is a two junction, four leg unit configured in series. Figure 62 also shows the gray interconnects between the legs, including the power and measurement taps at the ends of the device circuit, and the thermal gradient across the leg units. Due to the two types of material developing opposite potential gradients in response to a temperature gradient, the thermal gradient rises and falls across the electrical circuit, resulting in an accordion like configuration of the thermoelectric device across the circuit. The two power connections are linked to a variable load and a voltammeter for voltage measurement.

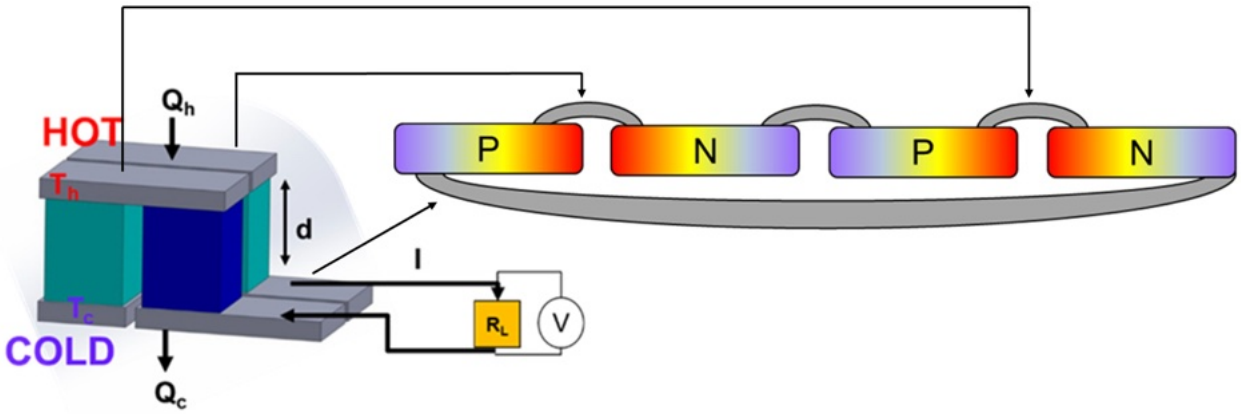

Figure 62. Schematic diagram of the skutterudite thermoelectric generator, with an expanded image showing the interconnects and the temperature gradients through each leg.

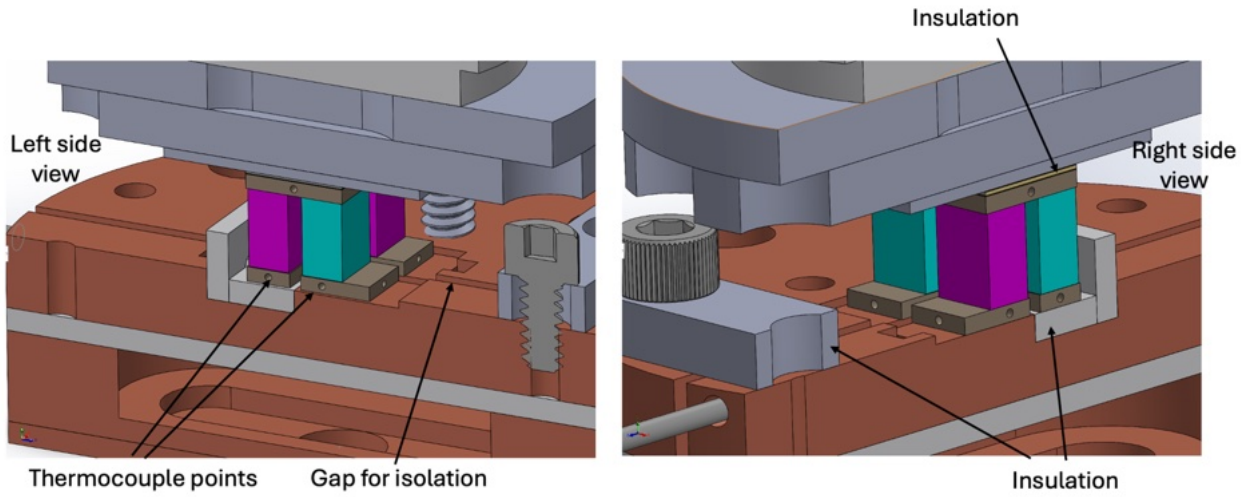

Figure 64. CAD for the thermoelectric testing jig, showing thermocouple locations and electrical isolation.

In a completed thermoelectric power system, good thermal connection between the hot and cold shoes are engineered by the device enclosure to deliver sufficient compression. Testing this device required a mechanical framework that would ensure good compression on the device stack as well as electrical insulation of the components from the heater, and hold wires in place to prevent shorts across the circuit. Figure 64 shows the CAD for the testing jig, including locations for thermocouple connections, as well as points of electrical isolation. The jig is formed of two copper half moons that connect to the two power terminals of the thermoelectric device, with a gap between for isolation. The jig also has insulating Macor, a glass-mica ceramic placed at the base of the middle legs to prevent a mid-circuit short, as well as this insulating ceramic across the top of the device to prevent shorting from the metal heater plate. This configuration provides vertical compression from screws holding the top heater plate to the base copper plates, ensuring good thermal contact throughout testing. The jig also provides structural stability of the device during testing that would normally be provided by the RPS structure and packaging. This device was instrumented with K-type

Figure 63. The prototype TEG device encapsulated in the jig.

thermocouples at each TE leg/interconnect location for measuring ΔT during thermal testing.

6.3 Sample Instrumentation

Thermoelectric testing experiments were done on the laboratory benchtop to allow for secure control of the thermocouple and electrical connections. While testing the TE device in a vacuum chamber would be more flight like for a vacuum configuration RTG such as the GPHS-RTG used for deep space operation, testing without vacuum will both suppress sublimation of the SKD TE materials, but also allow for a more direct comparison to the existing heritage option, the MMRTG, which has an inert atmosphere surrounding the PbTe/TAGS thermoelectrics. Using air rather than Ar or He as an inert gas has minimal effect on the operation of the TE for short durations, resulting in negligible oxidation of the SKD even at high temperatures.

Figure 65 (left) shows the device mounted on a cooling plate driven by a closed cycle water chiller that could reach down to 2 °C. The stainless steel cylindrical unit is a resistive-heater connected to a temperature controller that can reach 1000 °C. The heater unit is lowered on to the hot side of the TEG during the experiment. Both the thermocouple (TC) and electrical wiring are electrically insulated using fiberglass weave. A 20 channel calibrated data logger was used (Agilent 34970A) to measure the temperature from all the thermocouples along with open circuit voltage. The Agilent has a built-in thermocouple reference junction and can cycle through all the channels at a rate of 60 channels/sec. Figure 65(right) presents a collage of images from the experimental setup. The testing included two embedded TCs, placed at 1) on cooling plate, 2) on copper block-cold side, 3) on ceramic-Hot side, and 4) on heater unit for comparison. The data from the Agilent was collected using a computer and a data being taken on all channels at a one second interval.

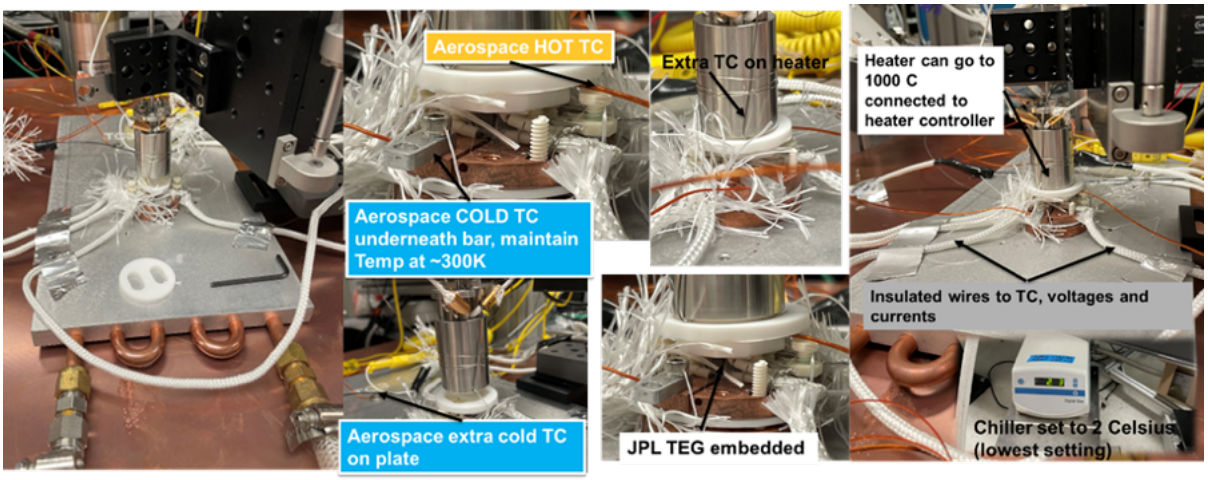

Figure 65. The experimental setup at room temperature and pressure. (left) the prototype device mounted on a controlled temperature cooling block that can reach down to 2 ˚C. The silver cylinder is the heating unit which is on an independent controller and can reach down to 2 ˚C. The silver cylinder is the heating unit which is on an independent controller and can reach 1000 ˚C. (right) a collage of images showing the insulated wiring and TC layout.

For evaluation of the device design to keep a room temperature cold shoe, the cold side temperature of the TEG was maintained close to 300K while the hot side temperature was increased. This enables an understanding of the capability of the APPLE device to operate at near room temperatures at the cold shoe, as in a vehicle design where the APPLE provides a temperature compatible with components such as batteries and electronics, removing the need to qualify spacecraft components to wide temperatures ranges. An experiment run consisted of cycling the heater to increasingly higher hot shoe temperatures with periodic cooling periods, while maintaining the 300K cold shoe (radiator) temperatures. As noted previously, the life expectancy of an SKD-APPLE device is directly affected by the SKD temperature at the hot shoe interface, with sublimation of the SKD as the primary life limiter. Lower temperature operation of the TE can be considered for lengthening the TE function.

6.4 Temperature Dependent Power Generation

Figure 66 shows the results of an experimental run as a function of time. Two data outputs are plotted. The data in blue represents the Delta temperature (T_H -T_c) between the hot and cold shoes with y-axis on the left while the data in orange is the TEG open circuit voltage with vertical axis on the right. The TEG voltage output follows the temperature cycling. The cold side temperature was maintained as close as possible to 300 K through a feedback loop to the chiller.

To first order, the open circuit voltage V_{OC} is related to the $\Delta T = (T_{Hot} - T_{Cold})$ by the equation $V_{OC} = S*\Delta T$ where S is the Seebeck coefficient for the skutterudite material. The literature suggests that the Seebeck coefficient for the $CoSb_3$ based TEGs is on the order of 200 μV/K.[74] Table 1 presents the results of the calculated Seebeck coefficient using

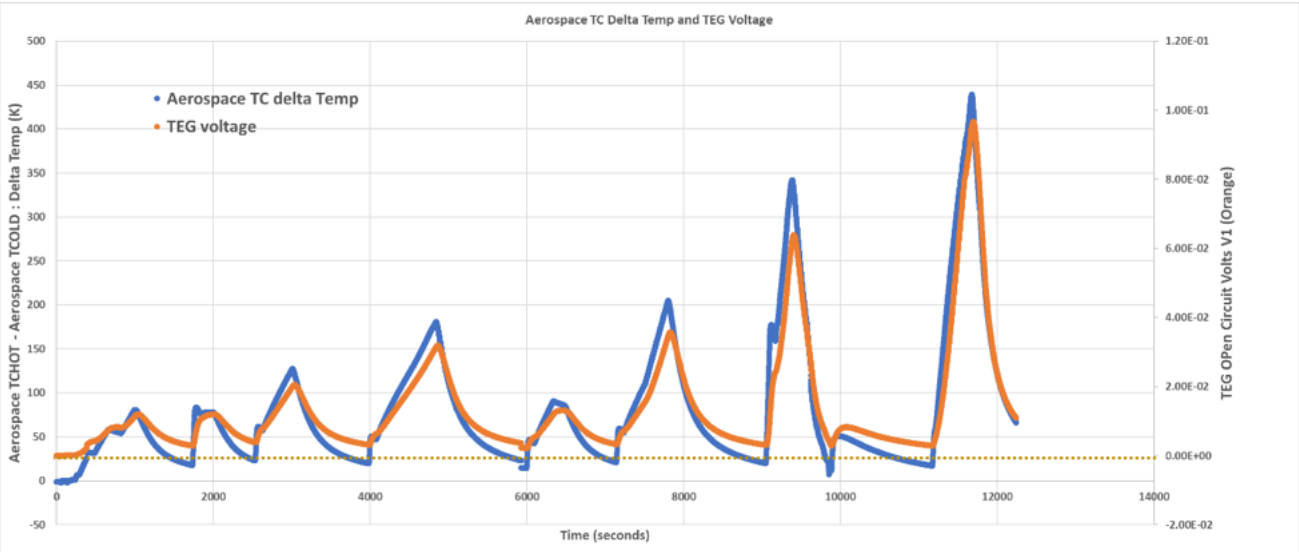

Figure 66. Data output from the prototype device showing the temperature difference (Hot - Cold) across the TEG (Blue curve) and generated open circuit voltage (orange).

Table 5. Calculated Seebeck coefficient from measured data.

Seebeck Coefficient, S (μV/K) from the data	Measured TC HOT (Kelvin)	Measured TC COLD (Kelvin)
150.1	354.9	300.2
136.4	383.6	299.8
143.6	400.4	301.8
153.0	425.8	306.0
161.4	451.0	310.0
167.1	480.0	315.4
177.1	500.6	321.5
147.2	525.4	306.0
163.6	600.1	315.0
212.7	700.3	325.0

the measured V_{OC} and ΔT data. In comparison to the literature, our results suggest a Seebeck value that is ~25% less than what is reported. To address this, we believe the following and using the schematic of figure 1, the equation for the measured voltage V can be written as $V=IR_L = (S*\Delta T - IR)$ where R_L is the shunt resistance at the Agilent probe, R is the internal resistance of the 4 junction series TEG and *I* is the driving current. If R is close to zero and R_L is high impedance, the measured voltage is close to the ideal open circuit voltage V_{OC}. If R is not close to zero, then there is a non-infinitesimal voltage drop across the TEG and the measured voltage would be less for a given ΔT and the measured V_{OC} would also be less along with the Seebeck coefficient. However, at one instance of package clamping and at the highest temperatures applied (T_H = 792K and with ΔT = 455K) we did measure a V_{OC} of 124 mV and Seebeck value of 272.

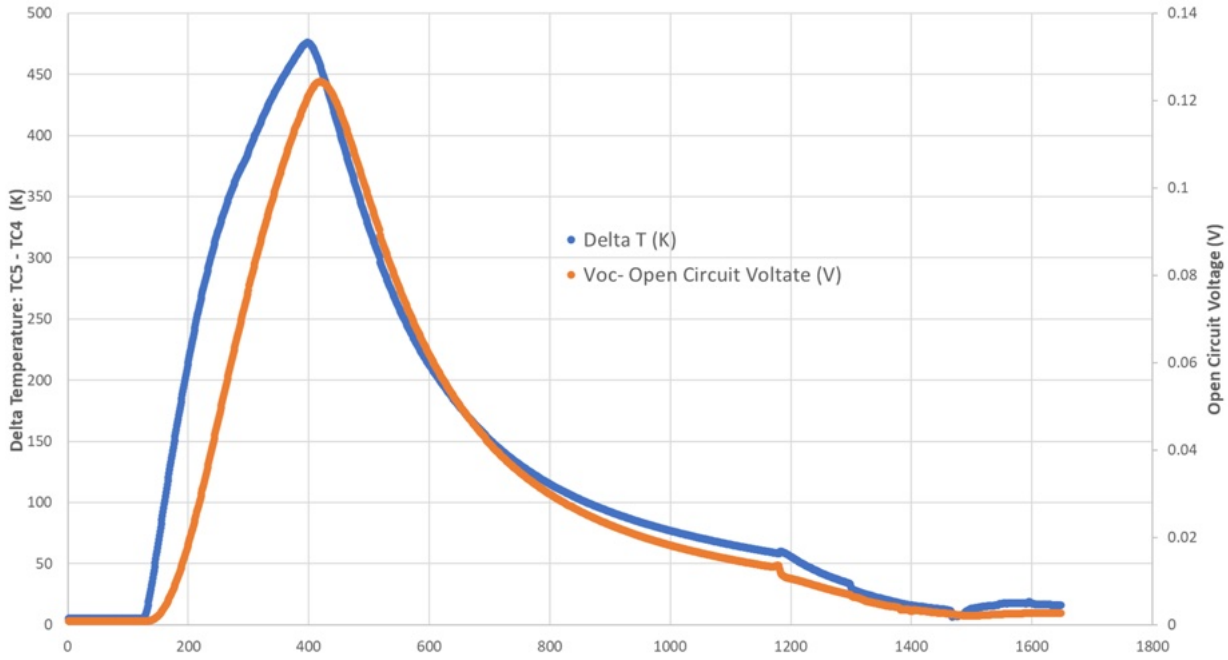

Figure 67. Increasing the clamping pressure resulted in higher OCV measurements vs ΔT, indicating that packaging of the device is critical to function.

6.5 Thermoelectric Junction Testing Conclusions

Testing of the TE junction did show voltage and current generation, though less than predicted for the current, though the predicted current is 10A, a value far higher than can be sustained by these components. A key step in Phase III will be to increase the number of junctions to increase the output voltage, reducing the current value to ~2A, allowing for reasonable conductor cross sectional areas and inputs into the vehicle bus. A larger set of junctions could not be fabricated under the allotted funds for this Phase II, but can be demonstrated in Phase III. It should be noted that the total interface area of the n- and p-type materials defines the heat flow between the hot and cold shoes, and to maintain the target temperatures from this study, the leg total area would need to be kept the same, resulting in thinner legs, which may increase fabrication issues.

7. Mission Context

7.1 Introduction

The APPLE architecture has three fundamental attributes. 1) It generates power, 2) it stores energy, and 3) it provides heat that can be used to keep spacecraft components warm. These attributes make APPLE most useful for space missions where solar flux is low, and temperatures fall below the operational requirements for instruments requiring additional power for component heating. The missions could be in-space missions and/or off-world ground missions (e.g., planets, moons, asteroids). In the thermal simulations above, the radiative surface was simulated as transmitting energy to space to generate the required ΔT, but the radiator can function through other heat transport mechanisms like conduction and convection in addition to radiation. This means that APPLE can be adapted to other environments than deep space. For example, an APPLE powered mission could be used in a rover on a rocky planet or swimmer on Enceladus, with heat transport to a wispy atmosphere or a liquid environment. The thermal transport would need to be simulated for each of these environments, and would give rise to different radiator designs to maintain desired battery temperatures and hot shoe-cold shoe ΔTs. Depending on the radiative properties of the environment, the efficiency of the radiator may be better or worse, though typically the addition of convective and/or convective heat transfer would be beneficial. In certain applications, however, it may be worse; for example when a radiator faces a nearby highly thermally insulating regolith, which an insulator almost as good as aerogel ($2.3x10^{-3}$W/mK vs $1.5x10^{-3}$W/mK).[75]

7.2 APPLE Unit Designs

The APPLE design presented here has a key feature improving over previous RTG designs. The small scale of individual units allows for distribution of heat generation. This in turn allows for more facile heat transport across the vehicle APPLE is powering. With a single location where heat is generated (leveraged in previous designs to increase the hot shoe temperature for a larger ΔT) the cold shoe temperatures of heritage designs were still relatively hot compared to conventional component temperature requirements. For example, the MMRTG typically has cold shoe temperatures of 212˚C and the GPHS-RTG was 302˚C. This necessitated placing the radiative surfaces far away from electrical components which are typically qualified to max temperatures between 50-80˚C. By using the spacecraft chassis as the radiator, the (additional) radiator mass can be removed, and make the structural and functional components of the vehicle do double duty. This does bring the component temperature requirements into the APPLE and APPLE-powered mission design. APPLE is designed and sized such that ~400 cm^2 of radiative area per APPLE unit is required, which results in a cold shoe/radiator temperature range between 10-30˚C, well within not only normal component operating temperatures, but also with the range of what is typically the most thermally sensitive component of the vehicle, the Li-ion battery. As noted, the radiator simulations were for equilibrium with deep space as the radiative cold sink, and this radiative surface requirement would need to be changed depending on the radiative

environment, which may benefit from convective transfer, but may also suffer from additional insolation and heating, for example the vehicle is sitting in sunlight on the lunar surface. Only the ΔT between hot and cold shoes matter for energy conversion, whether that cold shoe is in radiative equilibrium with the background of space or in a steady state heat transfer condition to the spacecraft.

7.3 APPLE-Lunar Seismic Mission

A key mission location for a small, modular RTG powered mission is the moon. With the difficulties in surviving the 14-day lunar night at mid latitudes and the low to nonexistent solar illumination at the poles, RTGs are needed for any mission longer than a lunar day. As a science target, the moon contains important clues into Earth's history, including Earth's formation, molten core development, and early periods of surface impacts. Due to the moon's cessation of dynamic geologic activity it reflects the early composition, crust formation, and evolution of Earth and other planetary bodies. Seismic measurements are the most direct method for scientific investigation of the lunar crust, mantle, and core. An APPLE powered Lunar Seismic Mission will collect short and long period seismic vibrations, which will open up our understanding of lunar and terrestrial geologic evolution. In addition, with the onrush of new lunar missions, including planning for long term emplacements and hopes for permanent structures on the moon, a better characterization of present day lunar activity is critical for the durability and safety of lunar missions. Based on existing lunar seismic data provided by the last lunar RTG powered seismic studies, the Apollo Lunar Scientific Experiments Package (ALSEP), moonquakes may pose substantial risks to future Artemis and other lunar missions.

An APPLE-Lunar Seismic Mission would involve the deployment of a number of measurement nodes at dispersed locations on the surface. The APPLE-Max concept would form nodes for a network of seismic sensors on the moon for collecting and collating seismic data simultaneously across the moon. The individual seismic payloads would be ~20 kg, and generate 20 W of power and need to dissipate 300W of heat. Individual nodes would carry seismic instruments to probe the interior structure of the moon. Each node would be a powered by 12 APPLE units, generating heat from either Pu-238 or Am-241 depending on isotope availability. The mission life would for a minimum of 7 years, with a goal of 10 years of continuous operation, made possible by RTG power and heat. Each node will be deployed on separate lunar landers, deployed to trans-lunar injection from a Falcon-S2 unit. The S2 will be launched to lunar orbit in partial reusability configuration (two boosters would perform barge landing, with expending of the center core S1 unit. Once deployed to lunar injection, four landers will be targeted to their landing targets through separate trajectory maneuvers.

After breaking burns, the landers will separate from their deployment vehicle and perform landing burns under visible, radar, and laser navigation. Once landed, the lander will deploy to the ground, and keep the seismic unit on the lander deck, with mechanical/vibrational contact to the regolith. The seismic experiment will be powered by four of the APPLE units, delivering 20 W_e to power a seismic sensor, data logger,

flight computer, thermal regulation system, and periodic data transmission. After deployment, the seismic experiment portion of the mission will operate for at least 7 years, collecting data and transmitting telemetry to an orbiting satellite for relay to the Lunanet proposed network. Powering the data transmission will be a trickle charged 40 Wh Li-ion battery. Choosing a set of mid to low latitude mission sites, power and heat for the mission are the key technical areas. For the sites experiencing the lunar day, surface temperatures will range from -173˚C to +117˚C, for a seven year mission, the landers will experience around 90 lunar day-night cycles, causing wide temperature swings. APPLE's supply of heat ($300W_{th}$) can be used to mitigate the low side of the temperature swings, at the cost of increasing the difficulty in heat rejection during the lunar day. The lander will deploy to the surface, and the seismic payload will operate for the remainder of the lunar day using attached solar panel, including operation of other payloads on the lander, and the initial stage calibration operations of the seismic sensors. After sun set on the lander, it will end its active mission, which may include additional lunar surface payloads. The lander post-mission will still perform passive thermal regulation for the seismic payload located on the lander deck. The lander can use several passive thermal regulation methods to prevent overheating of the seismic payload during the lunar day. To maintain temperatures during the lunar day, a skirt between the lander legs can shield the seismic payload from the sun. The skirt will be oriented south (northern hemisphere) or north (southern hemisphere) with substantial east/west extension to maintain the seismic payload in shadow during its mission, while maintaining a substantial fraction of the sky for radiative emission for cooling either through radiators located under the lander or through heat transport thorugh the lander to radiators placed on the lander exterior. The skirts will have a radiator facing skyward with a thermal coating with a low solar absorptivity can maintain radiative emission similar to the Surveyor spacecraft.

7.3.2 A Tech Demonstrator Mission Deep Dive

While the design above creates a network of seismic sensors, the isotope requirements per unit (600g Pu-238, 3 kg Am-241), and for the whole network (2.4 kg Pu-238, 12 kg Am-241) may well exceed the amount of isotopes available for such a mission in the near future, preventing of testing this technology. A smaller tech demonstrator mission could be designed to us the absolute minimum amount of isotope. A lunar mission developed for APPLE as a tech demonstrator involves very low power seismic sensors on the moon. The Radioisotope Powered Lunar Seismometer (RIPLS) brings the technology advancement from the NIAC Phase II work at the Aerospace FFRDC on developing a small, ^{241}Am radioisotope power system together with the low power, low-noise seismic sensors such as those designed by the University of Arizona for a long duration (10+ years), seismic mission for a new generation of lunar seismology. Leveraging the Atomic Planar Power for Lightweight Exploration (APPLE) RPS developed under NIAC, which generates 17 W of thermal power and 1.7 W of electrical power using a ^{241}Am isotope core and high efficiency skutterudite thermoelectrics, the RIPLS tech demonstrator project would develop a tech demo of an integral RPS seismic payload for lunar deployment. The key element to this demonstrator mission is the very

small amount of Americium-241 required. The heat and power requirements for missions to live through the lunar night have only been reliably solved through radioisotope heat, but the massive size of NASA's only current radioisotope power system (RPS) design (MMRTG, Multi-Mission Radioisotope Thermoelectric Generator) coupled with the lack of any ^{238}Pu allocated for lunar missions requires a new heat and power source for lunar missions to operate through multiple lunar nights. While the UK's National Nuclear Laboratory and University of Leicester are producing alternative isotope clads of Americium-241,[76] a non-Pu powered technology that enables distributed long-duration seismic missions is a critical need for NASA's lunar science and exploration goals. With Europe only fabricating small numbers of ^{241}Am clads this decade,[77] and no ^{238}Pu allocated for lunar missions,[78] for NASA to have a radioisotope mission on the moon it would need to operate on a single 20 W thermal ^{241}Am source like the small, efficient RIPLS. Other funded RPS developments such as the Zeno/Intuitive Machines collaboration[79] all require vastly more ^{241}Am than will be produced, much less what is likely to be offered to NASA. With no ^{238}Pu available for NASA lunar missions[78] and Europe potentially only making single ^{241}Am clads available to the US, only RIPLS will be capable of delivering an RPS powered payload to the Moon for NASA. RIPLS matches the mission to the limited availability of the key resource, ^{241}Am, and is the pathfinder for bringing radioisotope power back to the Moon.

Developing this RPS seismic sensor will enable small scale radioisotope powered missions, separating the previous RPS context from large flagship missions and providing a power capability to missions that most critically need RPS both for power as well as for heat. The main thrusts in this project would be 1) developing the lunar seismic science needs and requirements, including sensor, comms, location, and thermal inputs; 2) establish the RPS and package design, including the thermal design, thermoelectric configuration, and power system, and comms for build; 3) seismic sensors, with data logger, control, and compression hardware; 4) system integration, using the seismic sensors, and integration with the power system, comms, and control computer; 5) system test and characterization, including T-vac and vibration environments.; and 6) mission design and CONOPS, including lander and relay requirements, deployment, and data handling.

RIPLS is conceived to operate as a standalone system. It has its own power and its own data transmitting capability, and can operate throughout the lunar day and night. The flexible packaging and the communication solution can work located on the lunar surface or installed on the lander, and act independently or part of a seismic network.

RIPLS is powered and heated by the existing NIAC Phase II APPLE RPS design, based on a UK ^{241}Am unit in a Pt/Ir shielding clad. It is this cold shoe (radiator) interface temperature that allows for the intimate integration of the APPLE RPS design with a sensor. Currently the SKD technology is at TRL 4, and the skutterudite TE materials and devices have excellent stability and relatively low degradation rates with projections at the end of 17-year design life, ideal for long duration missions.[80]

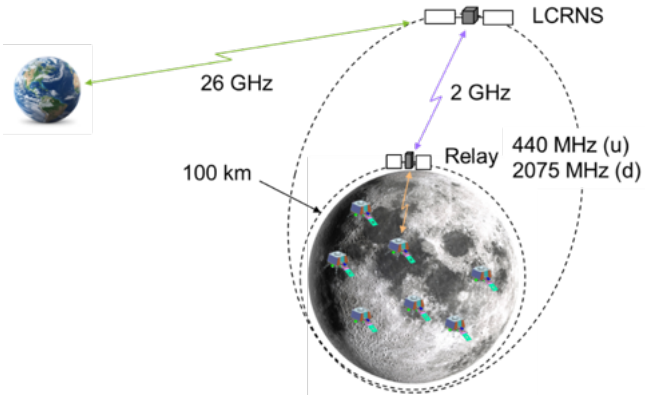

Figure 68. RIPLS proposed downlink scheme showing the relay satellite proposed to bridge the gap to LCRNS.

Communication design for RIPLS will flow up requirements for a low-lunar orbit satellite to collect data for downlink to Earth. The relay satellite (Figure 68) will transfer its data to the Lunar Communications Relay and Navigation Systems[81] (LCRNS) satellite, currently planned for an 8,000 km apogee, and be transferred back to Earth.

The RIPLS instrument would to generate 760 MB of data per lunar day and our link budget closes with a 2-watt transmitter at 433 MHz for 1.2GB allowing margin. The relay satellite in low lunar orbit (100 km altitude) will be visible to RIPLS for 200 minutes of each lunar day. A pair of quadrifilar antennas, one for the uplink and one for the downlink have the right pattern and gain for our instrument which is intended to be oriented with the antennas facing zenith. One antenna at each of the frequency bands listed in the Lunanet Interoperability Specification Version 4 are used.[82]

In the system block diagram, (Figure 69) the Aerospace electronics subsystem is in purple, and the seismic subsystem is in orange. The Science computer is dedicated to the task of collecting seismic data, time stamping it, and storing it. The Clock is a stable time source based on a chip scale atomic clock (CSAC). It will keep accurate time between updates from the relay satellite, necessary for correlating events between sensors for the seismic network mission. The supervisor computer is planned to be an ultra-low power MSP430 radiation tolerant microprocessor to manage the radio and switch power to the UA subsystem. To save power, the radio is off until the relay

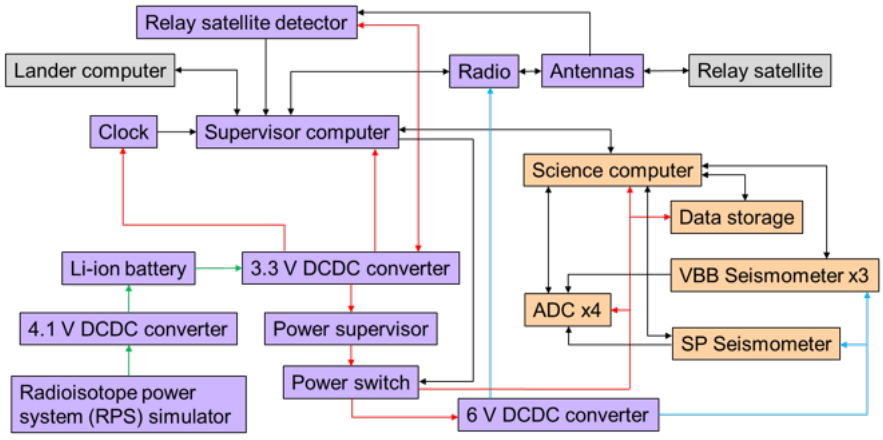

Figure 69. RIPLS power and data flow block diagram. Purple color is Aerospace design; Orange is seismometer; Grey is external mission infrastructure.

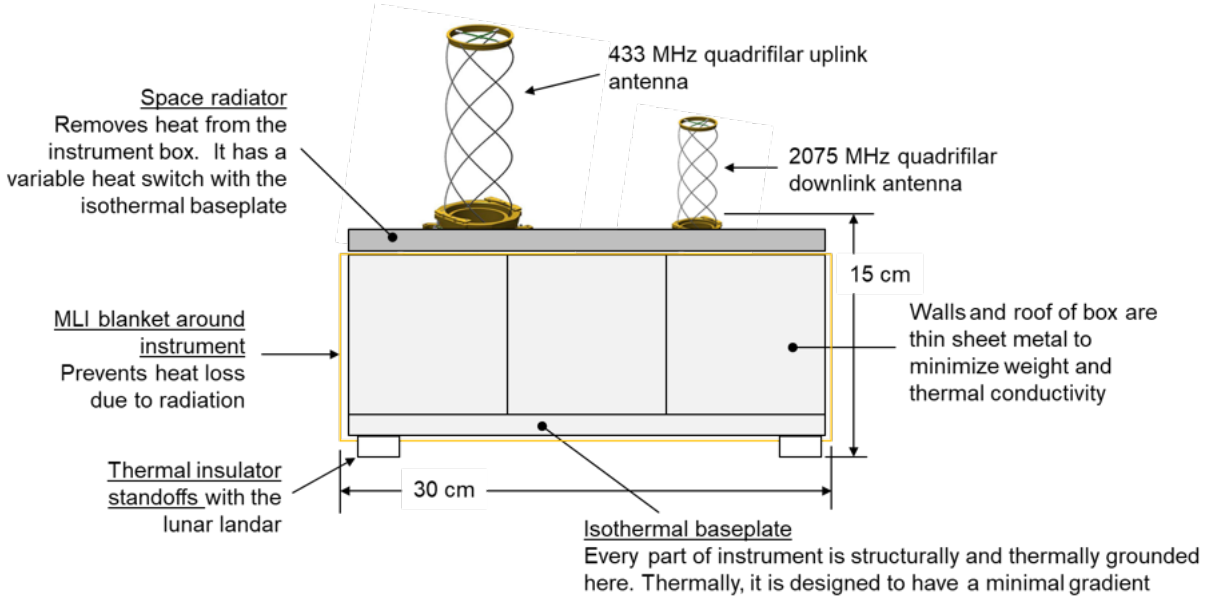

Figure 70. RIPLS DALI instrument with antennas deployed. For mission with the package mounted under the lander, the antennas and radiator would feed through the lander body for sky access.

satellite is detected by a narrow indicator tone, which will then wake the radio and start transferring science data from the data storage memory to the radio for transmission.

The RIPLS instrument packaging utilizes a pair of isothermal plates, one as the baseplate, 20 x 30 x 1 cm, (isothermal in construction and acts as the primary structure) to which the instrument is mounted and the other is a radiator, presently 20 x 30 x 0.5 cm, for emitting the heat from the instrument. The baseplate is connected to the lander through small thermal isolation standoffs. The radiator is the same area as the baseplate and are connected 12.5 cm above the thermally isolating standoffs. With RIPLS mounted to the lander, the radiator will be at the end of a thermal conduction path with a view of the sky. Quadrifilar antenna can be used to leverage their lack of pointing required for satellite overflight communication. The antennas are shown in their deployed state in Figure 70 mounted on the package, but for a mission the antennas would be mounted on the lander. The package box is enclosed in MLI with radiator access located above the MLI on the zenith face and the isolators that mount the instrument to the lander through the nadir face MLI. The total instrument mass is estimated at 10.5 kg.

The APPLE RPS generates 17 W_{th} constantly while producing 1.7 W_e. This is a benefit during the lunar night and a detriment during the lunar day. A thermal switch (a thermally conductive path passing up to 25 W_{th}) can be designed that can be adjusted in conductivity without holding power. In our proposed design, the RPS has its cold junction hard mounted to the baseplate, always warming it. The thermal switch opens and closes a heat path between the radiator and the baseplate to regulate the baseplate to within ± 10˚C of its desired setpoint.

The electronics would be laid out to fit on Aerospace's standard AeroCube 80 x 80 mm board hardware for heritage. It would have two distinct boards, one for the power elements and one for the supervisor computer. The radio will have a low power 433 MHz radio and will be connected to the quadrifilar 433MHz antenna. The electronics would fit within a 10 x 10 x10 cm volume on RIPLS. The APPLE RPS and thermal switch will fit into a similar volume adjacent. The seismic sensor subsystem will fit in an adjacent 20 x 20 x 12.5 cm. This leaves a final 10 x 10 x10 cm volume that was planned for a flight radio (such as a Space Micro μSDR-C™ or SDL Cadet).

The software on the RIPLS science computer will configure the seismic sensors and configure the ADCs. Once configured, it will start collecting data at a commanded cadence and store it in memory. The science computer can be signaled by the supervisor computer to either perform a task in parallel or to halt data collection when talking to the supervisor. The science computer can also signal the supervisor computer for housekeeping tasks such as the current time on the CSAC.

The software on the RIPLS supervisor computer will additionally collect telemetry on the instrument consisting of voltages and temperatures for state of health monitoring. The supervisor will be interrupted by either the Science computer or the Relay satellite detector. The later interruption halts collecting telemetry, turns on the radio, and interrupts the Science computer and asks it to interleave retrieving science data, staring from the latest bookmark, with the continued collection and storage of science data.

7.4 Small Mars and Beyond Spacecraft Powered by APPLE

The need for power at distant locations typically requires the use of RTGs, though missions as far as Jupiter (Juno) used solar power, at a high cost to mass and volume of the explorer. Currently these needs are met with the MMRTG heritage design, delivering ~100 W_e at 45 kg of mass. This large mass and relatively large power output then require missions that need RTG power to be fairly large, pushing the missions into the Flagship class of missions, with the attendant risk posture and cost. Not only do RTG powered spacecraft then cost several billion dollars, but the current production of ^{238}Pu by DOE for NASA's MMRTG is an amount (1.6 kg) creates a long wait list for MMRTG power, reducing the flow of deep space missions to a trickle. Using APPLE for deep space mission would reduce the amount of Pu needed (for Pu-APPLE), or create an alternate isotope pathway (for Am-APPLE). The small, scalable nature of APPLE also allows for smaller vehicles to be launched, or independent daughter craft from a mothership that can be MMRTG powered, or solar powered. Small and lightweight vehicles powered by APPLE can greatly expand the number of missions and more importantly, the number of destinations that are accessible.

To evaluate the potential and requirements for small spacecraft (<100 kg) using APPLE, the MarCO mission was used as a template for capability, power needs, and thermal conditions. The Mars destination of MarCO also serves as a worst case thermal

environment for a spacecraft using APPLE, as Mars represents the minimum distance from the sun where an RTG could be considered over solar power for a mission.

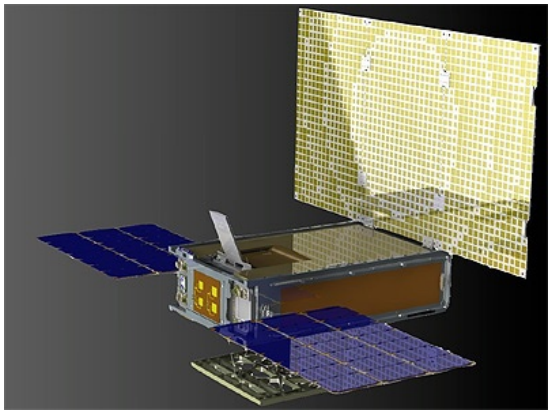

Figure 71. MarCO vehicle showing the two solar panels with 42 solar cells to provide 15 We. It also had a 35x60cm antenna.

MarCO mission was a pair of 6U small satellites sent to Mars to provide real-time communications to Earth for the InSight mission during its entry, descent, and landing. The vehicles had 15 W_e of solar photovoltaic power at their Mars destination. It had 42 solar cells designed to provide 15 W_e in Mars orbit from two solar panel wings. This will be taken for the power requirement for an APPLE powered design, and the 6U chassis (minus the solar wings) as the radiative surface for heat dissipation. MarCO vehicles also had a large (35 cm x 60 cm) antenna for UHF communication to InSight and X-band transmission to Earth as well as two solar wings. Assuming Mars location for thermal inputs. The design will be considered with and without the large antenna.

Assuming a 15,000 km Martian orbit, 0 degree beta andle, we modled a 6U (10 cm x 20 cm x 30 cm) chassis with six surfaces, as well as a 6U design that also used a 35 cm x 60 cm Al antenna. The simulate an APPLE powered design, the 2,200 cm^2 chassis surface area (6U only) is sufficient for 6 APPLE units using the 400 cm^2 requirment for surface emission. This uses the 2.1 W_e, 18 W_{th} version of APPLE. This would generate 12.6 W_e at Mars orbit, dispered with one unit on each of the 6 surfaces of the vehicle. This was modeled in thermal desktop as 18 W_{th} from each APPLE unit placed in the center of each 6U face. Entire vehicle surface is simulated as 2 mm thick aluminum material, surface emissivity of 0.92.

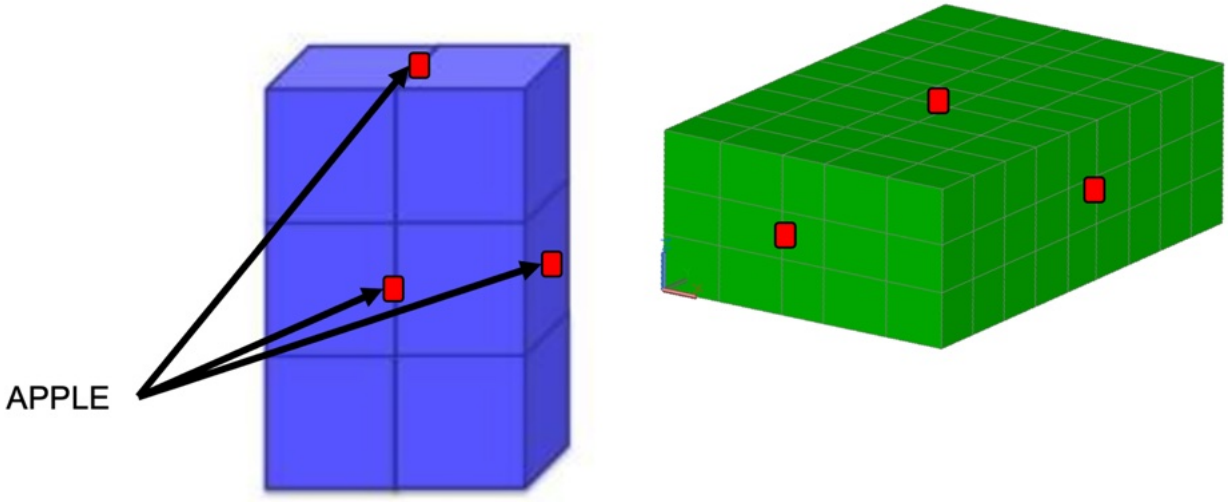

Figure 72. 6U spacecraft with 6 APPLE units, one on each face of the vehicle, to generate 12.6 W_e.

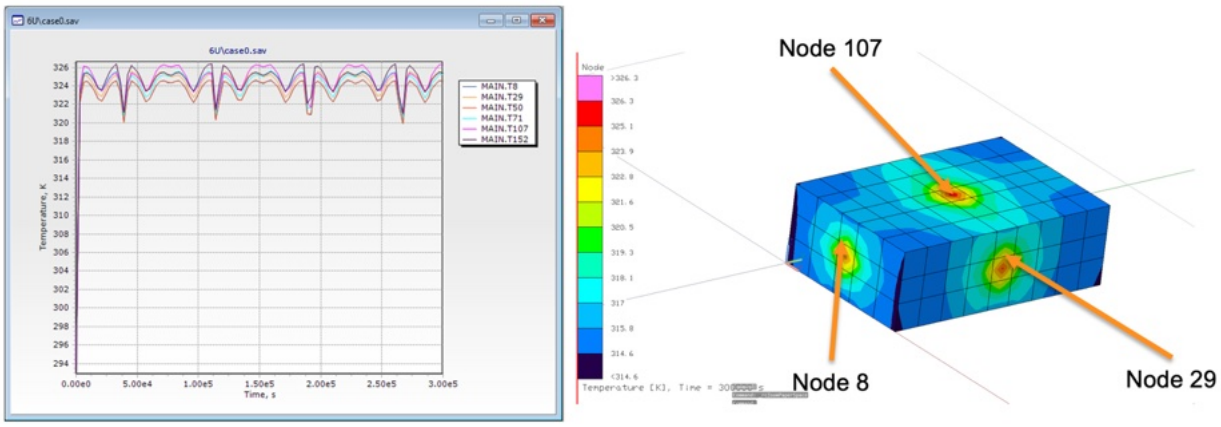

Figure 73. Thermal surface profiles of a 6U vehicle with 6 APPLE units. Surface temperatures ranged from 52˚C to 41˚C.

As seen in Figure 73, the vehicle surface ranges from 52 ˚C to 41˚C, a very reasonable temperature, with no additional radiators, but also obviating the needs for heaters for most components in addition to the removal of the solar panels and associated mechanisms (hinges, fold up capability, etc.). The 2,200 cm^2 of radiative surface area is 92% of the 'required' surface area for 6 units. As such, the cold shoe temperatures are slightly higher than the target temperature of 35˚C. This will raise the hot shoe temperature by about 16˚C. This increased hot shoe temperature may affect SKD longevity. But overall surface temperature ranges are compatible with most spacecraft components.

However, MarCO itself, and typically other vehicles are often not merely boxes, but have structures like MarCO's antenna or other components that will act as additional radiative surfaces that must be incorporated into the thermal design, and in this case, the APPLE thermal requirements. Simulating a MarCO structure using the attached 35x60 cm antenna, this additional radiative surface area allows for the addition of three more APPLE units, with three placed to use the antenna as a radiative surface. This additional radiative surface allows for matching of the MarCO power requirement (15

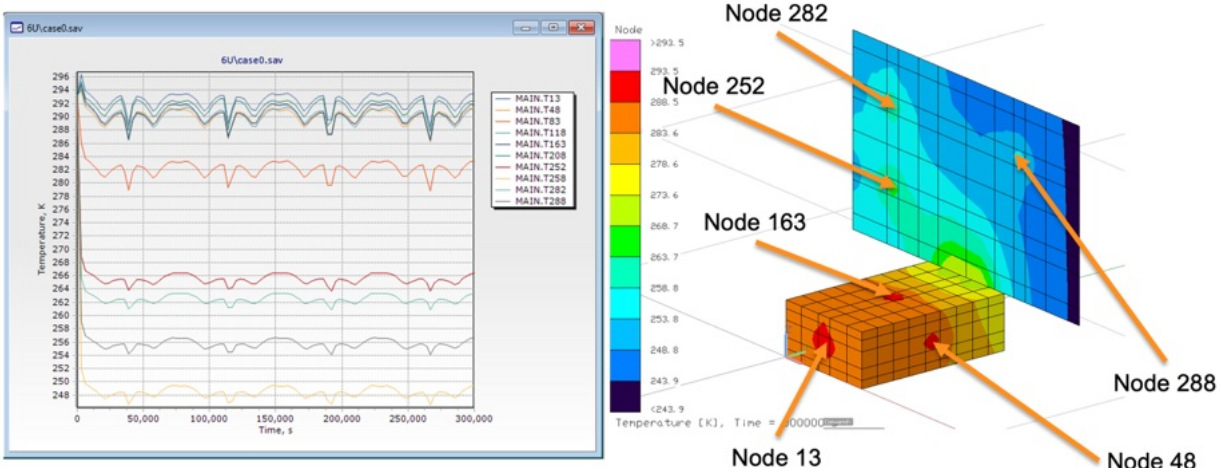

Figure 74. Simulating a 6U vehicle with a MarCO-like antenna surface. This model has 9 APPLE units distributed across the surface, and resulting in a temperature between 0-20˚C over the main chassis.

W_e) as well as bringing the chassis temperature to room temperature. This design does not include the additional radiative surface MarCO had for its solar wings, allowing for removal of the mass as well as deployment risk for those components. The Thermal Desktop simulation shows reasonable vehicle temperatures across the main chassis, between 20˚C at the cold shoe interfaces, down to 0˚C near the antenna junction. This first order thermal simulation can be altered by the actual structure of the vehicle, including heat pipes and specific thermal conduction properties, but does show that APPLE can supply power for missions comparable to what solar panels can supply for Mars location missions, but also delivers thermal control without the need for heaters at Mars and beyond.

The Martian solar input (538 W/m^2) for these simulations have a small effect on the surface temperature of the vehicle. It can be seen in Figure 73 and Figure 74, in the fluctuations in temperature as the vehicle passes through eclipses. To evaluate the thermal impacts of having no solar input, such as at a very distant location (i.e. Pluto's 0.9 W/m^2) or in long duration eclipses (ignoring planetshine), the equilibrium temperatures were simulated for a 0 W/m^2 mission. As shown in Figure 75, the average temperature drops ~5˚C, demonstrating little impact on vehicle surface temperature without solar input. From this, it can be seen that APPLE can be used at destinations from Mars to infinite solar distance without additional heaters for the vehicle.

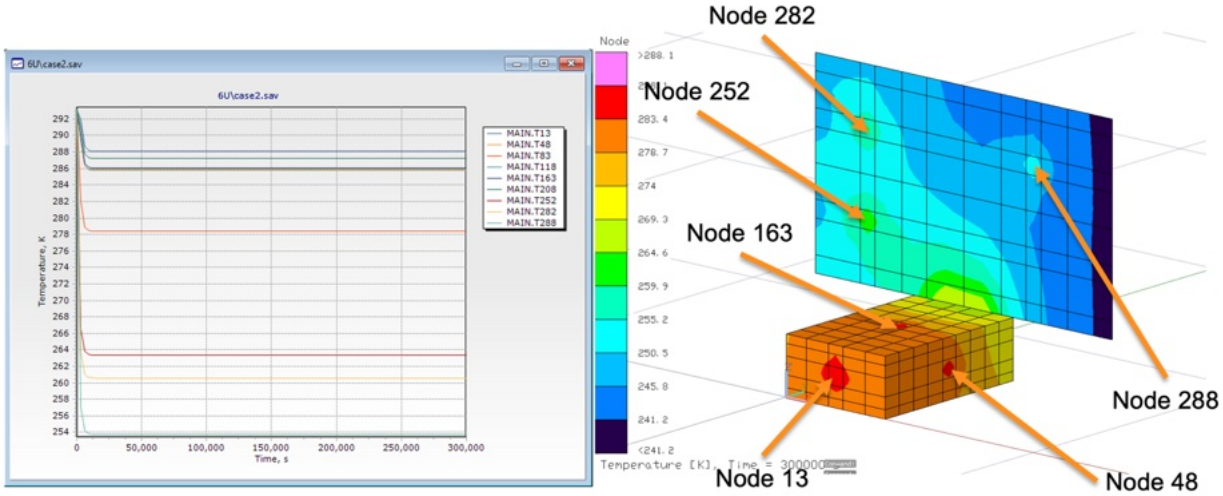

Figure 75. 6U vehicle with 9 APPLE units with no solar input, simulating distant mission destinations. The average temperature declines ~5˚C.

This Mars distance thermal simulation applies to Mars orbit vehicles but can be modified for more distant missions, with a range of achievable temperatures for the vehicle depending on overall thermal design. As shown here the magnitude of heat dissipation from the vehicle surface and the attendant cold shoe temperatures allows for tailoring the vehicle component temperature to not only typical electronics qualification temperatures of –34 to 71°C, but also to the most constraining vehicle component for temperature, the Li-ion battery, which typically requires a tight temperature range of 10˚C to 30˚C. This thermal design can be made without the need for a battery heater in space.

This exercise can also be performed for even small vehicles, with likewise smaller power requirements, suitable for daughter vehicles, sensors, or nodes from a mothership. A key benefit of APPLE is the delivery of RTG power for spacecraft remotes, and the single APPLE powered spacecraft could be deployed to collect data at a range of orbital locations for a collective mission. Considering a 1U vehicle, to leverage the small sat technology revolution over the last two decades, a single APPLE can power a 2W 1U vehicle for data collection and transmission to a mother ship. Figure 76 shows this vehicle, with a single APPLE on one face of the vehicle. The total surface area available (10 x 10 x 10 cm, 600 cm^2) is much greater than the required 400 cm^2 from the general thermal simulations, and because of this, the temperatures of the 1U surface range from 6-8˚C, outside of the hot shoe, which sits at 17˚C. The residual surface of the 1U can possibly also contain another APPLE unit, for twice the power, though with an increase in the hot shoe temperature.

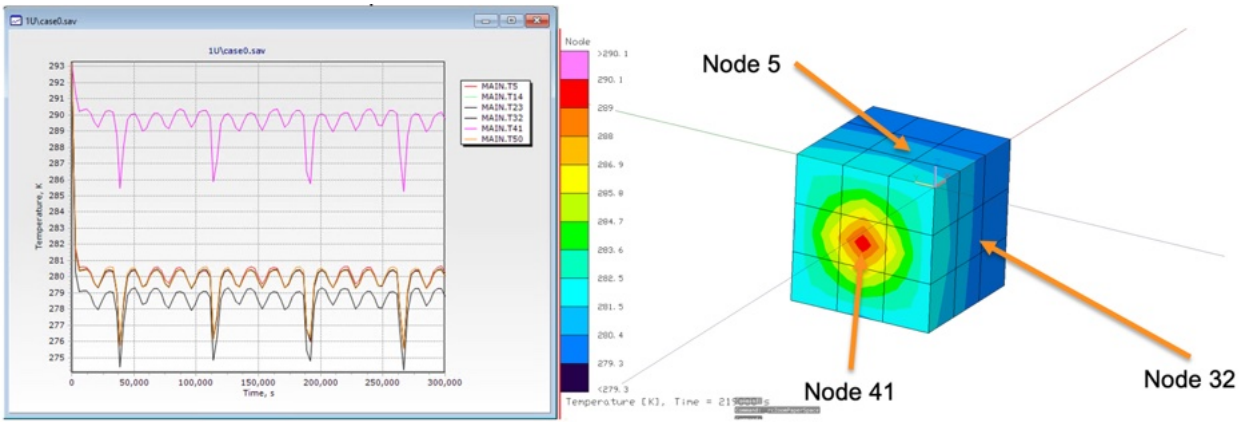

Figure 76. 1U, 1 APPLE vehicle or sensor node thermal profile, addressing a key issue with small vehicles, the thermal fluctuations of passing in and out of eclipse.

7.5 Solar Sail Mission Power Design

A low mass RTG power system technology opens up lightweight, rapid transit access to the solar system. The small mass and additional thermal supply from an APPLE RTG can allow for vehicles that need very low masses for fast transits, such as solar sails. Heritage RTG designs are too heavy for low thrust vehicles, limiting technologies like solar sails. Due to the stringent mass requirements for solar sails, they often are designed with limited capability for science payloads, especially compared to flagship spacecraft. To power a solar sail mission at its destination, APPLE can be used to displace thermal heating requirements, and supply power for instruments, and charge batteries for high peak power communications components, all while meeting the power and mass requirements. The Phase I design was used in a mission concept for the Solar Gravity Lens mission,[83] with APPLE being the key enabling technology for the mission, with the low power and heat provided closing the design space for vehicle operation.

Using the APPLE Phase II design, we performed an EPS design overview for the SCOPE team and demonstrated that APPLE could be the enabling technology for the mission. SCOPE, ScienceCraft for Outer Planet Exploration, is a NIAC program to develop a new architecture for science missions to the outer solar system at a low cost. It addresses all the major challenges of outer solar system, including high cost, long travel time, and narrow windows for mission implementation. The SCOPE design is scalable and low cost, allowing to fly a constellation of flybys for high coverage of a planetary target. SCOPE uses solar sails to carry a small avionics, comm, and payload package to deep space targets. SCOPE is a mission concept that integrates a science instrument and spacecraft into one monolithic structure. Utilizing a quantum dots printed on the solar sail to form a spectrometer SCOPE utilizes the mass, volume, and surface area of the solar sail for data collection in a rapidly travelling packing for missions across the solar system. Unlike solar sails that propel small cubesats, SCOPE uses this sail area for spectroscopy, lowing vehicle mass and increasing data collection capability. Several SCOPE vehicles working communally can deliver several very large area spectrometers to the Neptune-Triton system in just a few years and deliver considerable amounts of data, provided a power system exists that can fit the mission requirements.

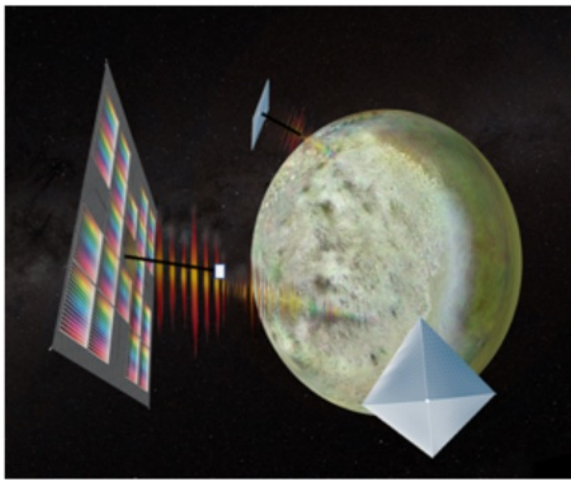

Figure 77. A constellation of four SCOPE vehicles providing global coverage of Triton with their large, sail based spectrometers.

An APPLE powered design could meet the power requirements for SCOPEs payload, avionics, and comm with 24 1.7W_e units. SCOPE requires 22 W peak power during data collection and transmission, setting the minimum bounds for the vehicle power

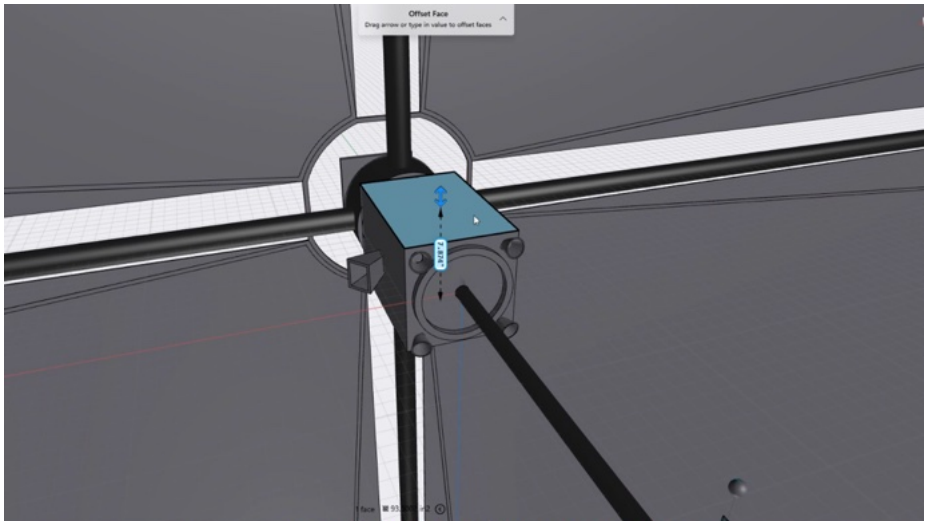

Figure 78. The SCOPE avionics compartment located at the center of the solar sail, requiring an RTG as distance from the sun and vehicle geometry prevent solar usage.

design. Using an assumption of power margin during this peak power operation of 40%, a mission performance time period of 8.7y after launch, 24 APPLE units would be needed, as seen in Table 6. Comparing the Pu-APPLE and Am-APPLE designs, the slower power decay from the longer half-life of the Am-APPLE has a small impact on the power requirements. Assuming an 85% power distribution efficiency and a 40% power margin to peak power, it can be calculated that 39 and 37 W of power are needed from the two designs respectively.

Table 6. Development of vehicle power requirements from CONOPS of 22 W peak power.

Unit parameters	Pu-238	Am-241
Isotope Mass (g)	31	161
Radiator X,Y dimensions (cm)	20	20
Radiator Area (cm2)	400	400
Tile Mass (g)	40	190
Tile Thickness (cm)	2.0	4.0
Power Out (W)	1.7	1.7
Power Conversion Eff. (%)	0.109	0.100
Mission Power System Needs		
Peak Power (W)	22	22
Power Distribution Efficiency	0.85	0.85
Isotope Remaining at 8.7y (%)	0.933	0.986
Power Margin at Peak Power (%)	0.4	0.4
Power System Size (W)	39	37

To make comparisons between the Pu-APPLE and Am-APPLE, as well as a conceptual solar power input, it can be seen that an RTG smaller than the MMRTG is the enabling technology for a solar sail mission to deep space. As seen in Table 7, to deliver the 40W post-margin required for the mission, 24 tiles are needed, resulting in a power system mass of 0.96 kg for Pu-APPLE and 4.56 kg for Am-APPLE (and a slightly larger 372,960 kg for a solar array). The Pu needed for this vehicle would only be 0.744 kg, less than half of the yearly production of new Pu-238 by the DOE for NASA. The Am needed, 4.56 kg would needed to be sourced from European production, or from a new domestic refinement program. Assuming a 40Wh battery for power system conditioning, as well as peak power operation for the comm system, APPLE enables delivery of data from the mission, in a mass package for the EPS of 1.9 kg for Pu-APPLE and 5.5 kg for Am-APPLE. The total radiative area required for the APPLE unit would be less than 1 m^2 (0.96m^2), easily accommodatable on the vehicle chassis, and allowing for integration of the APPLE units on the chassis preserving the thermal benefits of a room temperature, deep space vehicle.

Table 7. Power system design for a solar sail mission to Triton, comparing the mass of a Pu-APPLE and Am-APPLE with the theoretical solar panel system.

Power system (High Reliability)	Pu-238	Am-241	Solar
Power System Size (W)	40	40	40
Tiles/Cells	24	24	12432
Total Unit Mass (g)	960	4560	372,960
Isotope Needed (g)	744	3864	0
40 Wh Battery Mass (g)	200	200	200
40 W Power Distribution Board (g)	200	200	200
Harnessing (g)	500	500	500
Radiator/support Area (m^2)	0.96	0.96	81
Total System Mass (kg)	1.9	5.5	374

7.6 Uranus/Neptune Magnetosphere Study Fleet

A mission concept that was investigated was the Uranus/Neptune Magnetosphere Study Fleet. The science objective of the mission is to characterize the variation of the magnetosphere over an extended time period (years) and potentially understand the magnetosphere rotation for Uranus/Neptune. The mission concept requires 16 smallsats to deploy from a larger spacecraft to orbit the target destinations. The smallsats would be spin stabilized with no active attitude control (Figure 79). The RPS requirements of the mission are to have 1.7 W_e, with low mass and volume. The cruise would be projected to be 10-12 years with 1-5 year orbit. The instruments would need to be developed to meet the low power levels. This concept while clearly enabled by APPLE was also deemed to be too low TRL at this time.

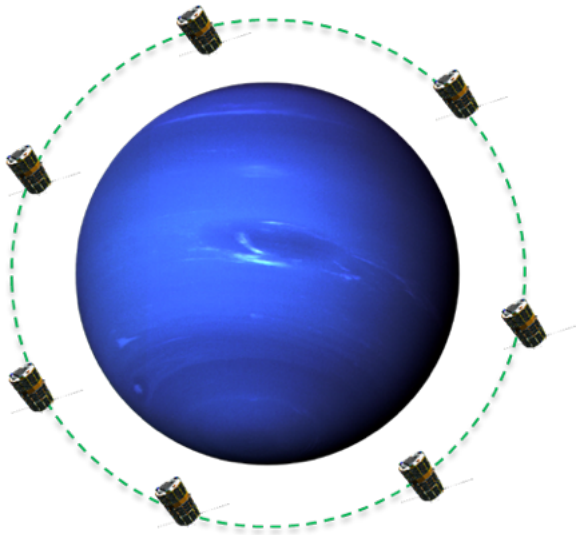

Figure 79. Uranus/Neptune Magnetosphere Study Fleet Concept, showing the arrangement of small satellites powered by single APPLE units.

7.7 APPLE Powered Ingenuity Follow On

APPLE can also open up exploration to moons and worlds where photovoltaic power is limited by the distance to the sun or through day/night cycles. A lightweight modular system would enable a wide range of rover designs, smaller and more capable than currently possible when using the large monolithic RTGs. Already MSL and Curiosity have chosen RTGs for power generation on Mars, even though other Mars exploratory missions such as Ingenuity, the small helicopter, have chosen a photovoltaic approach, likely due to the large size of the available RTG technologies. If APPLE was used for an Ingenuity-like follow on mission, it could efficiently replace the solar array + battery power system, while multiplying mission operation.

	Ingenuity	APPLE Match
Power units	1 5W solar array	1 1.7 W_e tile
Mass of Energy Gen + Energy storage	525g	400g
Energy per sol (Wh/sol)	40	40
Heater energy per sol (Wh)	20	0
Flights per sol	1	3*

Table 9. Comparison of Ingenuity power system to a Pu-APPLE system, demonstrating sufficient energy to perform three missions per daylight period. Am-APPLE would be 120g heavier, with the same energy generation.

The incident solar irradiation in the Martian northern hemisphere spring and summer is 2,000–5,000 Wh/m^2-sol,[84] and the 0.0544 m^2 fixed Sol Aero IMM4J array[85] during these seasons can then optimally generate between 24 Wh/sol and 60 Wh/sol. In addition, 21 Wh/sol of Ingenuity's power budget is to heat the vehicle and the six Sony VTC4 cells (42 Wh) during the Martian night.[86] One 90s flight uses about 10 Wh, which with the heater survival power means even in the peak of summer missions must be limited to less than one per sol. An APPLE power system could use a single APPLE unit to generate 1.7 W_e (40 W_e/sol), while generating sufficient waste heat (17 W) to eliminate heater requirements, in addition to allowing uniform operation regardless of time of day or season, as the power is independent of sun position. The Ingenuity power system (array + battery) weighs around 525g, and the APPLE unit would have a lower mass of 400g (for Pu-APPLE, or 500g for Am-APPLE). An APPLE powered Ingenuity successor using a single APPLE would be able to make at least 3 flights per daylight period, regardless of season or time. The limitation of the frequency of flight is not the total power available from the RTG, but rather the maximum discharge and charge rates of the batteries. Table 9 shows the mass and power comparison between the existing Ingenuity power system and a single APPLE unit, replacing the solar array with a Pu-APPLE RPS. This design would generate the same average power per sol, but since is it not required to sequester half of the generated power for overnight survival, would

	Ingenuity	APPLE 10x
Power units	1 5W solar array	2 1.7 W_e tiles
Mass of Energy Gen + Energy storage	525g	575g
Energy per sol (Wh/sol)	40	80
Heater energy per sol (Wh)	20	0
Flights per sol	1	10

Table 8. Two APPLE tiles would generate enough energy to run the vehicle continuously at 10 missions per day.

be capable of three missions per daylight period. Additionally, there is sufficient power for one or more additional flights, though night navigation will require a change to the navigation system. Figure 80. Battery state of charge for and APPLE powered Ingenuity follow on using a single 1.7 W APPLE unit. One APPLE delivers sufficient power for three flights per daylight period, regardless of season. Figure 80 shows the battery state of charge (SoC) for the flights, with a reserve capacity of 20%. The power system can supply sufficient peak power (400W_e for take off, 300 W_e for cruising) for the flights, with sufficient recharge periods between flights.

	AMH	APPLE Match
Power units	1 8W solar array	2 1.7 W_e tile
Mass of Energy Gen + Energy storage	1.7kg	1.6 kg
Energy per sol (Wh/sol)	60	80
Heater energy per sol (Wh)	20	0
Flights per sol	1	3*

Table 10. Comparing the Advanced Mars Helicopter design using solar arrays to a two APPLE powered design. APPLE enables 3x the number of flights per day, regardless of season.

To build a helicopter that would have 10x the daily flight capability as Ingenuity, only two APPLE units are required from the power requirements, and have only a modest increase in mass (50g). Two 1.7 W_e units would have a mass (Pu-APPLE plus battery) of 575g (Am-APPLE plus battery 675g), and have sufficient capability for 10 flights per sol. Table 8 shows the power system capabilities, using the same battery for a fair comparison. *Doubling the power generation enables 10x the number of flights, while retaining a similar SWAP profile.*

As shown in Table 10, this two APPLE design would be capable of 10 flights per sol, though CONOPS would need to be modified to enable the battery to charge sufficiently between missions. Since Li-ion batteries charge slower as they near 100% SoC, to minimize the time for recharge, the mission would have a peak SoC of 75% between flights. This limit minimizes charge time to 2.7h, increasing the number of flights per

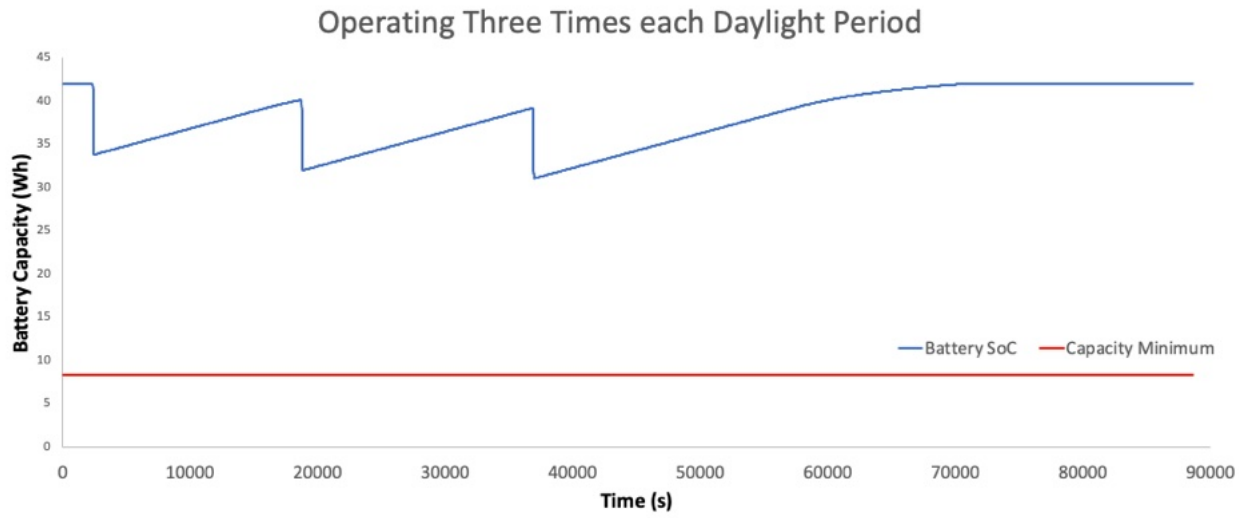

Figure 80. Battery state of charge for and APPLE powered Ingenuity follow on using a single 1.7 W APPLE unit. One APPLE delivers sufficient power for three flights per daylight period, regardless of season.

day. This lowered SoC during operations would not imperil the 20% SoC minimum for battery protection.

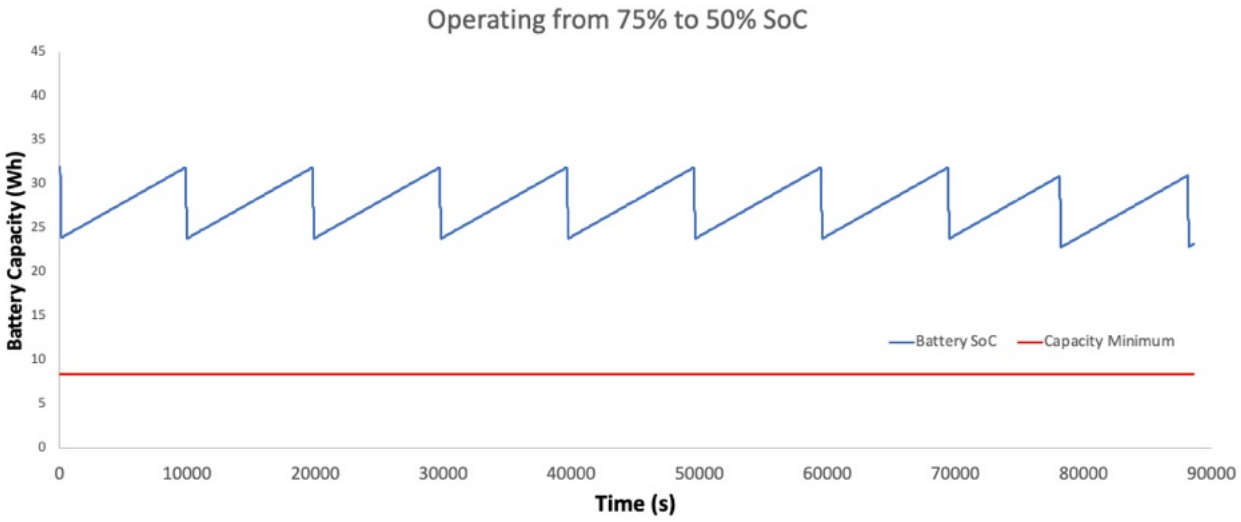

Figure 81. A two APPLE powered Mars helicopter design would be capable of 10 flights per day.

A more capable Ingenuity follow on design could increase the distance flown, and add payload capability. The Advanced Mars Helicopter, (AMH) design based on Withrow-Maser *et al. "An Advanced Mars Helicopter."*[87] Vehicle is based on Ingenuity hardware, using the same rotors, and with a larger battery and solar array. The AMH can operate for 2 minutes per flight (compared with 90s) with a range of 2 km. Critically, in addition to carrying the larger battery mass, it still has capacity to carry a 1.3 kg science payload, either a dedicated instrument, or carrying samples. The AMH design uses a larger 8W solar array and a 165 Wh battery. If APPLE was used for an AMH type design, it would enable missions more frequently than the existing solar power for less mass, and enable year-round operation. The design case shows using two 1.7 W_e tiles to power

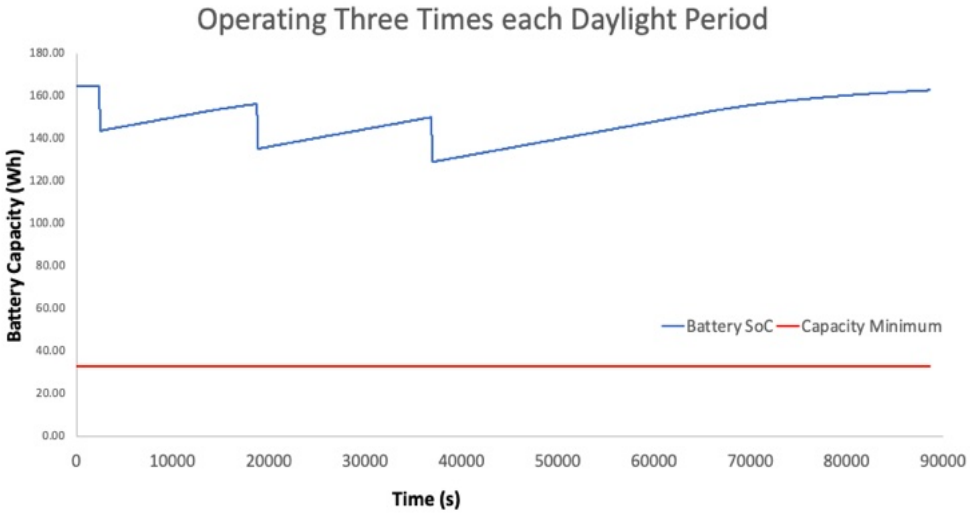

Figure 82. Battery SoC for an APPLE powered AMH design, showing sufficient power for at least three flights per daylight period, while carrying 1.3kg of payload.

the craft. The design also closes for only a single 1.7 W_e APPLE tile making two flights per day, matching the AMH output with half the power.

7.8 Mission Context Conclusions

The missions enabled by APPLE are extremely wide ranging, as the problem of power in non-solar locations forms the foundation of many missions to key locations for NASA missions, including the lunar surface, Martian surface, and deep space missions beyond Mars orbit. In many ways, power underlies the most fundamental mission design considerations, as all payloads and operations require power, and needs to be the first foundation stone laid in designing a vehicle.

In any location where fairly constant or predictable solar insolation is available, APPLE, or any RPS cannot compete against modern Li-ion batteries and high efficiency GaAs family multijunction solar cells. The relatively low cost, high reliability, commercial and NASA heritage for these power components leave them as far superior to any RPS type solution where ever possible. For locations such as Saturn and beyond, or the lunar surface, RPS technology performance far exceeds that of solar and is only limited the two most critical elements holding back RPS missions: isotope supply and launch, as the dearth of RPS designs to fit in different missions. It is only at the junction between solar/RPS needs that the most interesting cases arise; the competing applications of Martian surface operations, with the somewhat reduced solar incidence and reasonable day/night cycle, the space vehicles to the asteroid belt and Jovian orbit. It is these locations that APPLE may prove of the most benefit, as the modular design and option for smaller, lighter, and more efficient power may unlock additional missions that cannot be developed in the current RPS technology environment.

8. APPLE Development Path

8.1. Isotope Supply

8.1.1 Plutionium-238

Of the candidate RTG isotopes either considered or used in previous applications, ^{238}Pu has the lowest shielding requirements due to its production of primarily alpha particles, with stopping lengths in common spacecraft materials like aluminum and carbon in the 10 μm range, thinner the housing components of any component that may be radiation sensitive, much less the typical heavy metal isotope cladding, materials like Ir or Pt. Further the vast majority of this alpha emission is captured within the isotope material itself. Shielding for ^{238}Pu materials is mostly physical in nature, to prevent particles of material from flaking or powdering off and leaving environmental contamination. In addition, the 87.7 year half-life means that for even long missions EOL power levels have not diminished much from BOL. Actually, power losses for Pu RTGs are dominated by loss of thermoelectric conversion efficiency rather than isotope loss, typically through reduction in the efficiency of heat transfer at the hot shoe junction through sublimation of the thermoelectric materials.[88]

DOE entered into an agreement with NASA to restart ^{238}Pu production in 2013.[89] This production, occurring at Oak Ridge National Labs, supplied some of the ^{238}Pu used in the Mars 2020 mission, the first Pu RTG mission since the MSL, and using the last of the existing ^{238}Pu stockpile. Oak Ridge began new production in 2015, and has been increasing its ^{238}Pu production, with a goal to produce 1.5 kilograms of ^{238}Pu per year by 2026.[90] ^{238}Pu is produced at ORNL from neptunium-237 which is irradiated in ORNL's High Flux Isotope Reactor (HFIR), transmuting the neptunium into ^{238}Pu. The ^{238}Pu is purified from the neptunium and converted to an oxide powder for RTG use. Currently, HFIR can irradiate up to 6,800 grams of ^{237}Np every two to three months. Oak Ridge is currently building additional facilities to increase production to meet their 1.5 kg/y production targets. This 1.5 kg/y target when achieved can enable APPLE powered missions to deliver ~70 W_e per year in mission power, enough to launch one small APPLE-Pu RTG mission each year, or one large (>300 W_e) mission about every 5 years. Increasing these production targets through expansion of the fabrication facilities may open up many more missions, though it is likely that the motivation for this expansion will need to be driven by new mission designs, such as those enabled by APPLE. NASA's Office of the Inspector General issued a report warning of the difficulties of meeting the 1.5 kg/y target, and cast doubt on the possibility of increasing production beyond this rate, putting a ceiling on the number of MMRTG powered future missions.[91]

In addition, DoD interest in *cis*-lunar applications using non-solar power has increased in recent years, including the use of ^{238}Pu and other isotopes for heat and power generation.[92] This interest may lead to additional investment in isotope production beyond what has already been arranged. DoD production and current Pu supply is not openly known.

8.1.2 Americium-241

Europe has been focusing on alternative isotopes to ^{238}Pu, and have selected ^{241}Am as the isotope they would focus on for future radioisotope-based power systems. Americium oxide fuel can be refined from their stockpiles of nuclear waste through a chemical separation method developed by the UK's National Nuclear Laboratory. In this process, reactor fuel waste can be processed to extract the remaining Pu. ^{241}Am is formed from the beta decay of ^{241}Pu with a half-life of 14 years. This processing leads to a continual production of ^{241}Am from the continued decay of ^{241}Pu, and represents a long term supply chain for ^{241}Am RTG supplies, as the amount of available reactor waste is quite large compared to the RTG Am needs, and continually produces more Am over time. The production of the fuel is led by the UK's National Nuclear Laboratory and the University of Leicester. Processing of the ^{241}Am into a fuel oxide produces AmO_2 powders. This powder can then be sintered into fuel masses to form a clad. The temperatures of the sintering process tends to convert the cubic crystal structure of the AmO_2 to a bcc hexagonal form through oxygen loss, producing Am_2O_3, increasing the isotope mass fraction from 88.3% to 90.9% ^{241}Am and the density from 11.68 g/cm^3 to 11.77 g/cm^3.

In addition, the high temperature of the isotope after cladding leads the AmO_2 to undergo oxygen loss as well converting the AmO_2 to Am_2O_3, as well as generating oxygen that can accumulate in the clad as a gas and generate internal pressure. The clad design, similar to existing ^{238}Pu designs must then have a pressure relief mechanism to prevent gas pressure build up. Both ^{241}Am and ^{238}Pu produce alpha particles from their decay, which are essentially helium nuclei, which in their reaction with the materials of the clad produce helium gas. An example of a relief mechanism for an isotope clad, the clad itself can be formed to prevent internal gas overpressure through the formation of sintered Pt section of the clad.[93] By using Pt particles to form a frit for the clad, only gasses can be allowed to escape. A Pt frit over a vent hole in the continuous cladding material can serve to both block alpha radiation as well as migration of Am_2O_3 particles or powder out of the clad if the frit mean free path and particle size and packing are sufficient to stop the migration of particles while allowing He and O_2 gasses to freely migrate. Current production of ^{241}Am is estimated at 1 kg/y from commercial sources in its uses in smoke detectors, moisture detectors, and terrestrial RTGs.[94] This can be more easily increased through the processing of reactor waste than ^{238}Pu production.

8.2. APPLE Thermal Core Framework

At the center of the APPLE design is the isotope core, the radioisotope heart of each APPLE unit, consisting of a 1.7 x 1.7 x 1 cm $^{238}PuO_2$ tile encapsulated in a Pt cladding, or an 2.1 x 2.1 x 3 cm $^{241}Am_2O_3$ block encapsulated in a Pt clad. While the Pu-238 clad requires less Pt ionizing radiation shielding as seen above that the Am-241 core, in both cases the thickness of the Pt material is limited more by the mechanical needs of the clad and the Pt machining. In the APPLE design, both cores have a 1 mm thick Pt cladding to allow for ease of machining of the Pt as well as mechanical stability. These heat sources generate 16.8 W_{th}, allowing for a flexible design of the APPLE architecture

that scales by adding multiple APPLE units to supply the mission power needs. Currently, NASA uses the General Purpose Heat Source (GPHS), a $^{238}PuO_2$ bolus clad in iridium which measures 9.95 cm wide by 9.32 cm deep by 5.82 cm high and weighs 1.44 kg and provides 250 W_{th} at beginning of life. This was the heart of the GPHS-RTG system that powered Ulysses, Galileo, Cassini, and New Horizons, and is used in the MMRTG for Curiosity and Perseverance. However, the large mass and high heat flux of this heat source means that smaller spacecraft would be unable to use an RTG based on this thermal core. In the example of a 6U cubesat sized vehicle such as MarCO that uses about 17 W_e at Mars would be unable to use a power system based on even a single GPHS. In addition, with the current target of 1.5 kg of ^{238}Pu produced per year, this would allow for only a single GPHS produced per year. The larger flagship missions that used the GPHS in the past typically used up to 18 GPHS per vehicle (8 in MMRTG, 18 in GPHS-RTG), limiting flagship missions to one every decade or two. As the future of outer solar system exploration expands, more designs for small craft will need more flexibility in their power system design, and consequently a smaller thermal core. The APPLE Power Core generating 16.8 W_{th} can be incorporated into this design to allow for small craft to access RTG power, but also enable more frequent launches of missions past Mars with the current planned supply of ^{238}Pu.

In addition, the APPLE Power Core design can be the framework for future RTG missions, even outside of the APPLE. With regular production of this component, further designs can be made to incorporate it as a power or heat source, opening up vehicle design far beyond what can be done with the existing monolithic RTGs. The APPLE isotope core can also be used a as radioisotope heater unit (RHU) for missions to the lunar or Martian surfaces, or for space missions that need local production of heat for particular sensors or payloads. While there is an existing supply of Pu-238 RHUs for these applications, the expected explosion in lunar activity and missions in the next decade will put a heavy pressure on these supplies, as well as the production of new Pu-238. Diverting any of the new Pu-238 production away from use in the MMRTG powered missions would reduce the already low mission rate for these (one every ten years) missions. While APPLE-Pu missions would also impact this MMRTG mission rate, APPLE-Am would deconflict these missions, as well as adding additional production demand on Am-241 materials. Through the addition of another need for Am-241 clads, the production chain can be expanded, as even without APPLE as a final technology, the Am-241 RHUs can justify investment in accelerated Am-241 production.

8.3. Phase III Project Plan

8.3.1 Phase III Overview

Phase III would be a collaboration lead by the Aerospace Corporation FFRDC's Engineering and Technology Group (Aerospace), Jet Propulsion Laboratory's Thermal Energy Conversion Materials group (JPL), Aerojet Rocketdyne, an L3 Harris Company's Advanced Power Systems Group (AR), and Notre Dame's Civil and Environmental Engineering and Earth Sciences Department (ND). The Phase III study will focus on placing the APPLE RPS power architecture in the mission context of a lunar seismic

network, as the enabling component for a long duration lunar mission, as well as producing a system level design and producibility road map. Developing this power architecture will enable small scale radioisotope powered missions, breaking the previous RPS context from large flagship missions and providing a power capability to missions that most critically need RPS both for power as well as for heat. The history of lunar missions clearly indicates the need for RPS for operations far exceeding one lunar day,[95] and the Phase III APPLE powered lunar seismic network will lay out the benefits, as well as the development pathway to APPLE powered missions for other lunar missions as well as powering spacecraft. The main thrusts in Phase III will be a) developing an APPLE RPS lunar mission and its development roadmap, including a scalable long duration seismic network; b) establish the Phase III APPLE RPS design, including the thermal design, thermoelectric configuration, and system flow ups for integration; c) fabrication of the full component level/subsystem level skutterudite thermoelectric array, with thermal insulation and hot and cold shoe integration; d) demonstration of power output of the full stack, using thermal simulators based on Pu-238 and Am-241 clads; and e) performing a manufacturability and supply chain study, including developing a collaboration with U. Leicester for the Am isotope supply chain.

8.3.2 Phase III Design

Phase III will build on the existing Phase II APPLE design, the two-junction design, for the next generation of APPLE design, which in Phase III which will use an 8-junction system to increase both voltage output and efficiency, while also improving manufacturability. To this end, a new system-level thermal design and analysis will be performed for the RPS using both Pu-238 and Am-241 as heat sources. Previous work under this NIAC performed an evaluation of the available isotopes for APPLE, including Pu-238, Am-241, and Sr-90. The higher thermal output by mass for Pu-238 and Sr-90 disfavors Am-241, however, this mass advantage was offset by the additional required radiation shielding mass of the Sr-90. Am-241 was baselined as the secondary isotope option after Pu-238, needed due to the limited supply of Pu-238. APPLE in Phase III will be designed as isotope agnostic between Pu and Am, as the shielding requirements are similar, allowing APPLE to access new avenues for isotope supply.

8.3.3 Phase III Thermal Design

The design task would be joint between Aerospace and AR to develop the APPLE RPS unit design for integration into the mission design for the lunar seismic network in both the Mini and Max power configurations. The APPLE NIAC team will build a system level thermal and power models for the APPLE RPS system, including Am-241 and Pu-238 isotope clads, insulation, SKD thermoelectric legs, and system thermal outputs to transport vehicle. The thermoelectric thermal designs will use the analysis codes Thermal DeskTop, SINDA/FLUINT, and the Thermal Synthesizer System (TSS) to generate an optimum thermal-electric performance design. The model developed to optimize the designs will include all the materials, parametrics on geometry, radioisotopes, temperature, heat input, and environmental boundary conditions as well as performance at beginning and end of life. For the system level design, we will be

performing steady state thermal analysis using ANSYS software, and use PTC Treo software for system design. The analysis will take into consideration a) the system level thermal environment, b) the full system packaging of the unit, and c) manufacturability for follow on development and flight missions. The RPS Phase III design development in addition will formulate power electronics design and system packaging processes. These thermal designs will be performed for both the lunar mid latitudes and lunar poles with their differing thermal environments and consequent power impacts. Electronics design will cover power conversion from thermoelectric junctions to system bus power, including voltage regulation, voltage conversion, and including models for conversion and resistive losses.

8.3.4 Phase III Thermoelectric Stack Fabrication

Phase III would continue to leverage prior knowledge, production, and maturity of skutterudite TE materials and devices that were developed for advanced RTGs (eMMRTG) by NASA's Radioisotope Power Systems (RPS) program office and previously developed for DARPA.[96] Currently the SKD technology being developed is at TRL 4. The Skutterudite TE materials and devices have excellent stability and relatively low degradation rates with projections at the end of 17 year design life, ideal for long range/long duration missions.[97] The significant amount of lifetime data accrued by the JPL will be utilized to model the mission lifetime performance for baselined mission concept. These models will feed into the power simulations for the mission Ops as well as the risk matrix.

In order to meet a 2 W_e APPLE design target, TE multicouple modules will be designed and fabricated at JPL. Using JPL's existing technology[98] demonstrated in Phase II for SKD formation, sets of p-type and n-type SKD ceramics will be synthesized and diced for TE leg formation. Multi-junctions will be formed with 8 n-type and 8-p type legs for an 8 leg TE array. The team will characterize the TE transport properties using custom and commercial characterization equipment at JPL for TE materials and of the final devices.

After characterization these junction arrays will be encapsulated in an aerogel matrix thermally isolating the SKD materials and the hot and cold shoe exteriors. This thermal insulation prevents heat losses from the thermoelectric array, as well as suppressing sublimation of the SKD materials. The sublimation suppression is critical for life extension of the TE at the hot shoe temperatures. The assembled devices will be tested in the temperature range of interest (hot shoe 400-600˚C, cold shoe 0-40˚C) and under high vacuum to validate the performance at the beginning of life (BOL), and thermoelectric performance compared to previous JPL degradation studies for end of life (EOL) performance calculation. Extended testing of one module will also be conducted for reference and validation of fabrication and quality control[99] prior to delivery to Aerospace for stack assembly and testing. The JPL fabricated modules will be then utilized by Aerospace and tested as part of the full device.

8.3.5 Phase III Thermoelectric Stack Testing

In the NIAC Phase II effort, we demonstrated the operation of a thermoelectric generator (TEG) based on skutterudite junctions fabricated at JPL for this effort. We measured the response of the TEG to applied temperature differentials (ΔT) of up to 455 K (519˚C hot side) and demonstrated power generation from the device. The Phase II experimental results give confidence that a larger TEG array, coupled with an isotope thermal load and a seismometer payload could serve the needs of the lunar scientific community by heating and powering long duration lunar missions. he Phase III experiments are meant to develop the next step in the APPLE design, improving the design thermal and electrical efficiency, and enabling a tech-transition program to commercial companies and NASA mission directorates by increasing the TRL.

The design, modeling, and fabrication of the Phase III TEG unit will produce 2 W_e from 20 W_{th}. Phase III will produce 2 packaged APPLE thermoelectric units to be tested in a vacuum chamber with each unit package including insulation, bus wiring, and test leads along with a thermal simulator that mimics the isotope clade in dimensions, volume, and thermal output. The vacuum testing with the packaged, insulated TEG units will be used to verify the thermal modeling parameters including those for the lunar surface environment. Using the fabricated TEG units with the thermal simulator we would do the following experiments: 1) In a vacuum chamber and as a function of applied differential temperature, we will measure the output voltage and current (open circuit and with load), 2) measure the temperature at design points that show heat conduction, “recovery” from the thermal simulator to ensure the cold side temperature remains within specifications (lunar surface temperatures can plummet to -246˚C). 3) We will procure a miniature COTS vibration sensor, in lieu of the mission seismometer, which is deemed to be too costly for this project, and power it with the APPLE package and conduct a vibration experiment. This demonstration, to first order, will show the feasibility of our proposed concept and to lay the foundation for tech-transition to NASA mission directorates and commercial companies. Finally, using the experimental results we will design a package that integrates APPLE, a mission seismometer, and COMM system into a single unit.

8.3.6 Phase III Mission Design

System design efforts will focus first on power conditioning and control from the APPLE RPS. The expected output voltage of the thermoelectrics will be in the 500-600 mV range, and will need to be boosted to a design bus voltage (e.g., 5V, 12V). Low power boost converter electronics (e.g., TI BQ25504) will be specified for power regulation, and this design interface will allow APPLE to fit into any common bus design regardless of bus voltage through use of boost converter electronics. Typical efficiencies for these electronics are in the 90+% range and can be tailored to meet mission requirements. The bus design will also include a battery for high power operation for the COMM unit to support the Lunar Seismic Network units, and the battery will also serve to condition the bus power, and support mission burst power requirements for high power payloads or operations. Mission power simulation studies for the APPLE Lunar Seismic Network mission will demonstrate the frequency of data download events and develop a power budget based on the APPLE power delivery as well as payload location, data collection

rates, and potential preanalysis or conditioning of data. The APPLE System design will have a common power interface for missions, including output voltage, peak power, load limits, and ripple precision. The design will also encompass structural elements designed for thermoelectric stack compression and thermal contact, as well as packaging, with insulation, to protect components for environmental testing, and to ensure good thermal contact of the TE stack, isotope clad, and radiator interface. With the design completed, we will initiate a study describing tech needs for the manufacture of the APPLE RPS, including thermoelectric manufacture bottlenecks and alternatives, isotope supply chain, and a first order manufacturing cost analysis and methodology/procedures. The production assessment will include potential steps for manufacturing the individual components at scale for flight assets, including thermoelectric materials manufacturing, insolation production, prospective isotope handling requirements and hazards, isotope supply chain risks, and cost assessment. This study will be developed with the results to lay the foundation for the post NIAC-tech transition to tech demo missions and commercial production.

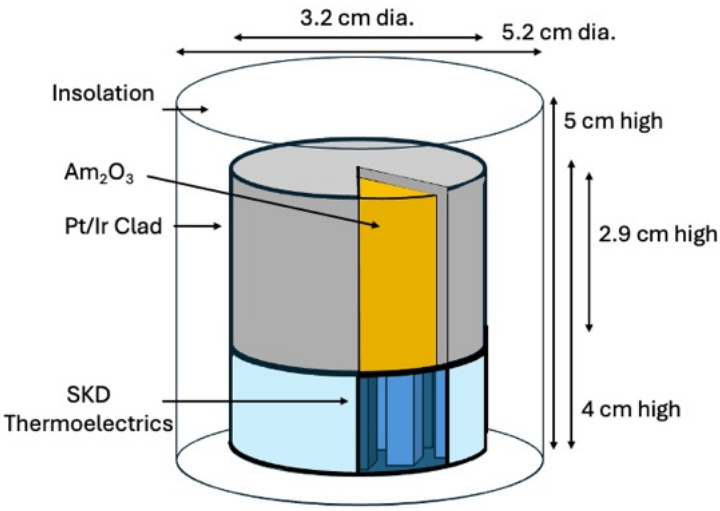

Figure 83. Diagram of the APPLE small RPS unit. The ^{241}Am isotope is clad in Pt-Ir, sitting on the skutterudite thermoelectric array, and encapsulated in aerogel for insulation.

9. Technology Roadmap and Transition

APPLE Phase III designs will exit with a complete range of thermal simulations, thermoelectric fabrication and assembly procedures, testing, and commercial connection with AR, the commercial company that delivered the RTG power for the Mars Curiosity and Mars Perseverance Rovers, as well as for the upcoming RTG powered DragonFly mission to Saturn's Moon Titan.[100] The final desired intent of a commercial partnership with AR is capability for productization of APPLE for NASA and commercial missions. The manufacturability study developed under Phase III will serve as the manufacturing roadmap for follow on mission proposals, as well as outlining the path to the required isotope supply for flight missions and regulatory approval process for an isotope containing launch.

Our work developing a small, modular RPS has generated considerable interest in the space technical community. The need for new mission designs that are enabled by providing power beyond our solar system's photovoltaic boundary (~2 AU) has already generated several collaborations and opened pathways for further development. In Phase I, we worked with the Solar Gravity Lens team (NIAC project selected for Phase I, II and III) to deliver a power system design that enabled reaching mission milestones at 500+ AU.[101] In Phase II, we worked with the ScienceCraft for Outer Planet Exploration (SCOPE)[102] team from NASA GSFC to design a power system to enable their fast transit solar sail mission to ice giants. In Phase III, our team will be working with the team behind the Lunar Geophysical Network[103] to develop our RTG powered lunar seismic mission. Each of these missions represent key archetypes for RTG powered missions: lunar and planetary missions, outer solar system exploration, and extreme extra solar missions.

In Phase III, we are working with AR and JPL for system integration and packaging for a commercial product, developing the manufacturing collaboration that would underly follow-on APPLE missions. In addition, this production collaboration is developing a collaboration with University of Leicester for a "pipeline" for Am-241 clads for use in APPLE production for future missions, the first practical pathway for Am-241 NASA missions. The TRL 5+ technology at the end of Phase III will enter into the robust NASA pathway for technology development and flight hardware delivery and a potential pathway for isotope fuels for NASAs RPS powered missions.

As shown in the Tech Roadmap, (Figure 84), APPLE Phase III will exit at a TRL 5+, and will target mission technology development programs such as Technology Demonstration Missions (TDM), or a combination Small Spacecraft Technology Program with the Flight Opportunities Program. In this follow-on phase, we will be developing a collaboration with University of Arizona and Silicon Audio to develop the lunar seismic sensor to enable the APPLE Powered Seismic Lunar Network. In addition, we will initiate closer collaborations with Prof. Richard Ambrosi at University of Leicester for the delivery of an Am-241 clad to produce a fully functional RPS-seismic sensor package. Alternatively, direct partnerships with mission concepts (P-star) or instrument development programs (i.e. DALI) could also be pathways to mature the technology for

a given mission. This high level Tech demonstration will position us to participate in the Artemis program in the 2030 timeframe, enabling deployment of an APPLE powered lunar seismic mission in the 2030s.

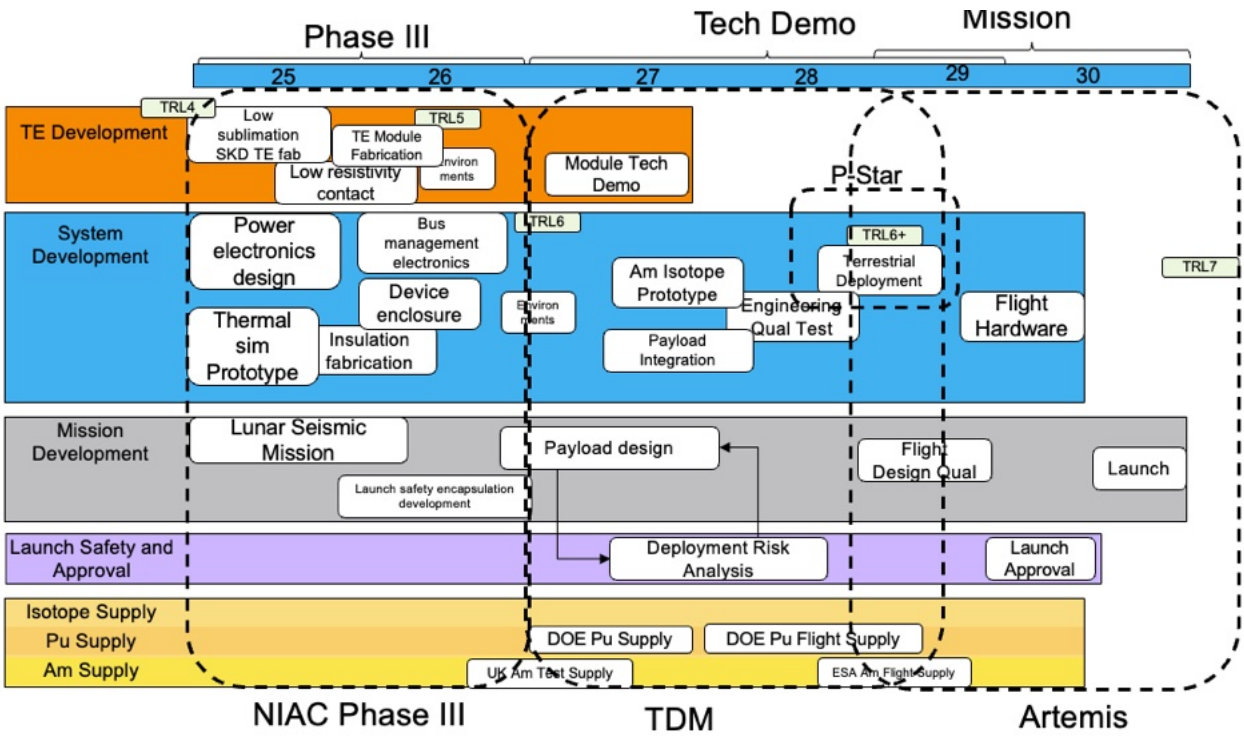

Figure 84. Tech Road Map for APPLE deployment. APPLE will move through Phase III delivering a TRL 5+ technology, ready for mission payload development under TDM. Successful deployment of the APPLE powered seismic sensor with a collaboration with U. Leicester for Am fuel will be demonstrated under a terrestrial mission, before transitioning to a CLPS or Artemis mission.

New Technology Report

The following technologies were developed under this NIAC Phase II study:

N/A

10. References

[1] Landis, G. A., Fincannon, J., "Study of Power Options for Jupiter and Outer Planet Missions," *42nd IEEE Photovoltaic Specialists Conference*, New Orleans, LA, June 14-19, 2015.

[2] https://spacenews.com/plutonium-availability-constrains-plans-for-future-planetary-missions/

[3]MacDonald, Wm., Hughes, G. W., McInnes, C., Lyngiv, A., Falkner, P., Atzei, A., "GeoSail: An Elegant Solar Sail Demonstration Mission," *Journal of Spacecraft and Rockets*, 44, (2007).

[4] Manzella, D., "Low Cost Electric Propulsion Thruster for Deep Space Robotic Missions," 2007 NASA Science Technology Conference, 2007.

[5] Cataldo, R. L., Bennett, G. L., "U.S. Space Radioisotope Power Systems and Applications: Past, Present, and Future," NASA Glenn Research Center (2009).

[6] Li, H. "Practical Evaluation of Li-Ion Batteries," *Joule*, 3, (2019) pp. 911-914.

[7] Miller, T. B. "Battery Applications for NASA's Missions - A Historical Perspective," *ARPA-E Robust Affordable Next Generation EV-Storage,* NASA KSC, January 28-29, 2014.

[8] Zhang, S.S., Xu, K., Jow, T.R., "The low temperature performance of Li-ion batteries," *Journal of Power Sources*, 115, (2003) pp. 137-140.

[9] Hamon, Y., Douard, A., Sabary, F., Marcel, C., Vinatier, P., Pecquenard, B., Levasseur, A., "Influence of sputtering conditions on ionic conductivity of LiPON thin films," *Solid-state Ionics*, 177, 2006, pp. 257-261.

[10] J. Fu, "Fast Li+ ion conducting glass-ceramics in the system Li2O–Al2O3–GeO2–P2O5," *Solid-state Ionics*, 104 (1997), pp. 191-194.

[11] Thangadurai, V., Weppner, W., "Li6ALa2Ta2O12 (A = Sr, Ba): Novel Garnet-Like Oxides for Fast Lithium Ion Conduction," *Adv. Funct. Mater.*, 15 (2005), pp. 107-112.

[12] Y. Inaguma, C. Liquan, M. Itoh, T. Nakamura, T. Uchida, H. Ikuta, M. Wakihara, "High ionic conductivity in lithium lanthanum titanate," *Solid-state Commun*., 86, (1993), pp. 689-693.

[13] Kuwano, J., West, A. R., "New Li+ ion conductors in the system, Li4GeO4-Li3VO4," *Mater. Res. Bull*., 15 (1980), pp. 1661-1667.

[14] Kanno, R., Murayama, M., "Lithium Ionic Conductor Thio-LISICON: The Li2 S - GeS2 - P 2 S 5 System," *J. Electrochem. Soc*., 148 (2001), pp. A742-A746.

[15] Plichta, E. J., Henrickson, M., Thompson, R., Au, G., Behl, W. K., Smart, M. C., Ratnakumar, B. V., Suampudi, S., "Development of low temperature Li-ion electrolytes for NASA and DoD applications." *Journal of power sources* 94.2 (2001), pp. 160-162.

[16] Li, D., Ma, Z., Xu, J., Li, Y., Xie, K., "High temperature property of all-solid-state thin film lithium battery using LiPON electrolyte," *Materials Letters*, 134, (2014) pp. 237-239.

[17] Mo, S., Lu, P., Ding, F., Xu, Z., Liu, J., Liu, X., Xu, Q., "High-temperature performance of all-solid-state battery assembled with 95(0.7Li2S-0.3P2S5)-5Li3PO4 glass electrolyte," *Solid-state Ionics*, 296, (2016) pp. 37-41.

[18] Wan, J., Xie, J., Kong, X., Liu, Z., Liu, K., Shi, F., Pei, A., Chen, H., Chen, W., Chen, J., Zhang, X., "Ultrathin, Flexible, Solid Polymer Composite Electrolyte Enabled With Aligned Nanoporous Host For Lithium Batteries," *Nature Nanotechnology*, 14 (2019), pp.705-711.

[19] Ambrosi, R., Watkinson, E.J., Barco, A., Mesalam, R., Crawford, T., Bicknell, C., Williams, H., Perkinson, M.C., Burgess, C., Gibson, S. and Stroud, C., 2019, March. Radioisotope power systems for the European space nuclear power program. In 2019 IEEE Aerospace Conference (pp. 1-10). IEEE.

[20] Ambrosi, R., Williams, H. and Samara-Ratna, P., 2013. Americium-241 radioisotope thermoelectric generator development for space applications.

[21] Ambrosi, R.M., Williams, H.R., Samara-Ratna, P., Jorden, A., Slade, R., Bannister, N.P., Sykes, J., Deacon, T., Stephenson, K., Simpson, K. and Reece, M., 2013. Development and testing of an americium-241 radioisotope thermoelectric generator.

[22] Dyal, P., 1990, January. Pioneers 10 and 11 deep space missions. In COSPAR Colloquia Series (Vol. 1, pp. 373-382). Pergamon.

[23] Whiting, C.E. and Woerner, D.F., 2023. Lifetime Performance of Spaceborne RTGs. The Technology of Discovery: Radioisotope Thermoelectric Generators and Thermoelectric Technologies for Space Exploration, pp.183-212.
[24] Breseke, D. and Muscolino, C., 1968, October. Advanced ALSEP. In 5th Annual Meeting and Technical Display (p. 1025).
[25] www.planetary.org/articles/plutonium-power-for-space-missions
[26] Wham, R., Onuschak, B., Sutliff, T., "Plutonium-238 Supply project – Additional processing Enabling Power for Future NASA Missions," *Proceedings of 2016 IEEE Aerospace Conference*, Big Sky, Montana, 5-12 Mar 2016.
[27] Barklay, C.D., 2023. Advanced US RTG Technologies in Development. The Technology of Discovery: Radioisotope Thermoelectric Generators and Thermoelectric Technologies for Space Exploration, pp.245-275.
[28] ESA Radioisotope Study Final Review – SEA Ltd, 9 February 2021, www.unoosa.org/pdf/pres/stsc2012/tech-18E.pdf
[29] https://physics.nist.gov/PhysRefData/Star/Text/ASTAR.html
[30] https://physics.nist.gov/PhysRefData/Star/Text/ESTAR.html
[31] https://physics.nist.gov/PhysRefData/XrayMassCoef/tab3.html
[32] Khatry, J., Nieminen, J., Smith, J., Slotten, K., "10 We Radioisotope Thermophotovoltaic (RTPV) Power Source Demonstration," NETS-2017 Nuclear and Emerging Technologies for Space, February 2017, Orlando, FL.
[33] Agostinelli, S., Allison, J., Amako, K., Apostolakis, J., Araujo, H., et al., "Geant4: A simulation toolkit," *Nuc. Instr. Phys. Res A,* 506, (2003), pp. 250-303.
[34] Ivantchenko, A., Ivantchenko, N., Quesada, Molina, J., Incerti, S., "GEANT4 Hadronic Physics for Space Radiation Environment," *Int J Rad Biol* 88, (2012), pp. 171-175.
[35] O'Neill, P., Golge, S., Slaba, T., "Badhwar-O'Neill 2014 Galactic Cosmic Ray Flux Model Description," National Aeronautics and Space Administration Report No. NASA-TP-2015-218569, 2015.
[36] Shea, M., Smart, D., "A Summary of Major Solar Proton Events," *Solar Phys*. 127, (1990) pp. 297-320.
[37] Cucinotta F., Kim M., Chappell, L., "Space Radiation Cancer Risk Projections and Uncertainties – 2012," National Aeronautics and Space Administration Report No. NASA-TP-2013-217375, 2013.
[38] ICRP. 2007. The 2007 Recommendations of the International Commission on Radiological Protection. International Commission on Radiological Protection Report No. 103.
[39] Guttman, D., Woerner, D., "Environmental Requirements Document for Next Generation RTG (Next Gen. RTG)," National Aeronautics and Space Administration Report RPS-REQ-0147 Rev. A, 2020.
[40] https://www.osti.gov/servlets/purl/4633320
[41] Title 10, Part 20, of the Code of Federal Regulations (10 CFR Part 20), "Standards for Protection Against Radiation."
[42] https://www.cdc.gov/nceh/radiation/air_travel.html
[43] Tan, C., Leung, K.Y., Liu, D.X., Canova, M., Downing, R.G., Co, A.C. and Cao, L.R., 2015. Gamma radiation effects on Li-ion battery electrolyte in neutron depth profiling for lithium quantification. Journal of Radioanalytical and Nuclear Chemistry, 305, pp.675-680.
[44] Tan, C., Lyons, D.J., Pan, K., Leung, K.Y., Chuirazzi, W.C., Canova, M., Co, A.C. and Cao, L.R., 2016. Radiation effects on the electrode and electrolyte of a lithium-ion battery. Journal of Power Sources, 318, pp.242-250.
[45] Stoddard, D. H., Albenesis, E. L., "Radiation Properties of 238Pu Produced for Isotopic Power Generators," Office of Scientific and Technical Information, July 1965.
[46] Wasiolek, M., Romaine, D., "Unexpected Neutron Emissions from New Sealed Am-241 Sources," Sandia National Laboratories, SAND2018-2620C, https://www.osti.gov/servlets/purl/1502279.
[47] Hoefs, J., Sywall, M., "Lithium isotope composition of Quaternary and Tertiary biogene carbonates and a global lithium isotope balance," *Geochimica et Cosmochimica Acta*, 61 (1997), pp. 2679-2690.
[48] Sedlacek, W. A., Ryan, V. A., "Prompt Activation Analysis for Lithium-6," *Analytical Chemistry*, 40, (1968), pp. 678.
[49] Barker, F. C., "Neutron and Proton Capture by 6Li," *Austrian Journal of Physics*, 33, (1980) pp. 159.

[50] Dudney, N.J., 2000. Addition of a thin-film inorganic solid electrolyte (LiPON) as a protective film in lithium batteries with a liquid electrolyte. Journal of power sources, 89(2), pp.176-179.
[51] Kozen, A.C., Pearse, A.J., Lin, C.F., Noked, M. and Rubloff, G.W., 2015. Atomic layer deposition of the solid electrolyte LiPON. Chemistry of Materials, 27(15), pp.5324-5331.
[52] Sepúlveda, A., Criscuolo, F., Put, B. and Vereecken, P.M., 2019. Effect of high temperature LiPON electrolyte in all solid-state batteries. Solid-state Ionics, 337, pp.24-32.
[53] Jiménez, A.R., Nölle, R., Wagner, R., Hüsker, J., Kolek, M., Schmuch, R., Winter, M. and Placke, T., 2018. A step towards understanding the beneficial influence of a LIPON-based artificial SEI on silicon thin film anodes in lithium-ion batteries. Nanoscale, 10(4), pp.2128-2137.
[54] Kim, Y., Veith, G. M., Nanda, J., Unocic, R. R., Chi, M., Dudney, N. J., "High Voltage Stability of LiCoO2 Particles with a Nano-Scale LiPON Coating," *Electrochimica Acta*, 56, (2011), pp. 6573-6580.
[55] 17. Xu, F., Dudney, N. J., Veith, G. M., Kim, Y., Erdonmez, C., Lai, W., Chiang, Y.-M., "Properties of Lithium Phosphorus Oxynitride (LiPON) for 3D Solid-State Lithium Batteries," *Journal of Materials Research*, 25, (2010) pp. 1507-1515.
[56] McBrayer, J.D., Rodrigues, M.T.F., Schulze, M.C., Abraham, D.P., Apblett, C.A., Bloom, I., Carroll, G.M., Colclasure, A.M., Fang, C., Harrison, K.L. and Liu, G., 2021. Calendar aging of silicon-containing batteries. Nature Energy, 6(9), pp.866-872.
[57] Xu, F., Dudney, N.J., Veith, G.M., Kim, Y., Erdonmez, C., Lai, W. and Chiang, Y.M., 2010. Properties of lithium phosphorus oxynitride (LiPON) for 3D solid-state lithium batteries. Journal of Materials Research, 25(8), pp.1507-1515.
[58] Axmann, P., Gabrielli, G. and Wohlfahrt-Mehrens, M., 2016. Tailoring high-voltage and high-performance LiNi0. 5Mn1. 5O4 cathode material for high energy lithium-ion batteries. Journal of Power Sources, 301, pp.151-159.
[59] Julien, Christian & Mauger, Alain. (2013). Review of 5-V electrodes for Li-ion batteries: Status and trends. Ionics. 19. 10.1007/s11581-013-0913-2.
[60] J. Li, et al. Adv. Energy Mater. 5, 1401408 (2015)
[61] Cherkashinin, G., Yu, Z., Eilhardt, R., Alff, L. and Jaegermann, W., 2020. The effect of interfacial charge distribution on chemical compatibility and stability of the high voltage electrodes (LiCoPO4, LiNiPO4)/solid electrolyte (LiPON) interface. Advanced Materials Interfaces, 7(12), p.2000276.
[62] Yu, L., Tian, Y., Xiao, X., Hou, C., Xing, Y., Si, Y., Lu, H. and Zhao, Y., 2021. Investigation on the overlithiation mechanism of LiCoO2 cathode for lithium ion batteries. Journal of The Electrochemical Society, 168(5), p.050516.
[63] A. Deb, et al. J. Applied Physis, 99, 063701 (2006).
[64] Dustin, J. S., Borrelli, R. A., "Modeling of Am-241 as an alternative fuel source in a radioisotope thermoelectric generator," *Nuclear Engineering and Design*, 385, (2021), pp. 111495.
[65] Johnson, S. G., "Considerations for Use of Am-241 for Heat Source Material for Radioisotope Power Systems," Idaho National Laboratory, INL/EXT-16-40336-Revision-1.
[66] Caillat, T., "Thermoelectrics: from Space to Terrestrial Applications–Successes, Challenges and Prospects," *College de France, Paris,* March 2013.
[67] Caillat, T., "Thermoelectrics: from Space to Terrestrial Applications–Successes, Challenges and Prospects," *College de France, Paris,* March 2013.
[68] Kim, H. S., Liu, W., Chen, G., Chu, C.-W., Ren, Z., "Thermoelectric Conversion Efficiency," *Proceedings of the National Academy of Sciences*, 112 (2015), pp. 8205-8210.
[69] Wang, X. Y., Fabanich, W., Schmitz, P., "Advanced Stirling Radioisotope Generator Thermal Power Model in Thermal Desktop SINDA/FLUINT Analyzer," *10th International Energy Conversion Engineering Conference*, 4060, (2012).
[70] Holgate, T.C., Song, Y., Shi, D., Utz, R., Chung, T., Bennett, R., Keyser, S., Hammel, T.E., Sievers, R., Caillat, T. and Fleurial, J.P., 2016. Enhancement of the Multi-Mission Radioisotope Thermoelectric Generator with Efficient Skutterudite Thermoelectric Couples: Current Status of the Skutterudite Technology Maturation Program. In 14th International Energy Conversion Engineering Conference (p. 4817).
[71] Woerner, D., 2016. A Progress Report on the eMMRTG. Journal of Electronic Materials, 45, pp.1278-1283.
[72] Matthes, C. S. R., Woerner, D. F., Caillat, T., and Pinkowski, S., "A Status Update on the eMMRTG Project," 2019 IEEE Aerospace Conference, Big Sky, MT, USA, 2019, pp. 1-9, doi: 10.1109/AERO.2019.8741919.

[73] Cheng, Eric Jianfeng, et al. "Cast-in-place, ambiently-dried, silica-based, high-temperature insulation." Acta Materialia 127 (2017): 450-462.
[74] M Rull-Brave, A. M.-G. (2015). Skutterudites as thermoelectric materials: revisited. RSC Adv. , 41653-41667.
[75] Xiao, X., Yu, S., Huang, J., Zhang, H., Zhang, Y., Xiao, L., "Thermophysical properties of the regolith on the lunar far side revealed by the *in situ* temperature probing of the Chang'E-4 mission," *National Science Review*, Volume 9, Issue 11, November 2022, nwac175.
[76] A. Barco, R. M. Ambrosi, H. R. Williams, T. Crawford, R. Mesalam, C. Bicknell, E. J. Watkinson, K. Stephenson, A. Godfrey, C. Stroud, M.-C. Perkinson, C. Burgess, "Design and Development of the ESA Am-Fueled Radioisotope Power Systems," 2019 IEEE Aerospace Conference, Big Sky, MT, USA, 2019, pp. 1-11, doi: 10.1109/AERO.2019.8741786.
[77] R.M. Ambrosi, R. Mesalam, A. Barco, E.J. Watkinson, H. Sargeant, C. Bicknell, T. Crawford, R. Tute, G. Bustin, T. Tinsley, R. Sanderson, "The European Radioisotope Power Systems Program: Updates & Synergies," In Nuclear and Emerging Technologies for Space (NETS 2024). https://www.ans.org/pubs/proceedings/article-55887/
[78] L. A. Dudzinksi, "Radioisotope Power for NASA's Space Science Missions," Briegind to the Outer Planets Advisory Group, March 2008, https://www.lpi.usra.edu/opag/march_08_meeting/presentations/dudzinski.pdf
[79] https://investors.intuitivemachines.com/news-releases/news-release-details/nasa-selects-intuitive-machines-team-develop-survive-lunar-night
[80] C. S. R. Matthes, D. F. Woerner, T. Caillat, S. Pinkowski, "A Status Update on the eMMRTG Project," 2019 IEEE Aerospace Conference, 2019, pp. 1-9, (2019) doi: 10.1109/AERO.2019.8741919.
[81] https://esc.gsfc.nasa.gov/projects/LCRNS
[82] www3.nasa.gov/sites/default/files/atoms/files/lunanet_interoperability_specification_version_4.pdf
[83] Helvajian, H., Rosenthal, A., Pokelmba, J., Battista, T., "A Mision Architecture to Reach and Operate at the Focal Region of the Solar Gravitational Lens," https://doi.org/10.48550/arXiv.2207.03005
[84] Appelbaum, J., Landis, G. A., "Photovoltaic arrays for Martian surface power," *Acta Astronautica*, 30, (1993) pp. 127-142.
[85] https://solaerotech.com/solaero-makes-history-with-solar-panel-that-powered-first-successful-flight-on-mars/
[86] https://www.linkedin.com/pulse/mars-helicopter-ingenuity-deep-dive-its-6-pack-damien-frost/
[87] Withrow-Maser, S., Johnson, W., Young, L., Cummings, H., Chan, A., Tzanetos, T., Balaram, J., Bapst, J., "An Advanced Mars Helicopter," AIAA Ascend 2020.
[88] Yang, J., Caillat, T., "Thermoelectric Materials for Space and Automotive Power Generation," *MRS Bulletin*, 31, (2006), pp. 224–229.
[89] Emanuelli, E., "NASA Will Pay the Entire Cost of Pu-238 Production," *Space Safety Magazine*, April 24, 2013.
[90] "ORNL-Produced Plutonium-238 to Help Power Perseverance on Mars." ORNL.gov, July 29, 2020.
[91] "NASA's Management of Its Radioisotope Power Systems Program," Office of the Inspector General, IG-23-010 (Assignment No. A-22-02-00-SAR), March 20, 2023.
[92] https://spacenews.com/dod-looking-for-commercially-available-nuclear-propulsion-for-small-spacecraft/
[93] E.W. Johnson, Monsanto Research Corporation, Mound Laboratory Report, MLM-3250(OP) (1984). https://www.osti.gov/servlets/purl/5688898
[94] Robertson, G.A, Young, D., Love, L., Cunningham, K., Kim, T., Ambrosi, R., M., Williams, H., "Preliminary Analysis: Am-241 RHU/TEG Electric Power Source for Nanosatellites," *Nuclear and Emerging Technologies for Space 2014*, Stennis, MS, February 24-26, 2014.
[95] Ulamec, Stephan, Jens Biele, and Ed Trollope. "How to survive a Lunar night." Planetary and space science 58, no. 14-15 (2010): 1985-1995.
[96] Bux, S., Fleurial, J.-P., Caillat, T., "Engineering of Novel Thermoelectric Materials and Devices for Next Generation, Long Life, 20% Efficient Space Power Systems," 11th International Energy Conversion Engineering Conference, 3927 (2013).
[97] Matthes, C. S. R., Woerner, D. F., Caillat, T. and Pinkowski, S., "A Status Update on the eMMRTG Project," 2019 IEEE Aerospace Conference, 2019, pp. 1-9, doi: 10.1109/AERO.2019.8741919.

[98] Caillat, T., Pinkowski, S., Chi, I., Smith, K., Paik, J., Bennett, R., Keyser, S., Lane, A., Wefers, K. "Development, Testing and Power Performance Prediction Update for the Skutterudite-Based MMRTG," 327-330. (2023).10.13182/NETS23-41921.
[99] Lane, A., Otting, W., Wefers, K., Frye, P., VanderVeer, J., Bennett, R., Keyser, S., Pinkowski, S., Caillat, T., "Path to Skutterudite Based Multi-Mission Radioisotope Thermoelectric Generator Flight Qualification Unit," 466-466. (2022). 10.13182/NETS22-38757.
[100] Gard, L. and Lane, A., 2024, March. Status of Current Aerojet Rocketdyne RPS Programs. In 2024 IEEE Aerospace Conference (pp. 1-11). IEEE.
[101] Helvajian, H., Rosenthal, A., Poklemba, J., Battista, T.A., DiPrinzio, M.D., Neff, J.M., McVey, J.P., Toth, V.T. and Turyshev, S.G., 2023. Mission Architecture to Reach and Operate at the Focal Region of the Solar Gravitational Lens. Journal of Spacecraft and Rockets, 60(3), pp.829-847.
[102] https://www.nasa.gov/general/scope-sciencecraft-for-outer-planet-exploration/
[103] Weber, R.C., Neal, C., Banerdt, B., Beghein, C., Chi, P., Currie, D., Dell'Agnello, S., Garcia, R., Garrick-Bethell, I., Grimm, R. and Grott, M., 2020. The lunar geophysical network mission. In Seg technical program expanded abstracts 2020 (pp. 3530-3533). Society of Exploration Geophysicists.